# Broadband Dielectric Response in Hard and Soft PZT: Understanding Softening and Hardening Mechanisms

THÈSE Nᴼ 4988 (2011)

PAR

## Li JIN

EPFL

ÉCOLE POLYTECHNIQUE
FÉDÉRALE DE LAUSANNE

Suisse
2011

# Abstract

Lead zirconate titanate ($Pb(Zr_{1-x}Ti_x)O_3$ or PZT) ferroelectric ceramics have been widely used in transducers, actuators, and sensors, since they posses high dielectric and piezoelectric properties with a relatively high temperature of operation. Commercially used PZT ceramics are always modified by different dopants and are divided into the "soft" (donor doped) and "hard" (acceptor doped) groups. Compared with the undoped composition, hard PZT often shows lower but more stable properties after ageing. In contrast, soft PZT shows higher properties and insensitivity to ageing. The difference in properties between the soft and hard PZT ceramics is rather large, even though the doping level is limited to a very low value (on the order of 1 mole %). The large difference of the physical properties between them mainly originates from the contributions from domain wall motion rather than properties of the crystal lattice. However, the mechanisms of hardening and softening are not well understood.

In order to understand better the hardening and softening mechanisms, in this thesis the different contributions to the dielectric properties of soft and hard PZT ceramics are studied by means of a broadband dielectric spectroscopy from 10 mHz to 20 GHz. Properties at THz and infrared frequencies where only crystalline lattice contributes to the dielectric response were also investigated in collaboration with another group. In the frequency range below 20 GHz, the different contributions to the permittivity by domain wall motion were revealed in hard and soft materials. In order to correlate the properties to the microscopic structure of hard and soft PZT ceramics, the domain structures were also investigated by transmission electron microscopy. Piezoelectric spectroscopy was employed to help separating different contributions at frequencies below 100 Hz. The main results of this work are:

The microwave dielectric dispersion of all PZT ceramics (including undoped, soft and hard PZT ceramics), which is characterized by a rapid decrease of the permittivity and a loss peak in the GHz frequency range, is contributed by both domain wall motion and piezoelectric grain resonances. These two mechanisms are separated by gradual poling of samples. The dispersion related to the domain wall motion appears at a higher frequency than the one related to grain resonance and constitutes the main contribution to the microwave dielectric properties of unpoled samples. Above the GHz frequency range, the dielectric properties of hard and soft PZT ceramics are rather close and approach the upper limit value of their intrinsic properties, which are identified by dielectric properties determined by THz dielectric spectrum. The contributions by domain wall motion make up more than 50% of the quasistatic dielectric properties (measured at 100 kHz) in all studied samples.

Below GHz frequency range, another dielectric dispersion due to the domain wall creep, which manifests itself by a logarithmic decrease of permittivity with increasing frequency, is indentified in both soft and hard PZT ceramics in a relatively broad frequency region over at least eight decades. The difference of the dielectric properties between the hard and soft PZT mainly results from this logarithmic dispersion, since soft PZTs exhibit stronger logarithmic dispersion than hard PZTs. By controlling the doping kind and crystalline symmetry, the slope of the logarithmic function can be adjusted. Large values are observed in the system with disordered distribution of defect dipoles (soft, donor doped materials) while nearly zero slope could be observed in hard, acceptor doped materials with tetragonal structure with defect dipoles well aligned with polarization within domains.

Rapid increase of both permittivity and loss below 1 Hz, which cannot be described by the logarithmic function, is observed in hard PZT ceramics. To interpret this behavior, results of dielectric spectroscopy were complemented by piezoelectric measurements in the frequency range from 10 mHz to 100 Hz. The absence of the strong dispersion in the piezoelectric properties and presence in the dielectric response strongly indicates that its origin is in charge transport (such as hopping conductivity) rather than in motion of domain walls.

Nanodomains, observed in $Fe^{3+}$-doped hard PZT with composition at morphotropic phase boundary do not lead to the high dielectric and piezoelectric properties, as would be expected from some theoretical models. Acceptor doping rapidly decreases the domain size in PZT ceramics with compositions in rhombohedral, tetragonal and MPB regions. This effect could not be interpreted by the decrease of the grain size according to the commonly assumed parabolic relationship between the domain size and grain size. The small domain size is rather related to the presence of oxygen vacancies which break continuity of polarization.

**Key words:** PZT ceramics, dielectric spectroscopy, domain wall, permittivity, dielectric losses, defect dipoles, microwave, TEM.

# Résumé

Les matériaux céramiques ferroélectriques basés sur le titanate de plomb et zirconium ($Pb(Zr_{1-x}Ti_x)O_3$ ou PZT) ont étés largement employés comme transducteurs, actuateurs et senseurs, en raison de leurs bonnes propriétés diélectriques et piézoélectriques et des températures opérationnelles relativement élevées. Les céramiques de PZT utilisés commercialement sont toujours modifiés avec des dopants et sont regroupées entre les groups "doux ou soft" (dopés avec des donneurs) et "dur ou hard" (dopés avec des accepteurs). Comparés avec les matériaux non dopés le "hard" PZT montre souvent propriétés moins élevées mais plus stables après vieillissement. Par contre le "soft" PZT montre propriétés plus élevées et insensibilité au vieillissement. La différence de propriétés entre le "soft" et le "hard" PZT est plutôt importante même si la quantité de dopants est limité a valeurs très faibles (dans l'ordre de 1 mole%). La grand différence de propriétés physiques entre eux trouve son origine principalement dans la contribution au mouvement de parois de domaine plutôt que dans des différences du réseau cristallin. Pourtant les mécanismes de l'adoucissement et du durcissement ne sont pas très bien connu.

Dans le but de mieux comprendre les mécanismes de l'adoucissement et du durcissement dans cette thèse, les différentes contributions aux propriétés diélectriques des céramiques de PZT "soft" et "hard" ont été étudiées avec la spectroscopie diélectrique en bande large de 10 mHz à 20 GHz. Les propriétés dans les THz et les infrarouges ou seulement le réseau cristalline contribue à la réponse diélectrique ont aussi été investiguées en collaboration avec un autre group. Dans l'intervalle de fréquences au-dessous de 20 GHz les différents contributions à la permittivité dues aux parois de domaine ont été révélées dans les matériaux "hard" et "soft". Pour trouver une relation des propriétés à la structure microscopique de céramiques de PZT "hard" et "soft", les structures de domaines ont été investiguées avec le microscope électronique à transmission. La spectroscopie piézoélectrique a été utilisée pour séparer les différentes contributions à des fréquences au-dessous de 100 Hz. Les résultats principaux de ce travail sont:

La dispersion diélectrique de microondes de tous les céramiques de PZT (compris les non dopés, les céramiques de PZT "soft" et "hard") qui est caractérisée par une rapide diminution de la permittivité et par un pic de perte dans la gamme de fréquence de GHz, a des contributions soit de mouvement de parois de domaine soit de résonance piézoélectrique des grains. Les deux mécanismes sont sépares par graduelle polarisation des échantillons. La dispersion liée aux mouvements des parois de domaines apparait à plus hautes fréquences par rapport a celles

liées à la résonance des grains et représente la majeure contribution aux propriétés diélectrique des échantillons non-polarisés. Au dessus de l'intervalle de fréquence de GHz, les propriétés diélectriques des céramiques de "hard" et "soft" PZT sont plutôt proches et rejoignent la valeur limite des propriétés intrinsèques identifiées par des propriétés diélectriques déterminées par le spectroscopie diélectrique de THz. Les contribuions des parois de domaines forment plus du 50% de la valuer de la permittivite diélectrique quasi-statique (mesurée a 100 kHz) dans tous les échantillons étudiés.

Au dessus de l'intervalle de fréquences des GHz, une autre dispersion diélectrique due au fluage des parois de domains se manifestant à travers une diminution logarithmique de la permittivité avec l'augmentation de la fréquence. Elle est identifiée dans les céramiques de PZT "soft" et "hard" dans une région de fréquences relativement large, sur une échelle d'au moins huit ordres de grandeur. La différance de propriétés diélectriques entre le "hard" et le "soft" PZT réside principalement dans cette dispersion logarithmique, vue que le "soft" PZT montre une dispersion logarithmique plus élevée que le "hard" PZT. Avec un contrôle du type de dopage et de la symétrie du crystal, la pente de la fonctionne logarithmique peut être ajusté. Valeurs élevées ont été observées dans les systèmes avec une distribution désordonnée de défauts de dipôle (matériaux "soft" dopés avec donneurs) mais par contre une pente presque proche à zéro a été observée dans les matériaux hard dopes avec des accepteurs, ayant une structure tétragonale avec des défauts de dipôle bien alignées avec la polarisation dans les domaines.

Une augmentation rapide de la permittivité et de la perte au dessous de 1 Hz que ne peu pas être décrite par la fonctionne logarithmique a été observée dans les céramiques de "hard" PZT. Pour interpréter tel comportement les résultats de la spectroscopie diélectrique ont été complétés avec des mesures piézoélectriques dans l'intervalle de fréquences de 10 mHz à 100 Hz. L'absence d'une dispersion élevée dans les propriétés piézoélectriques et la présence dans la réponse diélectrique indique fortement que son origine est le transport de charge (comme par exemple la conduction par saut) plutôt que le mouvement des parois de domaines.

Les nano-domaines observés dans le "hard" PZT dopé avec $Fe^{3+}$ avec une composition correspondant à la frontière de phase morphotropique (morphotropic phase boundary ou MPB) n'ont pas conduit à des propriétés diélectriques et piézoélectriques élevées, comme on attendrait d'après quelque modèle théorique. Le dopage avec des accepteurs diminue rapidement la taille des domaines dans les céramiques de PZT avec des compositions dans les régions rhomboédrique, tétragonale et de la MPB. Un tel effet ne peut pas être interprété par une réduction de la taille de grains en accord avec la relation parabolique entre la taille des domaines et la taille de grains qui est communément acceptée. La petite taille des domaines est plutôt corrélée à la présence de lacunes d'oxygène interrompant la continuité de la polarisation.

**Mots-clés:** PZT céramiques, la spectroscopie diélectrique, parois de domaine, la permittivité, les pertes diélectrique, des défauts de dipôle, microondes, TEM.

# Acknowledgments

First and foremost, I am indebted to my thesis supervisor, Prof. DRAGAN DAMJANOVIC, who gave me a precious opportunity to the beautiful city - Laussane - to join his research group. He introduced me into the wonderful and full of challenge materials world. Your *interest*, *hard working* and *patience* to the scientific researches impress me so much. It is my honor to work with you.

I am grateful to Prof. NAVA SETTER, who offered me the opportunity of working with the top scientists of our field, in the best laboratory conditions. In addition, I am thankful for the nice everyday conversations

Great thanks to Dr. VIKTOR POROKHONSKYY, who taught me the microwave characterization techniques. I also appreciate your suggestions on scientific writing and your constant encouragement to my work. You show me the power of LaTeX.

I am very grateful to Dr. ZHANBING HE for the collaboration on transmission electron microscopy. It is you let me enjoy the happiness of badminton and hiking.

I would like to thank Dr. GUOCHU DENG, Dr. TADEJ ROJAC and Dr. YONGLI WANG for your inspiring suggestions on the sintering and milling processing.

I gratefully acknowledge the research group at the Electroceramics Department of the *Josef Stefan Institute* for their warm hospitality in Ljubljana where I had the opportunity to study the processing of ceramics. I especially wish to thank Mrs. JENA CILENSEK, Prof. BARBARA MALIC and Prof. MARIA KOSEC who kindly organized my stay in Slovenia and provided me with useful experience in making good materials.

I am thankful to Prof. JAN PETZELT and his group at *Institute of Physics*, *Academy of Sciences of the Czech Republic* for cooperation on the THz dielectric spectrum.

I would further like to thank my thesis jury for your critical reading of my report. Special acknowledgments are give Prof. JAN PETZELT at *Institute of Physics* and Prof. PATRYCJA PARUCH at *University of Geneva* for their valuable comments on my thesis.

I am deeply indebted to Prof. XI YAO, Prof. XIAOYONG WEI and Prof. HONG WANG at *Xi'an Jiaotong University*. Your kindness and professionalism always support me in times when my mood was far below the standard. I feel that I am always your student and a member of *Electronic Materials Research Laboratory* (EMRL).

Special acknowledgments is given to Dr. YU BAI for his long support and encouragement.

You are always my important audience, especially when I was felt disappointed with something. The walking accompanied with the setting sun in the playground at *Ecublens* is a forever memory to my life.

I would also like to thank Lino Olivetta and Jacques Castano, who helped me resolve certain technical problems with experiments. Special thanks is given to Alberto Biancoli, who has transfered my English abstract into French at an unbelievable speed. Many thanks to Dr. Tomas Sluka, Maxim Gureev and Mahamudu Mtebwa. It is my pleasure to share the office with you.

I would like to express my thanks to the help and collaborations with all present and former Laboratory Ceramics friends: Yan Yan, Dr. Silviu Cosmin Sandu, Dr. Jin Wang, Dr. Igor Stolichnov, Dr. Tomas Sluka, Dr. Naama Klein, Dr. Enrico Colla, Dr. Evelyn Hollenstein, Dr. Scott Harada, Dr. Marko Budimir, Dr. Matthew Davis, Dr. Lisa Malin. They all contributed to fruitful collaborations and to the enjoyable and international atmosphere in the LC.

I acknowledge all my Chinese friends in EPFL for their patience and friendly encouragement, for not letting me feel lonely in a foreign country.

<div align="center">

慈母手中线，游子身上衣。

临行密密缝，意恐迟迟归。

谁言寸草心，报得三春晖。

</div>

The support and love of my family have been the endless fuel for all my life. Great thanks to my parents and grandma. You wrote this.

This document was produced using TEXshop2.18 typesetting system.

# Contents

# Chapter 1

# Introduction and goals

Lead zirconate titanate ($Pb(Zr_{1-x}Ti_x)O_3$ or PZT) ferroelectric ceramics are widely used in applications such as transducers, actuators, sensors and etc. This is because the PZT compositions 1) possess high piezoelectric and electromechanical coupling coefficients, 2) exhibit high Curie point, $T_C$, which permit a high temperature of operation (above $200\,^{\circ}C$), 3) can be easily poled, 4) possess a wide range of dielectric constants, (5) are relatively easy to sinter at lower temperatures, (6) form solid solution compositions with many different constituents, thus allowing a wide range of achievable properties [1].

PZT ceramics are especially attractive for designing materials properties, since a wide range of physical properties could be tailored by adjusting the Zr/Ti ratio, particularly in the so-called *morphotropic phase boundary* (MPB) region. Depending on requirement of the applications, commercially used PZT ceramics are always modified by different dopants. Those doped PZT ceramics are mainly divided into the "soft" and "hard" PZTs, which are normally prepared by substituting the A-site or B-site ions with donor and acceptor dopants, respectively [2]. Compared with the undoped composition, hard PZT shows lower permittivity, piezoelectric coefficients and elastic compliances, low dielectric and mechanical losses, lowered resistivity, pronounced ageing, and pinched ferroelectric hysteresis in aged state. In contrast, soft PZT shows higher properties, larger losses, improved resistivity, low ageing, square polarization loops, easy poling and depoling [3; 4].

Even though the doping level is limited at a very low value (less than 5 mole %), the difference of those physical properties between the soft and hard PZT ceramics is still impressively large. It is believed that the large difference of the physical properties mainly comes from the extrinsic (domain wall contributions), instead of the intrinsic (crystal lattice). The aim of this thesis is to clarify the mechanisms which govern the soft and hard behaviors in PZT ceramics. The understanding of these mechanisms would benefit the designing the physical properties not only for the PZT system, but also for the novel ferroelectric materials [5; 6; 7].

In this chapter, we will first explain the frequently used concepts, terms and symbols. Then the progress on the studies of PZT ceramics, especially on the related topics of the softening and hardening mechanisms, will be briefly reviewed. Finally the goals of the thesis will be stated.

## 1.1   Background

### 1.1.1   Ferroelectricity and domains

Ferroelectric materials possess a spontaneous electric polarization that can be reversed by the application of an external electric field (8). The term is used in analogy to ferromagnetism, in which a material exhibits a permanent magnetic moment (9). According to the crystalline symmetry with respect to a point, there are 21 non- centrosymmetric classes. However, only 10 classes among these 21 classes have a unique polar axis. Crystals belonging to these classes are called *polar* since they possess a *spontaneous polarization*, $P_s$ (10). In general, $P_s$ decreases with increasing temperature to disappear either continuously or discontinuously at a *Curie point*, $T_C$.[1] Usually the phase above $T_C$ is termed as *paraelectric* phase.[2]

In ferroelectrics below $T_C$ and in the absence of external electric field, a $P_s$ develops along at least two directions. In order to minimize the energy of depolarizing fields, crystal splits into polar regions along each of these directions. Each volume of uniform polarization is called a *domain*. Crystallographically, domain structure is a type of twinning (12). The resulting domain structures usually results in a nearly complete compensation of macroscopic polarization. The polarization directions of domains are basically high temperature symmetry axes, such as $\langle 001 \rangle$, $\langle 110 \rangle$ or $\langle 111 \rangle$. Angles between the dipoles of adjacent domains are those between such symmetry axes, e.g. $90°$, $180°$, and $71°$, respectively. The boundaries separating domains are referred to as *domain walls*. In ferroelectrics, the domain walls could be shifted or switched by an external electric field. The polarization- electric field relationship in ferroelectrics is often nonlinear and hysteretic, due to the domain wall motion and switching.

The ferroelectricity was discovered in single crystal Rochelle salt by Valasek in 1921 (13). The demonstration of the ferroelectricity in polycrystalline $BaTiO_3$ ceramics proved to be much valuable when it was discovered by Gray (1). The prevailing opinion in that period was that ceramics could not be piezoelectrically active, because randomly oriented grains would, on the whole, cancel out each other (1). This proved not to be the case for polycrystalline ferroelectric ceramics, since the domains within the grains could be permanently aligned or reoriented by means of an electric field, somewhat analogous to magnetic alignment in permanent magnets. This electrical aligning or "poling" process, was correctly identified as the key to turning an inert ceramic into an electromechanically active material with a multitude of industrial and commercial uses.

Unfortunately, in spite of almost 50 years of continuous effort there are still no reputable $Pb(Zr_{1-x}Ti_x)O_3$ single crystals available with compositions near the MPB. Only compositions close to pure $PbTiO_3$ and $PbZrO_3$ have been grown with adequate quality. Therefore most of studies of domain walls in PZT are performed in ceramic materials.

---

[1]Not all polar materials exhibit a Curie point.

[2]One exception is Rochelle salt ($KNaC_4H_4O_6 \cdot 4H_2O$), which processes two $T_C$ at -18 °C and 23 °C (11). The ferroelectric state exists in the range between those two Curie points. Of course, this material is also paraelectric below -18 °C.

## 1.1.2 Dielectric and piezoelectric properties

According to the crystallographical classification, ferroelectrics are the subgroup of polar dielectrics and piezoelectrics. Naturally, a ferroelectric inherently possess dielectric and piezoelectric properties. In this section, the frequently used dielectric and piezoelectric terms will be introduced.

In a dielectric crystal, the polarization $P_i$ is proportional to the applied electric field $E_j$, with the second rank tensor named dielectric susceptibility, $\chi_{ij}$:

$$P_i = \chi_{ij}E_j. \tag{1.1}$$

The dielectric displacement $D_i$ is then defined as:

$$D_i = \varepsilon_0 E_i + P_i = (\varepsilon_0 \delta_{ij} + \chi_{ij})E_j = \varepsilon_0 \varepsilon_{ij}E_j, \tag{1.2}$$

where $\varepsilon_0$ is the vacuum dielectric permittivity with a value of $8.854 \times 10^{12}$ F/m, and $\delta_{ij}$ is Kronecker's symbol with $\delta_{ij} = 1$ for $i = j$ and otherwise $\delta_{ij} = 0$. Here, $\varepsilon_{ij}$ is the relative dielectric permittivity.

For an unpoled polycrystalline ferroelectric ceramic, second order tensor $\varepsilon_{ij}$ is reduced into a scalar quantity $\varepsilon$ because of its isotropic dielectric properties. Applying an alternating electric field to a real dielectric ceramic, the charge stored on the dielectric ceramic has both real (in phase) and imaginary (out of phase) components, caused by either resistive leakage or dielectric absorption. Therefore a complex permittivity ($\varepsilon^* = \varepsilon' - j\varepsilon''$) is needed to express both the real and imaginary parts. The real part normally is referred to as *dielectric constant*, while the loss tangent $\tan\delta$ is equal to $\varepsilon''/\varepsilon'$.

The piezoelectric effect is a linear interaction between the mechanical and the electrical state in crystalline materials with no inversion symmetry ([2]). The piezoelectric effect is reversible in that materials exhibiting the direct piezoelectric effect (the internal generation of electrical charge resulting from an applied mechanical force) also exhibit the converse piezoelectric effect (the internal generation of a mechanical strain resulting from an applied electrical field). In terms of dielectric displacement $D_i$ and stress $T_{jk}$, the direct piezoelectric effect is expressed as:

$$D_i = d_{ijk}T_{jk}. \tag{1.3}$$

The converse piezoelectric effect could be described by Eq. 1.4 through the strain $S_{ij}$ and electric field $E_k$,

$$S_{ij} = d_{kij}E_k. \tag{1.4}$$

For two effects, the proportionality constant $d_{kij}$ is the *piezoelectric constant*.

Naturally-occurring piezoelectric crystals are few and their piezoelectric properties are also weak, e.g., quartz ($SiO_2$). It was Jaffe, who realized the importance of "poling" process ([2]). By temporary application of a strong electric field to polycrystalline ferroelectric ceramics, polarization needed to impact the piezoelectric properties can be induced. It is obvious that the dielectric properties of a ferroelectric ceramic are not isotropic anymore after poling. A

single subscript 3 or 1 indicates the direction of measurement, being respectively parallel or perpendicular to the polar axis. The dielectric constants measured at constant (zero) stress and at constant (zero) strain are called "free" ($\varepsilon^T$) and "clamped" ($\varepsilon^S$) dielectric constants, respectively. They are related through the electromechanical coupling factor $k$ (2):

$$\varepsilon^S = \varepsilon^T (1 - k^2). \tag{1.5}$$

According to Eq. (1.5), it can be seen that a piezoelectric material with a large value of $k$ could result in a large difference between $\varepsilon^S$ and $\varepsilon^T$. $k$ depends on piezoelectric, elastic and electric constants and is zero in non-piezoelectrics.
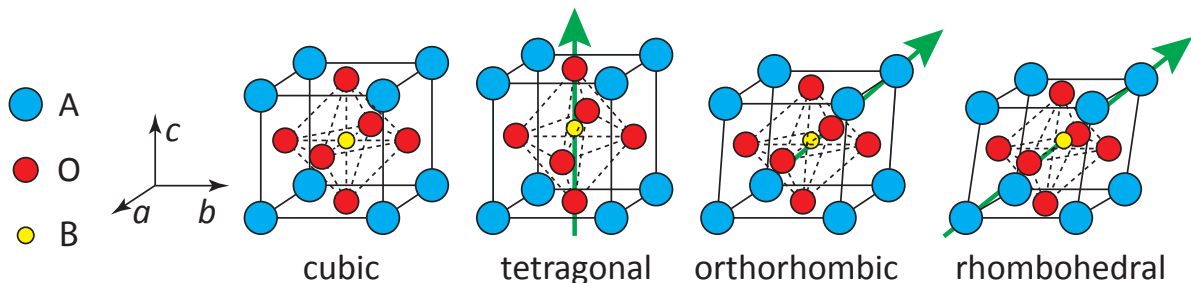
Combing with the elastic coefficients $s_{ijkl}$ and the electric permittivity $\varepsilon_{ij}$, the piezoelectric constitutive equations are expressed as:

$$D_i = d^E_{ijk} T_{jk} + \varepsilon^T_{ij} E_j, \tag{1.6}$$

and

$$S_{ij} = s^E_{ijkl} T_{kl} + d^T_{kij} E_k. \tag{1.7}$$

### 1.1.3 The perovskite structure and phase transitions



**Figure 1.1:** Perovskite structure of $ABO_3$. Unit cell in the cubic phase (a), tetragonal phase (b), orthorhombic phase (c) and rhombohedral phase (d).

The prototype of the *perovskite structure* comes from the mineral calcium titanate, $CaTiO_3$. Most of important piezoelectric ceramics, such as barium titanate ($BaTiO_3$) and PZT have such a perovskite structure (14; 15). These materials have a general chemical formula $ABO_3$, where O is oxygen, A represents a cation with a larger ionic radius, and B a cation with a smaller ionic radius (see Fig 1.1) (16). The mineral perovskite itself is not simple cubic. In most cases, however, the perovskite strictures is idealized as a cubic unit cell with a large cation on the corners, a smaller cation in the body center, and oxygens in the centers of the faces, as shown in Fig. 1.1(a). This structure forms a network of corner-linked oxygen octahedra, with the smaller cation filling the octahedral holes and the large cation filling the dodecahedral holes (2). Through this model, the paraelectric-ferroelectric (P-F) and ferroelectric-ferroelectric (F-F) phase transitions could be described as the distortion of the unit cell. All cations and anions may move with respect to the equilibrium position in the cubic perovskite unit cell.

By decreasing the temperature, the cubic paraelectric phase could transfer into other phases. Tetragonal, orthorhombic, and rhombohedral phases are the three symmetries which frequently occur. In tetragonal phase, the cubic unit cell of the perovskite structure elongates along the $c$ axis, i.e. the [001] direction, and results in the $a = b < c$ (Fig. 1.1(b)). In orthorhombic phase the unit cell elongates along a face diagonal (the [110] direction). As shown in Fig. 1.1(c), $a = c > b$ and $\beta$, which is the angle between the $a$ axis and $c$ axis, is $< 90°$. In rhombohedral phase (Fig. 1.1(d)), the unit cell distorts along the [111] direction with $a = b = c$ and $\beta < 90°$. In each phase, the dipole is generated by the displacement of the B-site ion along the same direction of the distortion and the $P_s$ in those phases is parallel to the [001], [110], and [111] direction, respectively (2)[3].

Most ferroelectric materials exhibit a paraelectric-ferroelectric phase transition at $T_C$. But it is not necessary for all the ferroelectric materials to experience one or several ferroelectric-ferroelectric phase transitions below the $T_C$. For example, $PbTiO_3$ keeps its tetragonal symmetry below its $T_C$ (490 °C), whereas $BaTiO_3$ transfers from the cubic paraelectric phase, through tetragonal ferroelectric phase and orthorhombic ferroelectric phase, into the rhombohedral ferroelectric phase on cooling from the $T_C$ at 120 °C (2).

## 1.2 Lead zirconate titanate
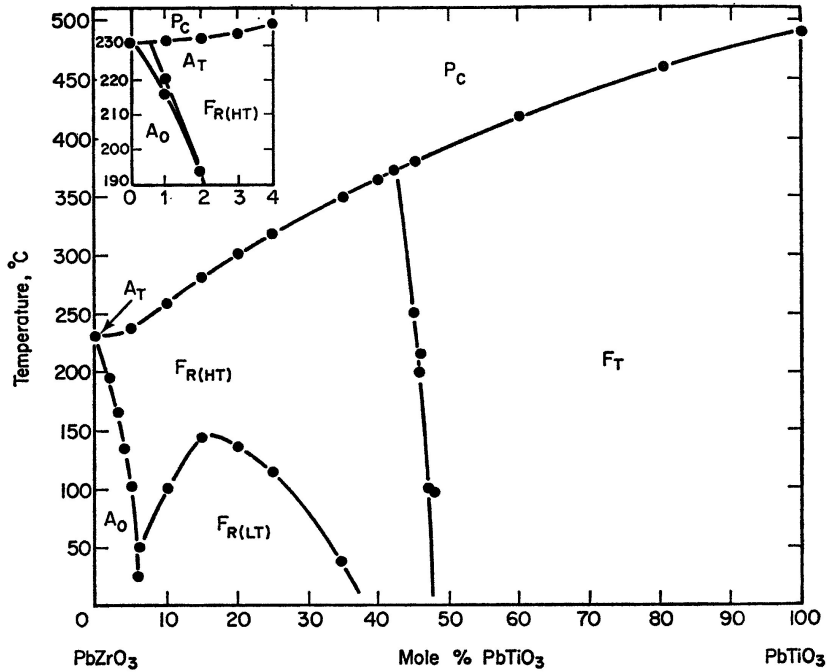
### 1.2.1 Phase diagram

Fig. 1.2 shows the phase diagram of PZT in the temperature range between 0 °C and 500 °C. This phase diagram is mainly based on the works conducted by Shirane (18; 19; 20), Jaffe (21), Barnett (22) and Berlincourt (23), and finally summarized by Jaffe, Cook an Jaffe in their treatise on piezoelectric ceramics (2). Except the region near the MPB, this phase diagram is widely accepted so far.

The end-members of this binary solid solution are $PbTiO_3$ and $PbZrO_3$. At room temperature, they are in the tetragonal ferroelectric phase and orthorhombic antiferroelectric phase, respectively. Replacing the $Ti^{4+}$ ion partially with $Zr^{4+}$ ion, the $c/a$ is decreased accompanied by the decrease of $T_C$. When $x$ is in the range between 0.48 and 1.0, the symmetry of $Pb(Zr_{1-x}Ti_x)O_3$ is tetragonal. Higher-level replacement of $Ti^{4+}$ with $Zr^{4+}$ ion results in a rhombohedral phase ($F_R$). Actually this rhombohedral phase is divided into two phases, i.e. high temperature $F_{R(HT)}$ and low temperature $F_{R(LT)}$ phase. Both of them exhibit the rhombohedral symmetry. The antiferrodistortive (or tilt) transition from the $F_{R(LT)}$ to the $F_{R(HT)}$ is accompanied with the loss of oxygen octahedron tilt angle and corresponding superstructure[4]. Further increase of the concentration of $Zr^{4+}$ ion generates an antiferroelectric orthorhombic phase,

---

[3]In some systems, the dipole is partially generated by the displacement of the A-site ion. In $PbTiO_3$, the dipole is mainly attributed to the displacement of Pb ion against the $BO_6$ octahedra (17).

[4]For this phase transition, neither the direction of $P_s$ nor the point symmetry changes, however, the magnitude of $P_s$ changes during the transition (24).

**Figure 1.2:** Phase diagram of PbZr$_{1-x}$Ti$_x$O$_3$ (PZT) solid solution. P$_C$, cubic paraelectric phase; F$_T$, tetragonal ferroelectric phase; F$_{R(HT)}$, high temperature rhombohedral ferroelectric phase; F$_{R(LT)}$, low temperature ferroelectric rhombohedral phase; A$_O$, orthorhombic antiferroelectric phase; A$_T$, tetragonal antiferroelectric phase. Taken from Jaffe, Cook, and Jaffe (2).

A$_O$ ($x <$ 0.05). Increasing the temperature close to the $T_C$, another antiferroelectric tetragonal phase (A$_T$) is observed in a very limited composition range.
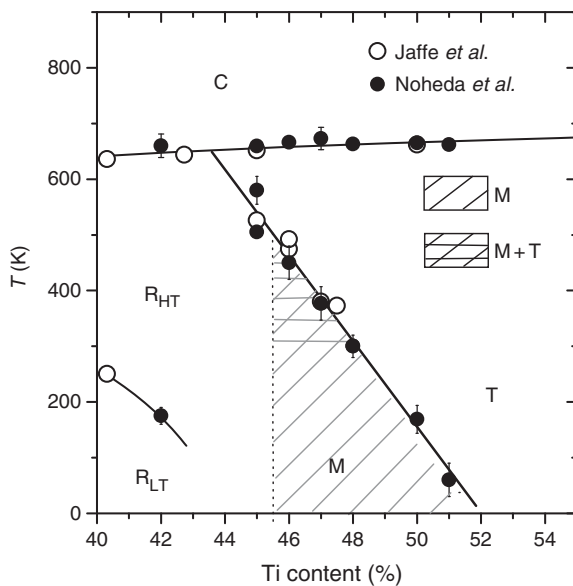
Note that in Fig. 1.2 the phase boundary between the tetragonal and rhombohedral phases is nearly independent of temperature (morphotropic phase boundary). The term *morphotropic* is used to denote an abrupt structure change with a solid solution with variation in composition (21). In contrast, the phase boundary between the F$_{R(HT)}$ (or F$_{R(LT)}$) and A$_O$ is more curved.

## 1.2.2   Morphotropic phase boundary

Elucidation of the phase diagram of PZT near MPB is beyond the scope of this thesis. Here we only present a brief introduction of the progress of the study of MPB, since compositions involved in this region will be studied in the following chapters. The discussion below is mainly based on the reviews given by Noheda (25; 26).

Over the many years, it came to be generally accepted that the so-called MPB is a region of coexistence between the F$_T$ and F$_R$, with a variable width dependent on the homogeneity of the powders (27; 28; 29) and the grain size (30). A comprehensive review of the early research of the MBP is given by Glazer *et al* (31).

In 1999, Noheda *et al* observed an unsuspected monoclinic (*M*) phase in Pb(Zr$_{0.52}$Ti$_{0.48}$)O$_3$ by high-resolution synchrotron x-ray powder diffraction techniques (33). The symmetry of the monoclinic phase was found to be a space group *Cm*, which has just a mirror plane and no

**Figure 1.3:** Phase diagram of PbZr$_{1-x}$Ti$_x$O$_3$ (PZT) solid solution near MPB based on synchrotron x-ray powder diffraction data. Taken from Noheda *et al* (32).

symmetry axis. This mirror plane is also the only symmetry element common to the well known R (space group *R3m*) and T (space group *P4mm*) phases, and can be viewed as a bridge between these two structures. In subsequent work, the lattice parameters were measured as a function of temperature and composition (34; 32), and a phase diagram around the morphotropic region was proposed, as shown in Fig. 1.3. First-principles calculations reproduced the stability of the monoclinic phase in a narrow region at the MPB when a random Zr/Ti cation distribution was taken into account (35). The stability of a monoclinic phase of space group *Cm* (the so-called $M_A$ phase) in between the R and T phases was also explained using a Landau-Devonshire approach (36).
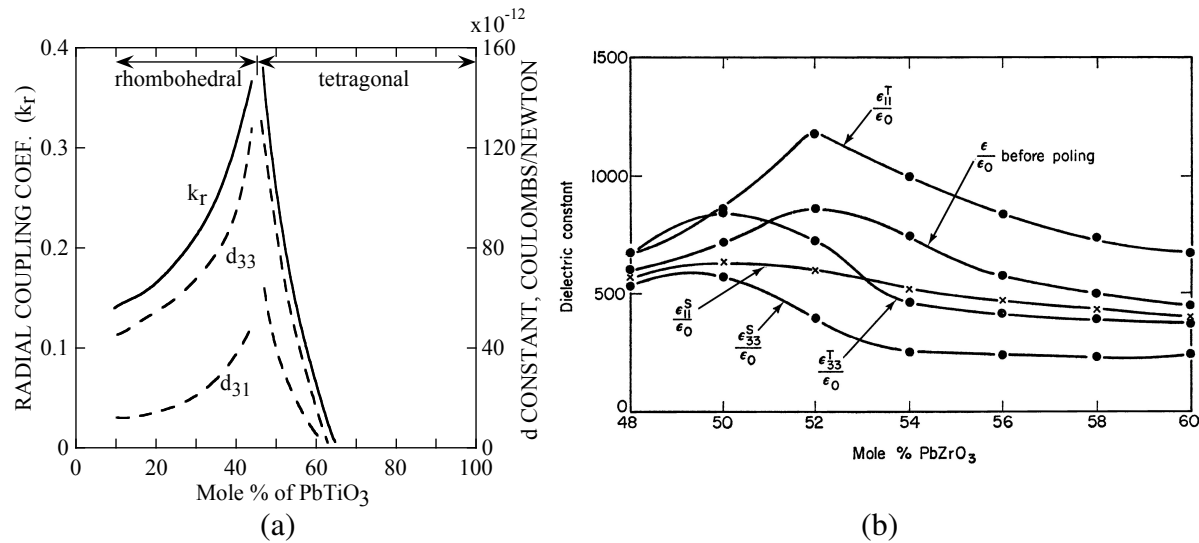
PZT ferroelectric ceramics are not completely periodic in three-dimension because they contain domains with distinct polarization directions. Domain structure strongly influences x-ray diffraction patterns (12). The Rietveld refinement based on three dimensionally periodic structures can only result in a structural model, which is an idealized assumption of the structure present. All the real structure and local structure information accessible should be discussed in context with structural information derived from diffraction data. Single crystals of PZT are not available and thus no experimental information exists of the near-ideal structure.

Khachaturanyan and coworkers discussed the interference effects between the domains in terms of the martensitic theory (37; 38; 39). They stated that the lattice parameters of the monoclinic phase calculated using Rietveld refinement are directly dependent on the lattice parameters of the tetragonal and cubic parent phases and are just an average over miniaturized tetragonal nanodomains, which can reach up to tens of nanometers without being able to diffract incoherently.

Schönau *et al* investigated PZT samples with composition near MPB using high-resolution synchrotron x-ray diffraction in combination with transmission electron microscopy (TEM) and

electron paramagnetic resonance (EPR) to correlate average structure and microstructural infor-
mation (40). It is shown that the appearance of intensity in diffraction patterns formerly linked
to a monoclinic phase can directly be correlated to a miniaturization of the average domain
structure of the material visible in the presence of nanodomains (41; 42). The internal symme-
try of the nanodomains is not necessarily monoclinic due to coherence effects in diffraction.
The same authors later concluded that material within domains is monoclinic (43).

### 1.2.3   Piezoelectric and dielectric properties



**Figure 1.4:** Variation of room temperature piezoelectric and dielectric properties with composition for
Pb($Zr_{1-x}Ti_x$)$O_3$ ferroelectric ceramics. (a) piezoelectric coefficients $d_{33}$, $d_{31}$ and radial electromechani-
cal coupling factor $k_r$ (44); (b) dielectric constants (45).
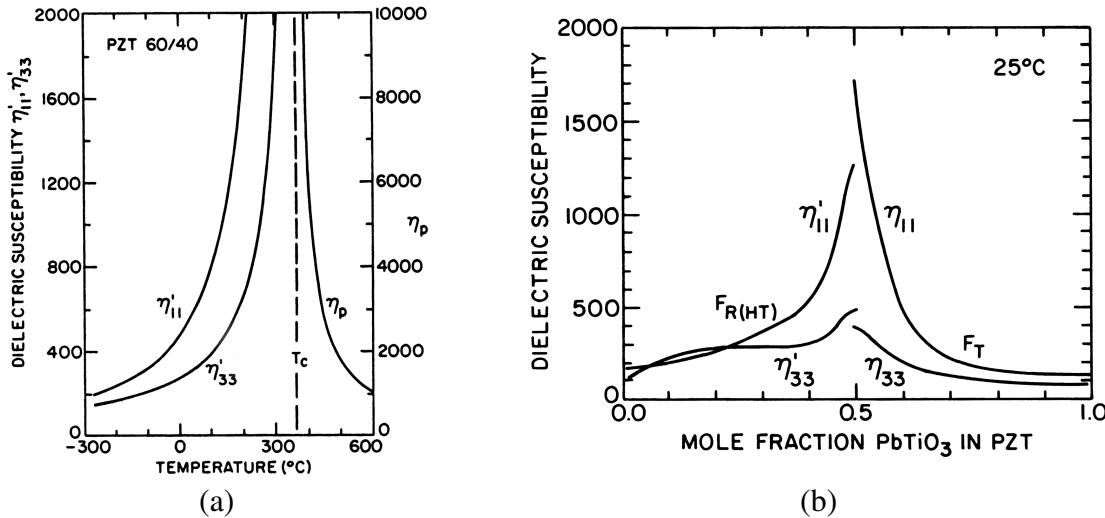
According to the earliest investigations of the piezoelectric properties of Pb($Zr_{1-x}Ti_x$)$O_3$
ferroelectric ceramics (44; 21), strong piezoelectric effects were discovered in the composi-
tions near MPB, as shown in Fig. 1.4(a). Since the MPB is almost independent of temperature,
the temperature dependence of the electromechanical properties is practically free of polymor-
phic irregularities in contrast with BaTiO$_3$. The compositions in tetragonal phase were not
successfully poled, whereas superior piezoelectric effects were readily induced throughout the
compositions in rhombohedral phase.

Much stronger piezoelectric coupling was observed in subsequent works, because of the
improvements both in ceramic quality and poling technique (45; 46). Maximum planar cou-
pling factor over 0.6 at room temperature have been achieved both in undoped and doped PZT
compositions. Their piezoelectric properties are substantially stronger and more useful than
the BaTiO$_3$ compositions. Because of the high T$_C$ (typically above 360 °C), the properties are
relatively stable over a much wider temperature range.

The dielectric properties of Pb($Zr_{1-x}Ti_x$)$O_3$ ferroelectric ceramics as a function of com-
positions near the MPB is shown in Fig. 1.4(b) (45; 2). Among all studied compositions, the

highest value is obtained in the composition with $x=0.48$. Note that the dielectric constants have their highest values just on tetragonal side of the transition, while the piezoelectric constants maintain their high values on rhombohedral side.

## 1.2.4 Intrinsic and extrinsic contributions



**Figure 1.5:** (a) Single domain dielectric properties as a function of temperature calculated for Pb(Zr$_{1-x}$Ti$_x$)O$_3$ composition with $x=0.4$; (b) Single domain dielectric properties as a function of Zr/Ti ratio. Taken from Haun *et al* (47).
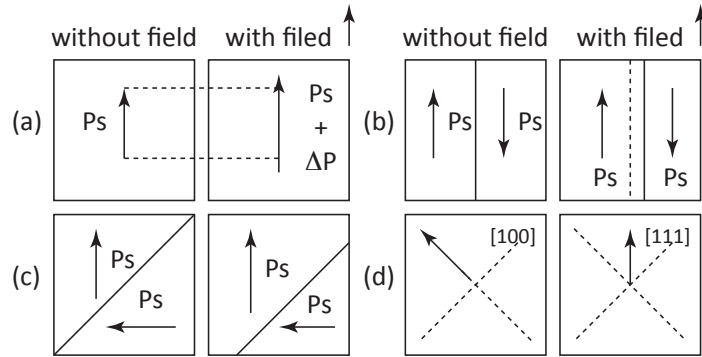
A lot of works have been conducted to understand the anomalous dielectric and piezoelectric properties of PZT ferroelectric ceramics. Those approaches are mainly divided into two categories in terms of intrinsic and extrinsic contributions. In the literature, the physical properties determined from a single domain state ferroelectric material are denoted as the intrinsic properties (or volumetric contribution) of the material, while the contributions from other parts of the materials, mainly from domain walls, are considered as extrinsic properties of the material. (48; 49; 50; 51)

A complete Landau-Ginsburg-Devonshire phenomenological theory has been developed to describe the intrinsic properties of BaTiO$_3$. (52; 53; 54) The coefficients of the energy function could be extracted from the measurements on single domain state BaTiO$_3$ single crystals. In PZT ferroelectric ceramics, however, the situation becomes much more complex. Besides the complexity of the phases existing in the PZT system, the more important constrain results from the lack of high quality PZT single crystal samples. The coefficients of the energy function of PZT compositions could only be obtained by indirect methods, except the compositions close to pure PbZrO$_3$ and PbTiO$_3$.

After 10 years continuing effort, the ferroelectric group at the Pennsylvania State University has successfully formulated an adequate phenomenology theory to describe the intrinsic properties of PZT system. (55; 56; 57; 58; 59; 24; 47; 60) Based on the phenomenological calculations of the free energy vs. composition, a phase diagram deduced from the crossing points

of the phase stability lines for the whole compositions-temperature field is obtained, which is in good agreement with the phase diagram shown in Fig. 1.2. The dielectric and piezoelectric properties as a function of temperature and composition were also deduced (Fig. 1.5). The highest values of those physical properties were observed in the compositions near MPB.

Due to the random orientation of grains and internal stresses generated by switching the large spontaneous strains during poling, even in the best poled PZT ceramic the sample does not come to an ensemble of single domain grains. For example, in considering the polarizability of the ceramic in its ferroelectric phases, we should take into account the extrinsic contributions due to the changes in the polar domain structures and phase makeup brought about by the field. The type of changes occurring which could contribute to the polarizability are shown schematically in two dimensions in Fig. 1.6. Here the domain walls are divided into two groups: 180° and non-180° domain walls. Note that 180° domain walls are purely ferroelectric and they will not couple to mechanical stress. On the other hand, non-180° domain walls are both ferroelectric and ferroelastic. It is this difference that makes them distinguishable when the quantities related to the mechanical strain of the samples are measured (48).
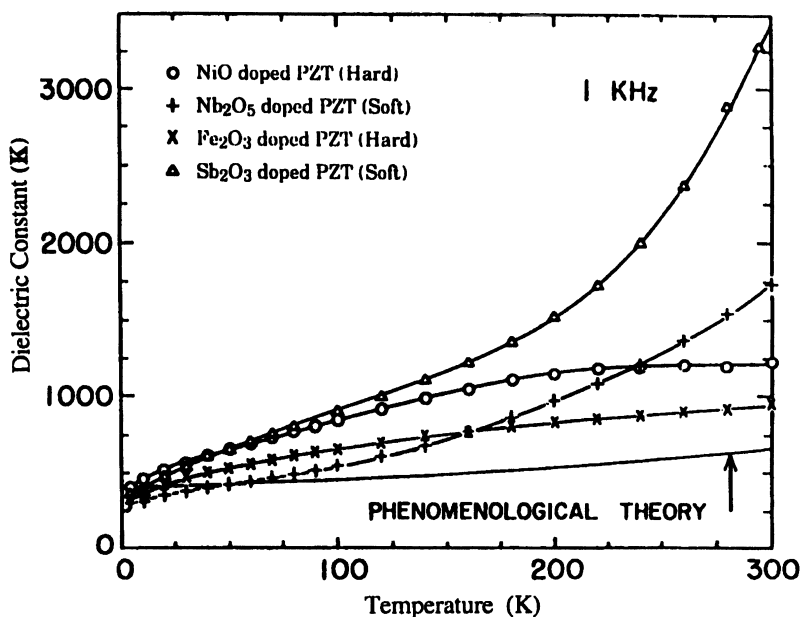


**Figure 1.6:** Possible mechanisms which can contribute to the dielectric polarizability in a ferroelectric PZT ceramic with composition near MPB. (a) Intrinsic single domain; (b) 180° domain wall motion; (c) Ferroelastic domain wall motion; (d) Ferroelectric phase change. Taken from Cross (61).

The works by Arlt *et al* qualitatively indicate that the domain wall motion plays an important role in the dielectric and piezoelectric properties of ferroelectric ceramics (62; 63; 64; 65). Then, Zhang *et al* proposed an experimental method to directly and quantitatively determine the intrinsic and extrinsic contributions in PZT ferroelectric ceramics, basing on the fact that domain wall motion does not produce volumetric changes (49). By means of this method, the contributions from both intrinsic and extrinsic part as well as their temperature dependence are evaluated. The data suggested that extrinsic domain wall motion makes up a major contribution to the dielectric and piezoelectric properties at room temperature (larger than 50%). Note that the domain wall motion is limited to the action induced by weak external driving field, since strong fields would induce domain wall switching, which may introduce significant local stress and result in volume change.

### 1.2.5   Softening and hardening

The research of the doping effects on PZT system has been conducted as early as the late 1950s. (66; 67; 68; 69). It is shown that the dielectric and piezoelectric properties of PZT fer-roelectric ceramics could be readily tailored by means of low level doping, especially through the aliovalent dopants. In general, these aliovalent dopants fall into two distinct groups. The soft donor dopants where the charge on the cation is larger than that which it replaces in the PZT structure and hard acceptor dopants where the charge on the cation is smaller than that of the ion which it replaces.

The donar dopants enhance both the dielectric and piezoelectric properties at room temper-ature, and show symmetric hysteresis loops with good "squareness" and lower coercivity with respect to the high fields. The acceptor dopants in general reduce both dielectric and piezo-electric properties, they give rise to highly asymmetric hysteresis response, larger coercivity and higher electrical and mechanical quality factor ($Q$). A detailed summary of those doping effects could be found in Ref. (2).



**Figure 1.7:** Temperature dependence of the dielectric constant of soft and hard PZT ferroelectric ceram-ics measured from 4.2 to 300 K. The experimental data are after Zhang *et al* (70). The theoretical curve of an average of the single crystal values is calculated by assuming a tetragonal solution to the energy function. Taken from Randall *et al* (50).

Instead of influencing the intrinsic contributions, it is believed that those dopants change the dielectric and piezoelectric properties mostly by means of the interactions with the domain walls. As shown in Fig 1.7, dielectric constants of studied soft and hard PZT ceramics[5] show a

---

[5]The PZT ceramic samples used in this measurement have the same Zr/Ti ratio as 52/48, however the doping level is unknown since the ceramic samples are obtained from a commercial company. More information could be found through the link: http://www.bostonpiezooptics.com/?D=26.

large difference at room temperature. However, their dielectric constants decrease by decreasing the temperature and convert to almost the same value at liquid helium temperature. The data measured at 4 K agree quiet well with the intrinsic dielectric properties calculated from the average of the single domain values deduced from the phenomenological theory for that composition.
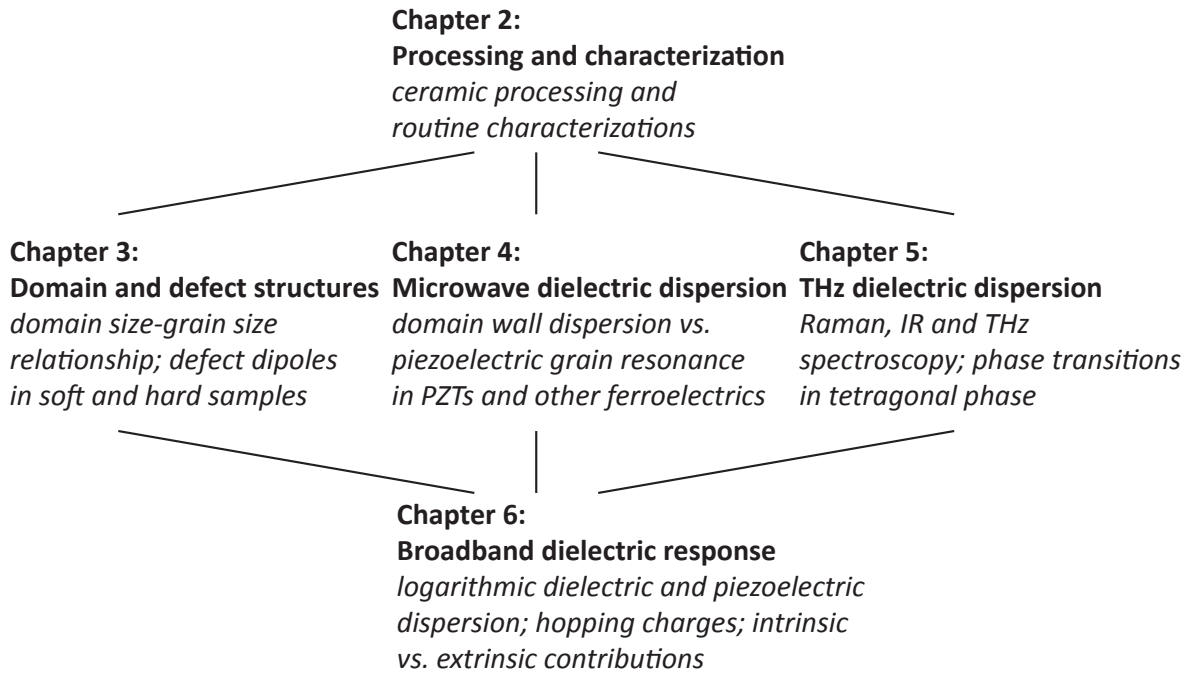
It is known that in hard PZT ceramics properties decrease with time. This behavior is termed as "aging". In contrast, this aging effect could not be detected in soft materials (2). Understanding origin of aging in hard and its absence in soft materials may thus help identifying details of hardening and softening mechanisms. It is believed that the hardening mechanism is associated with the domain wall stabilization. However, the exact mechanism dominating the stabilization of the domain walls is still disputable (71; 72; 73; 74; 75; 76; 77; 78). Three main models are usually discussed in the literatures: (I) the bulk effect (caused by alignment of charged defects with polarization within ferroelectric domains) (72; 74; 76), (II) the domain wall effect (diffusion of charges toward domain walls thus creating pinning centers) (79; 80; 81) and (III) surface effect (drift and gathering of charges near grain boundaries and other interfaces). The bulk and domain walls models are based on results of experimental studies (72; 82; 83; 84; 73; 74; 76; 77), while the dominating contribution of surface (interface) effect was proposed by modeling in Refs. (72; 78; 85).

For soft PZT samples, the structure of defects induced by donor doping is sill not clear. What is more important is to clarify the relationship between those defects or defect dipoles and the domain walls. There are only "hand waving" arguments as to how or why the domain walls should become more mobile in soft mateirals. Much more work is needed to determine the physics of the softening in these materials.

## 1.3   Goals of the thesis

It has been shown that materials with "soft" and "hard" characteristics could be obtained by introducing the donor and acceptor dopants in PZT. Those dopants and corresponding defect vacancies may form defect dipoles. The softening and hardening effects are mainly manifested in the changes in the extrinsic domain wall contributions, which are strongly associated with the interactions between the domain walls and defect dipoles. However, interaction of the domain walls and defects in soft and hard PZT ceramics are not fully understood.

Understanding of the dynamic domain wall response to the weak external driving field (electrical or mechanical) is important, because the frequently discussed dielectric and piezoelectric properties are measured in such experimental environment and these materials are often used under weak driving signals. In weak fields, it is assumed that domain walls move near the equilibrium sites instead of switching and moving over long distances. This weak field movement dominates dielectric and piezoelectric properties. Whereas domain switching at high fields is rather well understood, the knowledge of domain wall motion at weak fields is still not sufficiently developed.

**Chapter 2:**
**Processing and characterization**
*ceramic processing and*
*routine characterizations*

**Chapter 3:**
**Domain and defect structures**
*domain size-grain size*
*relationship; defect dipoles*
*in soft and hard samples*

**Chapter 4:**
**Microwave dielectric dispersion**
*domain wall dispersion vs.*
*piezoelectric grain resonance*
*in PZTs and other ferroelectrics*

**Chapter 5:**
**THz dielectric dispersion**
*Raman, IR and THz*
*spectroscopy; phase transitions*
*in tetragonal phase*

**Chapter 6:**
**Broadband dielectric response**
*logarithmic dielectric and piezoelectric*
*dispersion; hopping charges; intrinsic*
*vs. extrinsic contributions*

**Figure 1.8:** Thesis chapter structure. The main achievements of each chapter are summarized below the titles.

The goal of this thesis is to deepen understanding of the hardening and softening mechanisms in PZT by investigating dielectric properties over a wide frequency range. Hardening and softening are intimately related to domain structure, domain wall mobility and interaction of domain walls with the defects. The interaction of domain walls with defects is expected to be frequency dependent and such a study can help understanding dynamic effects behind the softening and hardening mechanisms. In order to reach this objective, the dielectric responses of soft and hard PZT ceramic samples is evaluated by means of the broadband dielectric spectroscopy. This tool is very powerful in separating contributions from different polarization mechanisms. Information on both intrinsic and extrinsic contributions can thus be obtained. To correlate dielectric properties with the domain structures, soft and hard PZT ceramic samples are studied by transmission electron microscopy. Together, these studies are expected to lead to a general description of the softening and hardening effects on dielectric properties.

The chapters of the present text correspond to the main steps outlined above and are schematically presented in Fig 1.8. Each chapter would be devoted to a core topic, and support materials would be discussed around this topic.

# Chapter 2

# Processing and characterization

## 2.1 Introduction

The processing of PZT ceramics has been refined and several routes were proposed since the discovery of very high properties in PZT ceramics with composition near the MPB. The objective of the work described in this chapter is not to develop an innovative way to synthesize PZT samples, but rather to obtain good and reproducible samples which possess uniform microstructure for various compositions allowing for comparison of properties independently of processing issues. Basic characterizations, such as density, phase structure, microstructure, dielectric properties and ferroelectric properties also will be presented in this chapter.
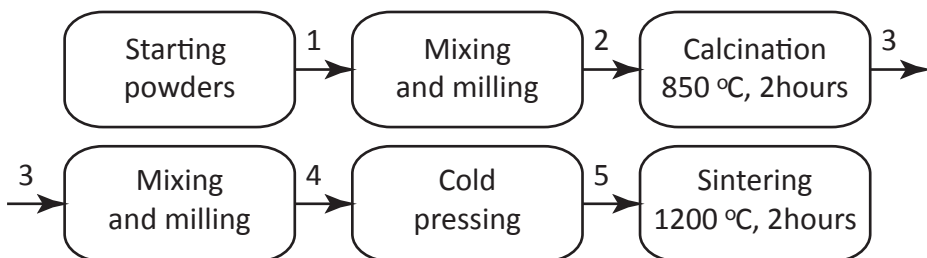
## 2.2 Composition selection

To a selected $Pb(Zr_{1-x}Ti_x)O_3$ composition, both the softening and hardening effects can be generated by partially substituting A- or B-site ions with the donor and acceptor ions. Therefore the first step to prepare the soft and hard PZT ceramics is to choose the basic compositions for doping. According to the phase diagram of PZT solid solution, three representative phase regions (rhomboderal, tetragonal and MPB regions) are of interest in this thesis. The corresponding Zr/Ti mole ratio of those three compositions were set as (58/42), (42/58), and (52/48), respectively. Due to the complications with the presence of mixed or monoclinic phases near the MPB, much of the work was concentrated on the compositions corresponding to pure rhombohedral (58/42) and tetragonal (42/58) phases.

For each basic composition, soft and hard samples were prepared by partially substituting the (Zr,Ti) site ions with $Nb^{5+}$ (donor) and $Fe^{3+}$ (acceptor) ions, respectively. For the compositions in rhombohedral and tetragonal phases, the doping level was set as 0.2, 0.5 and 1.0 at. % for soft samples, and 0.1, 0.5 and 1.0 at. % for hard samples. To the MPB composition, the doping level was set as 1 at. % for both soft and hard samples. For the sake of convenience, the samples are labeled in the following manner: for example, PZT(52/48)Fe1.0 refers to the nominal formula $Pb(Zr_{0.52}Ti_{0.48})_{0.99}Fe_{0.01}O_3$, etc.

## 2.3   Bulk ceramic processing

The mixed oxide route is the most common route to synthesize PZT ferroelectric ceramics. It was adopted since the first synthesis of PZT solid solutions by Shirane *et al* (18; 19; 20) and the first determination of the full PZT phase diagram (86). Later, the discovery of very high electro-mechanical properties at MPB by Jaffe and his coworkers was also made on the samples prepared by a similar method (44). The main steps of the mixed oxide route are summarized in Fig. 2.1.



**Figure 2.1:** Flow chart of the mixed oxide route for synthesis of PZT ceramics.

Oxide powders were used as raw materials to synthesize PZT ceramics. The purity, particle size and manufacturers of the oxide powders used in present work are summarized in Table 2.1. The particle size was determined by a Horiba CAPA-700 particle size distribution analyzer. Here, the *particle size* refers to the median particle size ($D_{50}$), which means that 50 % of the particles are below these sizes according to the volumetric distribution of the particle sizes.

**Table 2.1:** Component oxide powders used in synthesis of PZT ceramics.

| Materials | Grade | Particle size | Manufacturer |
|---|---|---|---|
| Lead oxide (PbO) | 99.9+ % | 4.78 µm | Sigma-Aldrich GmbH |
| Zirconium dioxide ($ZrO_2$) | 99.96 % | 0.73 µm | Tosoh Corporation |
| Titanium dioxide ($TiO_2$) | 99.8 % | 0.95 µm | Alfa Aesar GmbH |
| Niobium pentoxide ($Nb_2O_5$) | 99.9 % | 0.45 µm | Alfa Aesar GmbH |
| Iron (III) oxide ($Fe_2O_3$) | 99.945 % | 0.30 µm | Alfa Aesar GmbH |

Starting powders were weighed according to the desired composition, then dispersed in isopropanol and mixed by a planetary milling machine for 6 hours with cylindrical $ZrO_2$ media. A typical mill consisted of 120 g of powder, 75 ml isopropoanl and 300 g media. After milling the mixtures were dried in glass beakers at approximately 50 °C to increase the evaporation rate of the solvent.

Powders were calcined in a high density alumina crucible which was loosely covered with an alumina plate. The powders were calcined at 850 °C for 120 minutes with a heating rate of 5 °C/min. Calcined powders were milled in a similar manner to the first milling but with less isopropanol (65 ml), for better particle size (or agglomerate size) reduction.

A 5 % polyvinyl alcohol (PVA) water solution was used as binder to increase the plasticity of the powders. The weight ratio between the PVA solution and the powders was 1:20. Powder and PVA solutions were mixed in a mortar and then uniaxially pressed into pellets with a pressure of 125 MPa in cylindrical stainless steel dies. The size of those pellets was 10 mm in diameter, while the thickness varied from 2 to 7 mm, according to requirement of the corresponding measurement.

Pellets were packed into the covered alumina crucibles. The inner space of the crucibles was filled up with the powders of the same compositions as the pressed pellets, in order to prevent intensive evaporation of the lead during the sintering. A typical sintering schedule consisted of a hearting rate of 3 °C/min, a dwell for 120 minutes at 600 °C (to release the organic binder), 3 °C/min to 1200 °C for 120 minutes and natural cooling in the furnace.

## 2.4 Basic characterization
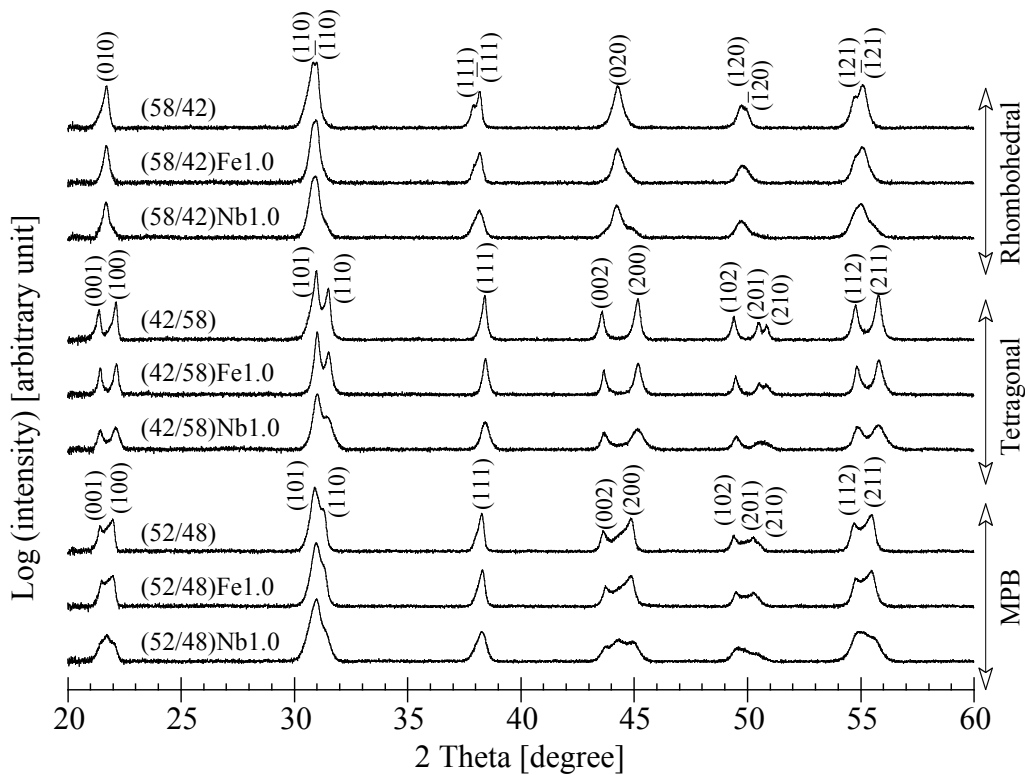
### 2.4.1 Density

The density of all studied samples was determined based on Archimedes' principle. The weight of the sample in air ($m_1$) was measured by a Mettler PM200 analytical balance. Then a beaker containing distilled water with a fixture was placed on the balance. The sample was suspended in the water by this fixture. Before dipping the sample into the water, the balance was reset to zero. The weight measured in water is referred to $m_2$. The density of the sample was calculated according to ($m_1/m_2 \times \rho$), where $\rho$ is the density of distilled water. In order to increase the accuracy, heavy samples ($>3$ g) were used for the measurement. In this thesis, we assume that the theoretical density of all studied PZT ceramics is 8 g/cm$^3$. The results suggest that the relative density of all studied sample was above 96% at least.
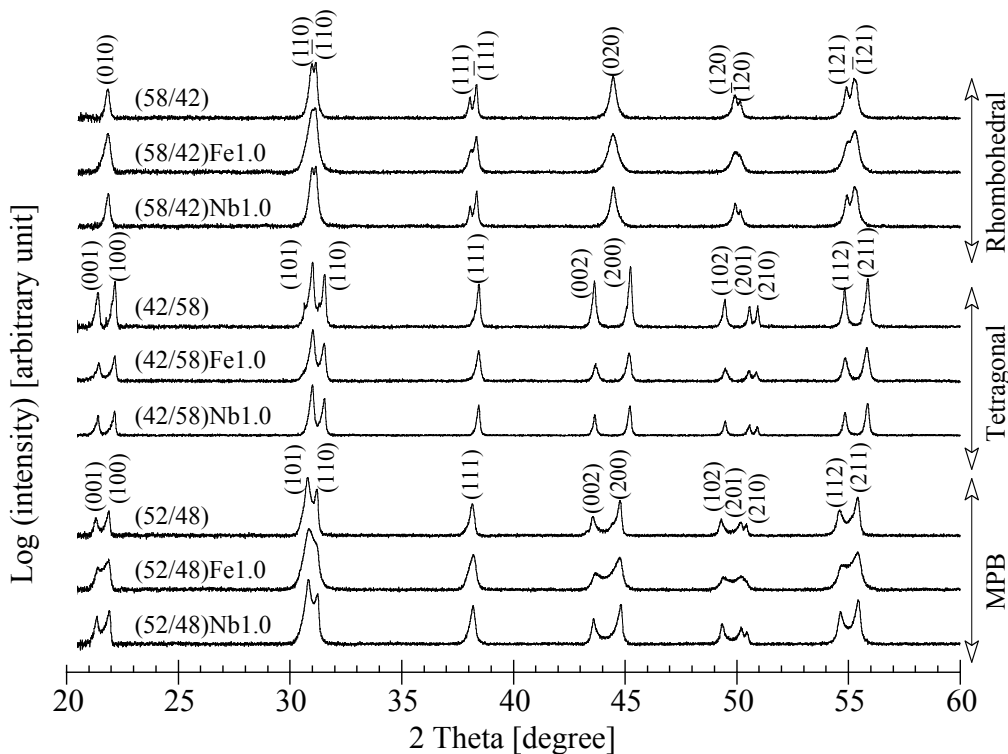
### 2.4.2 X-ray diffraction

The crystalline purity was checked by X-ray diffraction (XRD) analysis. Room temperature $\theta$-$2\theta$ coupling scannings were conducted on a Bruker D8 X-ray diffractometer from 20° to 60° with a step of 0.01°. Powder diffraction files (PDF) for the compositions in rhombohedral (PbZr$_{0.58}$Ti$_{0.42}$O$_3$, # 01-073-2022), tetragonal (PbZr$_{0.40}$Ti$_{0.60}$O$_3$, # 01-070-4056) and MPB (PbZr$_{0.52}$Ti$_{0.48}$O$_3$, # 01-070-4060) regions were used to index the diffraction peaks detected from the scanning.

Fig 2.2 show the XRD spectra of calcined PZT powders with selected compositions in rhombohedral, tetragonal and MPB regions. These calcined powders show a distinct pseudo-cubic perovskite structure with the appropriate peak splittings expected from the non- centrosymmetric ferroelectric phases. No spurious peaks associated with pyrochlore phases are detected. However, given the high detection threshold for XRD, second phase absence cannot be strictly proven here. For the compositions with the Zr/Ti ratio of 58/42, typical rhombo-

**Figure 2.2:** Representative XRD spectra of calcined PZT powders with compositions in rhombohedral, tetragonal and MPB regions.



**Figure 2.3:** Representative XRD spectra of sintered PZT powders with compositions in rhombohedral, tetragonal and MPB regions.
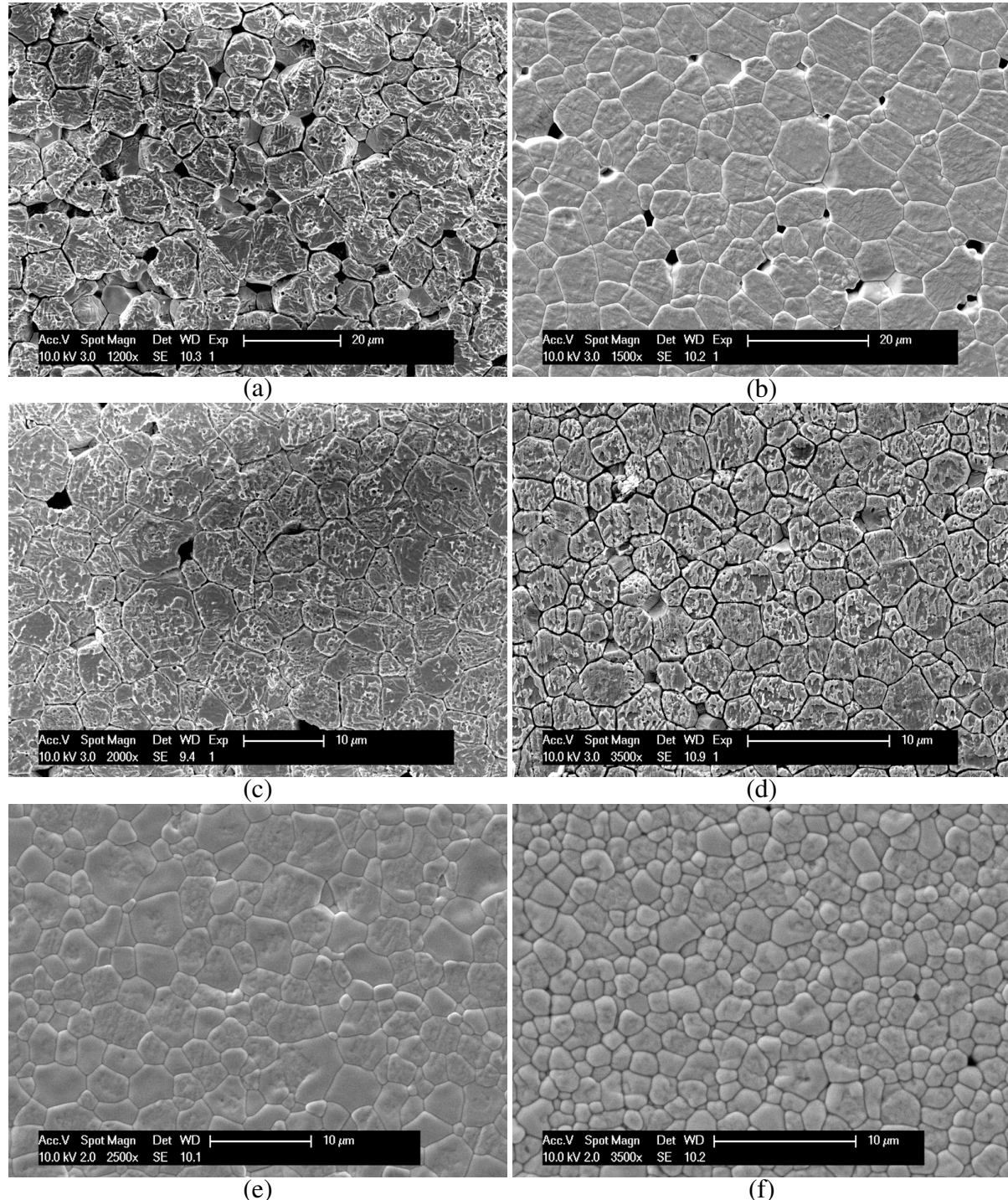
hedral structures are detected in undoped, soft and hard PZT powders. The strongest peak splittings reflected in the {110}, {111}, {120} and {121} planes are observed in PZT(58/42). For PZT(58/42)Fe1.0 and PZT(58/42)Nb1.0, although no clear peak splittings are detected in the same peak groups, obviously asymmetric peaks in those groups still suggest a rhombohedral structure. For the compositions with the Zr/Ti ratio of 42/58, expected tetragonal structures are indentified by the peak splittings in the {001}, {101}, {002}, {102} and {112} planes. Also strongest peak splittings are observed in undoped PZT(42/58). The phase structure in the MPB region is complicated due to the coexistence of the rhombohedral and tetragonal phases. For PZT(52/48) and PZT(52/48)Fe1.0, typical tetragonal characteristics are reflected by the peak splittings of {001} and {002} planes. In PZT(52/48)Nb1.0, however, a third strong peak observed in the {001} and {002} planes suggest that the rhombohedral structure is predominant in the calcined powders.

Sintering effects on the PZT crystalline structure are shown in Fig 2.3. Generally, peaks are getting sharper in agreement with a better crystallization or compositional homogenization due to high temperatures. No spurious peaks associated with pyrochlore phases are observed. For the compositions with the Zr/Ti ratio of 58/42, all the samples show pronounced peak splittings in the {110}, {111}, {120} and {121} planes. The single peaks in the {010} and {020} also become much symmetric compared of the scanning patterns from the calcined powders. For the compositions with the Zr/Ti ratio of 42/58, the tetragonal structures of all the samples manifested wider peak splittings in the {001}, {101}, {002}, {102} and {112} planes. Especially in the {102} plane, three diffraction peaks can be well distinguished from the scanning patterns. For the compositions with the Zr/Ti ratio of 52/48, undoped and soft samples display strong peak splittings in the {001} and {002} planes, which suggest that the tetragonal strictures are dominant. However, the relatively small peak splittings in those plane of the PZT(52/48)Fe1.0 indicates the a high concentration of the rhombohedral phase. The phase coexistance in the MPB region will be discussed in Chapter 3.

### 2.4.3 Microstructure
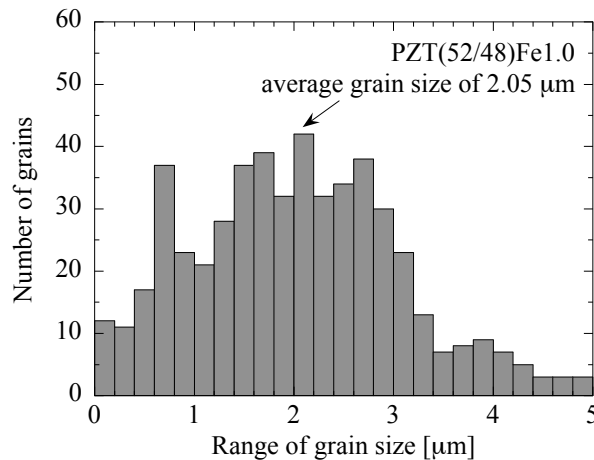
Microstructural features such as grain size, grain boundary, and pores were characterized by means of scanning electron microscopy (SEM). The samples used for SEM observation were polished down to optical quality. Depending on the samples, different etching methods were used to reveal grain boundaries. For hard PZT ceramic samples, 5% HCl solution with 5 drops of HF per $100\,cm^3$ of solution was used. For soft PZT ceramic samples, grain boundaries in good contrast were observed after thermal etching at $1050\,°C$ for 30 minutes in air. For undoped PZT ceramic samples, either chemical or thermal methods were used. Before the SEM observation, a layer of gold (about $20\,nm$) was deposited on the etched surface by sputtering to avoid the electron accumulation on the sample surface. A FEI XL30-SFEG scanning electron microscopy was used to conduct the observations.

Several representative microstructures of undoped, hard and soft PZT ceramic samples are

**Figure 2.4:** Polished and etched surfaces of several representative PZT ceramic samples (a) PZT(58/42) (chemical etching); (b) PZT(52/48) (thermal etching); (c) PZT(58/42)Fe0.1 (chemical etching); (d) PZT (42/58)Fe1.0 (chemical etching); (e) PZT(58/42)Nb1.0 (thermal etching); (f) PZT(42/58)Nb1.0 (thermal etching).

shown in Fig 2.4. From those SEM images, no second phase can be observed, as suggested by XRD analysis. The porosity is low. In general among all studied samples, undoped PZT ceramics possess the larger grains ranging from 10 to 20 μm. Both soft and hard samples show relatively small grain size. For samples in 1 at.% doping level, the average grain size is less than 5 μm. Our results are consisted with the previous report by Morozov (87). By means of doping, the grain size of PZT ceramics could be adjusted. This observation is very useful, especially when we discuss the microwave frequency dispersion in Chapter 5.
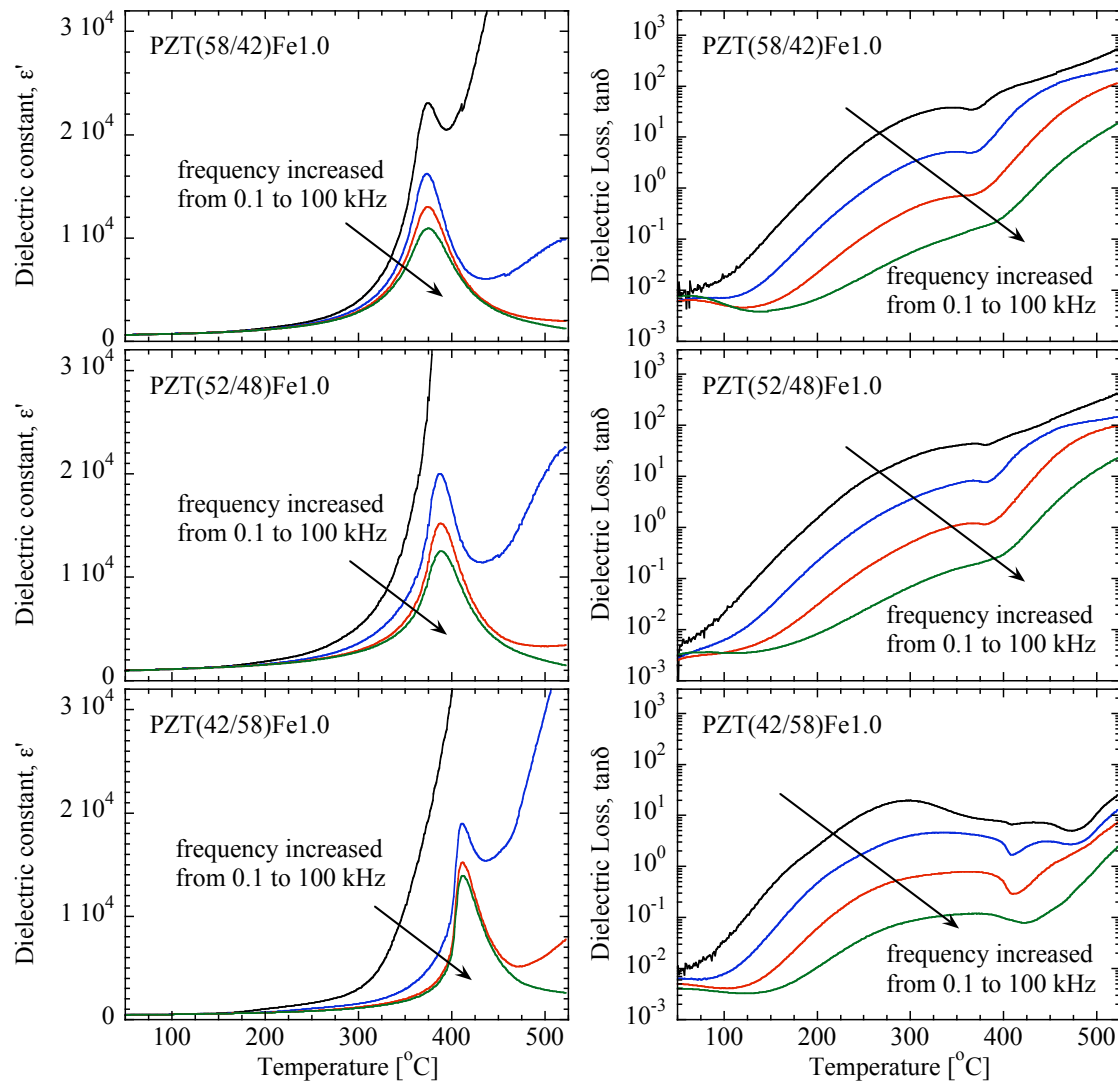


**Figure 2.5:** Histogram of grain size distribution of PZT(52/48)Fe1.0.

In order to define the grain size quantitatively, the SEM images collected on polished and etched samples were processed by means of IMAGEJ software package[1]. As a result we obtained the cross-section area on the plane of polish $A_{cs}$ for individual grains. Further, the equivalent grain diameter was introduced as $D_e = 2\sqrt{A_{cs}/\pi}$. The distribution of $D_e$ was found to be unimodal for all compositions. Corresponding probability plots reveal quite good agreement with the log-normal distribution for a number of samples, while minor right-skew deviations were evident for some samples (Fig 2.5). At this point, one needs to note that $A_{cs}$ and $D_e$ describe random cross section of a grain. It is obvious, therefore, that they underestimate its three-dimensional extent. To overcome this problem we adopt here the approach developed by Mendelson (88). Assuming particular grain shape, it relates average grain size to the average intercept length $\overline{L}$ by a proportionality constant. In the present study, 1.56 was used as such correction factor (88), which was applied to the average value of $D_e$, instead of $\overline{L}$. It is justified in our view, as $\overline{D_e}$ turns out to be very close to roughly estimated. We will show the comparison between $\overline{D_e}$ and $\overline{L}$ in Chapter 5.

## 2.4.4   Temperature dependence of dielectric properties

Characterization of dielectric constant as a function of temperature is the most common tool to observe phase transition in ferroelectric system. The measurements performed at various

---
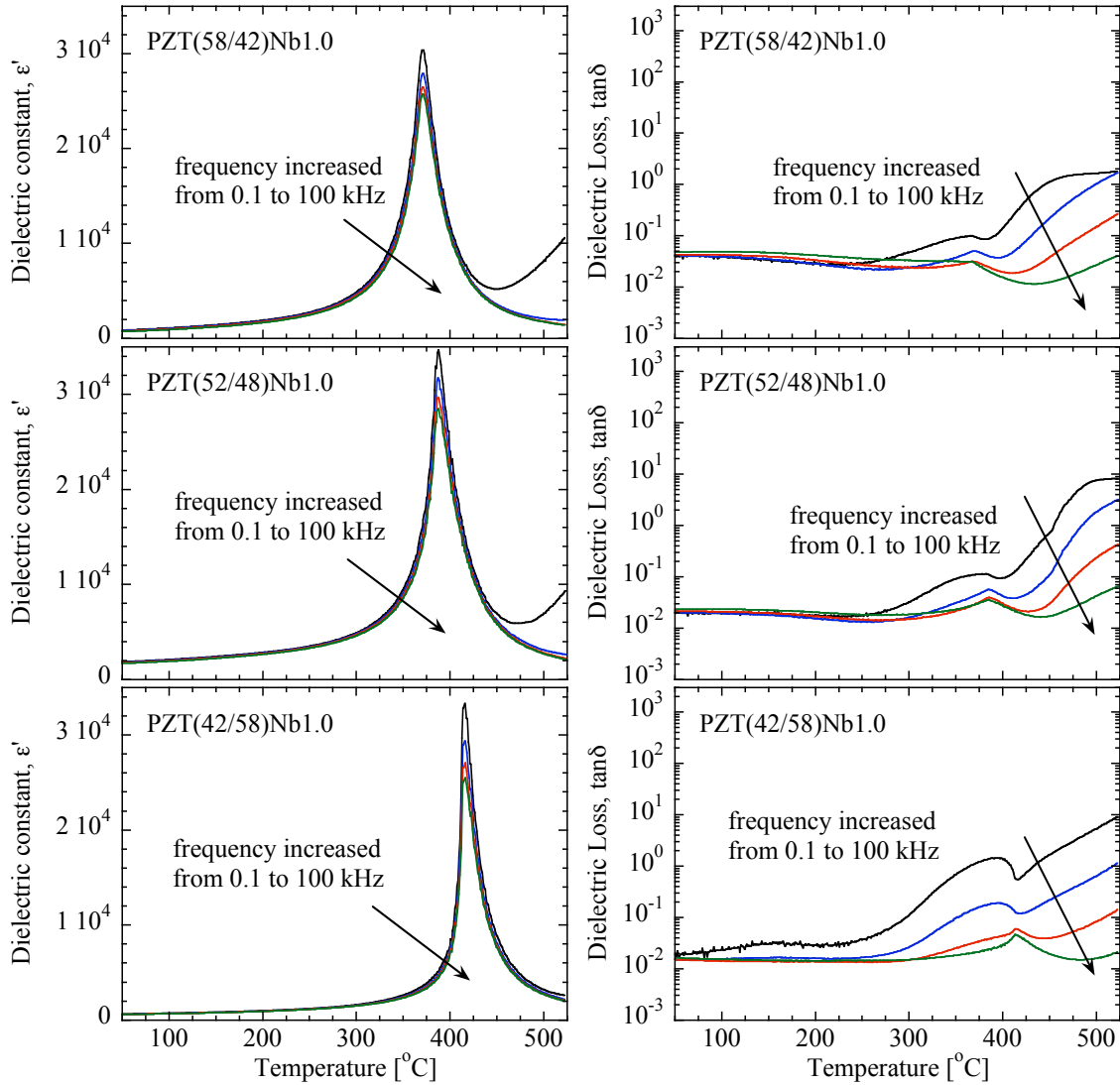
[1]ImageJ is available at http://rsbweb.nih.gov/ij/.

**Figure 2.6:** Temperature dependences of permittivity and loss for $Fe^{3+}$-doped hard PZT ceramic samples in rhombohedral, MPB and tetragonal regions. Measurements were performed at 0.1 kHz, 1.0 kHz, 10 kHz and 100 kHz upon heating.

frequencies and characterization of the dielectric loss gives some additional information on the dielectric properties of the material, for example, the conductivity. The dielectric measurements were performed using a HP 4284A *LCR* meter connected to the electroded sample with platinum probes. Samples were heated in a minifurnace with heating rate 2 °C/min; the temperature was controlled by a thermocouple contacting the sapphire sample holder near where the sample was situated. Without specification, the dielectric properties shown in this section were measured at several discrete frequencies from 0.1 kHz to 100 kHz upon heating in unpoled state.

Three 1 at. % $Fe^+$-doped hard PZT ceramic samples in rhombohedral, MPB, and tetragonal regions have been characterized with the described dielectric measurements. The results are shown in Fig 2.6. The losses at higher temperatures are extremely high and are evidence of high conductivity and related dielectric dispersion that has well pronounced frequency depen-
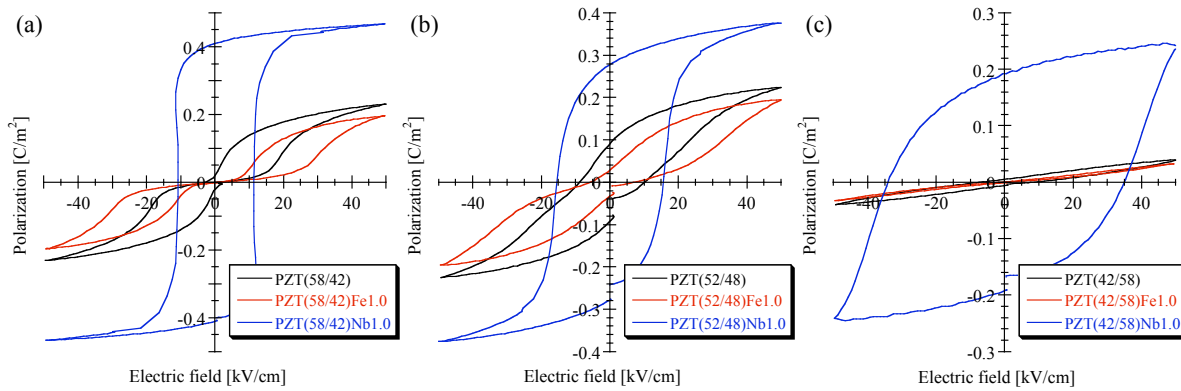
**Figure 2.7:** Temperature dependences of permittivity and loss for $Nb^{5+}$-doped soft PZT ceramic samples in rhombohedral, MPB and tetragonal regions. Measurements were performed at 0.1 kHz, 1.0 kHz, 10 kHz and 100 kHz upon heating.

dence. The rapid increase of permittivity measured at 0.1 kHz shields the characteristic of the phase transition, especially in PZT(52/48)Fe1.0 and PZT(42/58)Fe1.0. However, the dielectric response measured at higher frequencies (1 kHz, 10 kHz and 100 kHz) is strong enough to observe the ferroelectric phase transition and Curie-Weiss behavior. The conductivity dominates the relatively high dielectric response at lower frequencies, so the measurements performed at lower frequency are not precise enough to determine the dielectric part of the response, which results in very high apparent values of the dielectric permittivity. If this effect is attributed to oxygen vacancy diffusion, it is probable that the related diffusion coefficient is higher for tetragonal compositions. (4)

In comparison with the permittivity and loss of the $Fe^{3+}$-doped hard PZT, the dielectric properties of the $Nb^{5+}$-doped hard PZT ceramic samples reveal the absence of the frequency dispersion below $T_C$, as shown in Fig 2.7. It gives further support to the assumption that oxy-

gen vacancies contribute to the conductivity, as their concentration is reduced in donor-doped ceramics.

### 2.4.5 Ferroelectric hysteresis loop



**Figure 2.8:** Room temperature ferroelectric hysteresis loops for representative undoped, hard and soft PZT ceramics in (a) rhombohedral, (b) MPB and (c) tetragonal regions.

Measurement of the ferroelectric hysteresis loop is the easiest way to distinguish the soft and hard effects in PZT ceramics. Fig 2.8 shows the room temperature ferroelectric hysteresis loops for undoped, hard and soft PZT ceramics in rhombohedral, MPB and tetragonal regions. In each phase region, expected soft and hard characteristics are observed and are consistent with previous works (87). Due to the pinning effect of defect dipoles, the hard PZT exhibits as a strongly pinched loop. For soft PZT, a square loop with a relatively small coercive field is observed. For undoped PZT, due to impurities, which cannot be eliminated from the raw materials, or lead vacancy-oxygen vacancy dipoles, the hysteresis loops are qualitatively similar to those of hard PZT (3).

## 2.5 Defect structures

In order to deepen the understanding of the hardening and softening mechanisms, defect structures are tentatively studied by electron paramagnetic resonance (EPR) and positron annihilation lifetime spectroscopy (PALS) in cooperation with Prof. Eichel's group at Universität Freiburg and Prof. Keeble's group at University of Dundee, respectively.

### 2.5.1 Defect structures in hard PZT

Concerning the placement of defects with respect to domains and ensuing domain configuration, three basic mechanisms are discussed for acceptor doped "bulk" ferroelectrics. (i) *volume*

*effect*: owing to the polarization $P_D$ associated with the defect dipole $(Fe'_{Zr,Ti} - V_O^{\bullet\bullet})^{\bullet 2}$, an orientation of spontaneous polarization of the surrounding lattice $P_S$ parallel to $P_D$ is energetically favored (90; 91; 84; 83; 92; 93; 94). (ii) *domain-wall effect*: to neutralize internal stresses and charges, defects may migrate to domain walls, stabilizing their position (79; 85). (iii) *grain-boundary effect*: due to the formation of secondary phases at high dopant concentrations (95), surface charges at the grain boundaries are generated that stabilize a certain domain configuration (72). Mechanisms (i, ii) are directly related to an interaction between defect structure and domain walls. It has been proposed that the clamping of domain walls is due to resorting forces that limit the domain-wall displacements (96; 97; 74; 81; 77). On the other hand, the defect dipoles were shown to follow the change of polarization direction after application of an external field, provided the corresponding thermal and electric energies are high enough (84; 83; 92). However, during fast field cycling, the defect-dipole orientation remains unperturbed leading to reversible change of macroscopic polarization with electric field.

The origin of the fine domain structure in $Fe^{3+}$-doped PZT has been discussed in terms of oxygen vacancies disrupting the oxygen octahedral network and thus the spontaneous polarization (will be discussed in Chapter 3). Defect dipoles could thus be located preferentially at domain walls imprinting a nanodomain structure to the material (93; 40; 75). It is, therefore, of a main interest to characterize the location of $(Fe'_{Zr,Ti} - V_O^{\bullet\bullet})^{\bullet}$ defect dipoles either within a domain or at a domain wall. In order to define this location electron paramagnetic resonance (EPR) has been applied (98). In particular, the corresponding local symmetry at the $Fe^{3+}$-site is monitored by means of the second-rank fine-structure interaction[3].

The X-band (9.7 GHz) EPR spectra of PZT(52/48)Fe1.0 are depicted in Fig 2.9 (center). Analogously to the recently reported EPR analysis of $Fe^{3+}$-doped hard and $(La^{3+}, Fe^{3+})$-codoped soft PZT (99; 100; 101; 102), the observed X-band spectra are representative for the so-termed *low frequency* regime $(3B_q^2 \gg h_{mw})$ with two main resonances at low fields. First, they are characteristic for the formation of $(Fe'_{Zr,Ti} - V_O^{\bullet\bullet})^{\bullet}$ defect dipoles. Second, the resonance at 110 mT is representative for a center of axial site symmetry (Fig 2.9(b), top), while the resonance at 160 mT is due to a center of rhombic site symmetry [Fig 2.9(b, bottom)].
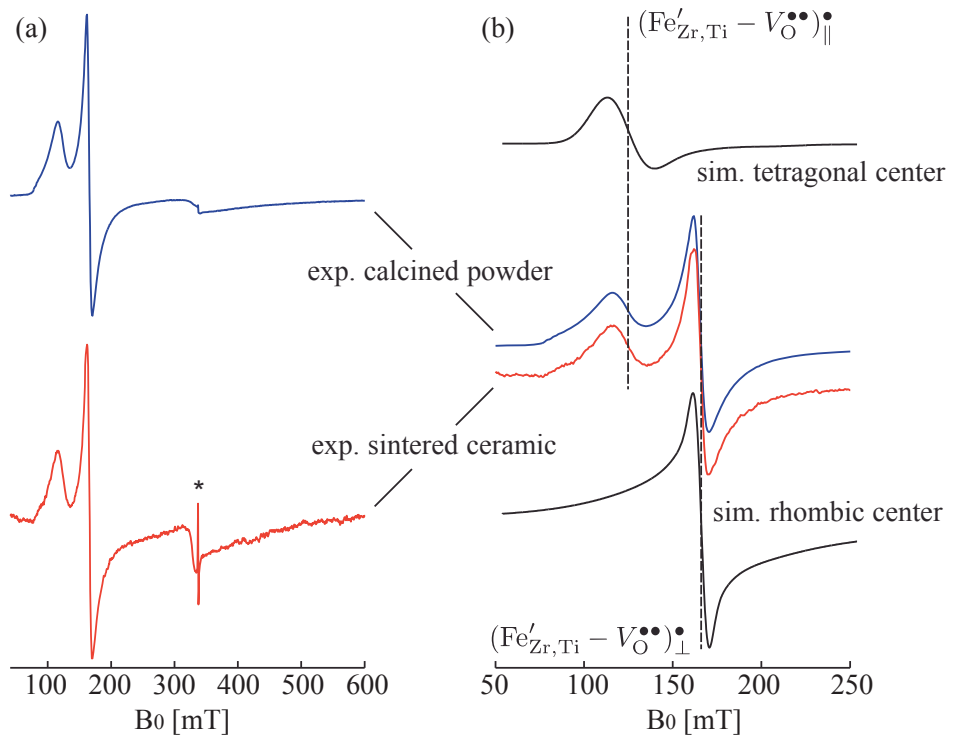
In order to distinguish if (part of the) $(Fe'_{Zr,Ti} - V_O^{\bullet\bullet})^{\bullet}$ defect complexes are located at domain walls, two different samples were investigated. A powder of $Fe^{3+}$-doped PZT 52/48, as representative for a mechanically stress-free system with considerably reduced amount of non-180° domain walls, is compared with a sintered dense ceramic of identical composition

---

[2]In this thesis, the *Kröger-Vink* notation is used to describe the defects. The main body of the notation identifies whether the defect is a vacancy "*V*", or an ion such as "Fe". The subscript denotes the site that the defect occupies. The superscipt identifies the effective charge of the defect relative to the perfect crystal lattice. For this part of notation, dots ($\bullet$) represent positive effective charges, dashes ($'$) represent negative charge (89).

[3]The EPR analysis of PZT(52/48)Fe1.0 was provided by P. Jakes, E. Erdem and R. A. Eichel from Institut für Physikalische Chemie I, Universität Freiburg, Germany. The details of the experiments and calculations of the EPR could be found in the publication: P. Jakes, E. Erdem, R.-A. Eichel, L. Jin, and D. Damjanovic, "Position of defects with respect to domain walls in $Fe^{3+}$-doped $Pb[Zr_{0.52}Ti_{0.48}]O_3$ piezoelectric ceramics," *Applied Physics Letters*, vol. 98, art. no. 072907, 2011.

but owing to the release of internal stress with markedly developed domain structure. Corresponding 1 at.?% $Fe^{3+}$-doped PZT 52/48 ceramics were synthesized by a conventional solid state process using standard mixed oxide route (3). Samples were sintered at 1200 °C for 2 h. The powder used in this experiment was obtained by crashing one of the sintered samples and milling the powder in a planetary mill. The particle size after the milling was verified by a scanning electron microscope. Most particles appeared as individual grains with an average size of around 1-2 µm, which is comparable to the grain size in the sintered samples. The ceramic specimen is characterized by a fine domain structure (see Chapter 3). In order to rule out any effect of poling, both samples were annealed above $T_C$ previous to the EPR experiments (600 °C for 1 h). In case some of the defect dipoles would be located at a domain wall, the resonances indicative for axial and rhombic site symmetry should show a variation in relative intensity for the ceramic as compared to the powder.



**Figure 2.9:** X-band (9.8 GHz) EPR spectra of PZT(52/48)Fe1.0 recorded at 20 K. (a) Experimental spectra for calcined powder (top) and sintered ceramic (bottom); (b) Detailed view of the relevant resonances compared to numerical spectrum simulations for the pure axial (top) and rhombic (bottom) $(Fe'_{Zr,Ti} - V_O^{\bullet\bullet})^\bullet$ site symmetries. An F-center in the ceramic compound is indicated by an asterisk.

The striking observation is that both ceramic and powder spectra display an identical intensity ratio of resonances from axial and rhombic $(Fe'_{Zr,Ti} - V_O^{\bullet\bullet})^\bullet$ centers. Correspondingly, the amount of $(Fe'_{Zr,Ti} - V_O^{\bullet\bullet})^\bullet$ defect dipoles located at a domain wall has to be below the detection limit for EPR. Accordingly, the amount of defects at domain walls should be at least by nine orders of magnitude smaller than the amount located within domains.

The conclusion may be drawn that in an unpoled ceramic the defect dipoles rather not lo-

cate at domain walls. This situation has already been proposed earlier (72; 90) and has been supported by a recent *in situ* optical microscopy study that reported domain-pattern conservation after polarization switching with cyclic electric field (77). While giving strong evidence that defect dipoles are concentrated within domains (between domain walls), the present study leaves open the question whether defects are preferentially distributed close to the grain boundaries or uniformly through the grains. Placement of defects near grain boundaries would be consistent with recent theoretical models that report three orders of magnitude stronger clamping pressure on domain walls from charged defects at the grain boundary than from the defect dipoles between domain walls aligned with polarization (103).

### 2.5.2 Defect structures in soft PZT
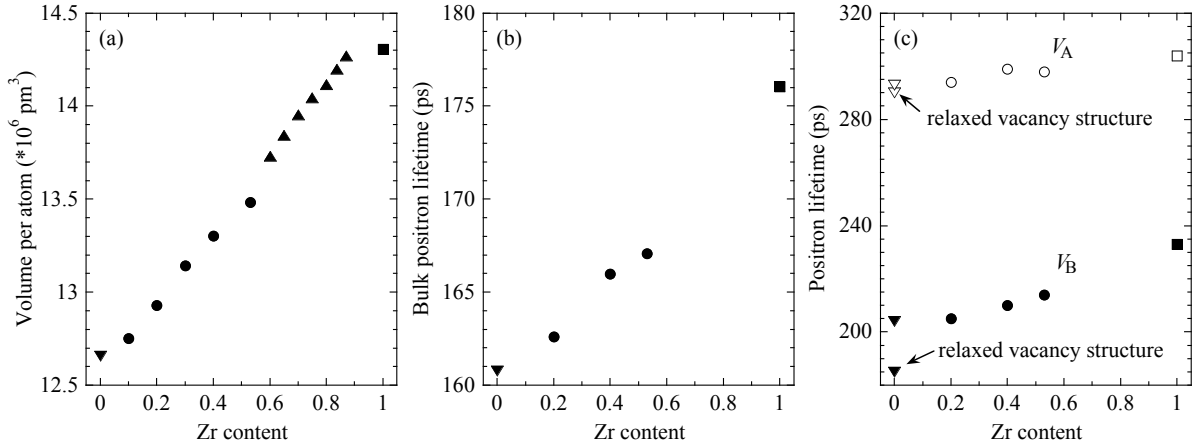
The characteristic feature of soft ferroelectrics is the higher domain wall mobility, compared to undoped materials. Aging, if it occurs, will progress very rapidly hence there appears to be an absence of aging in soft ferroelectrics (4). It has been proposed that (i) the higher domain wall mobility results from donor dopants compensating effects of residual acceptor impurities (2). (ii) The formation of lead vacancies which compensate the donor dopants (e.g. $(Nb^{\bullet}_{Zr,Ti} - V''_{Pb})'$) and so help to reduce internal stresses in the ceramics making domain walls more mobile (2; 68). (iii) Electron transfer between defects which minimize space charge at domain walls (104). Dielectric measurements on $Nb^{5+}$ doped PZT over a wide frequency range show charge mobility is limited below $T_C$ and there is no evidence for alignment of $(Nb^{\bullet}_{Zr,Ti} - V''_{Pb})'$ defect dipoles with the polarization, or for hopping of charged defects, e.g. $V''_{Pb}$ (4). There is some evidence for the simple role of charge compensation of residual acceptor impurities, however, the question of whether donor doping provides additional mechanisms for softening remains unresolved (104).

Substituting $Nb^{5+}$ at the B-site $(Zr^{4+},Ti^{4+})$ in PZT clearly results in donor doping, however, the detail of compensation mechanisms can vary dependent on processing conditions and dopant concentration, and has not been firmly established. It is possible that when Nb doping a perovskite oxide the excess oxygen contained in the donor oxide is lost and compensation is by electrons. An alternative, assumed to be particularly relevant at higher concentrations, is compensation by cation vacancy formation (105; 106). Niobium doping is also expected to suppress oxygen vacancy concentrations. In PZT there is the possibility of PbO loss and the presence of Pb vacancies, which can also alter the Nb compensation mechanism. (106; 107) An attempt has been made to influence the cation vacancy content by varying the Pb content, but the resulting vacancy distributions could not be determined (108). In this section, positron annihilation lifetime spectroscopy (PALS)[4] will be used to study the variation in vacancy de-

---

[4]The PALS analysis of soft PZT ceramic samples was provided by R. A. Singh and D. J. Keeble from Carnegie Laboratory of Physics, School of Engineering, Physics, and Mathematics, University of Dundee, United Kingdom. The details of the experiments of EPR and positron lifetime calculations using density functional theory (DFT) method implemented in the MIKA-doppler package could be found in the manuscript: R. A. Mackie, L. Jin, D. Damjanovic, and D. J. Keeble, "Vacancy defects in Nb doped $Pb(Zr_xTi_{1-x})O_3$ ceramics," to be submitted.

fect content resulting from $Nb^{5+}$-doped PZT ceramics, since its particular sensitivity to cation vacancy defects in perovskite oxide materials.
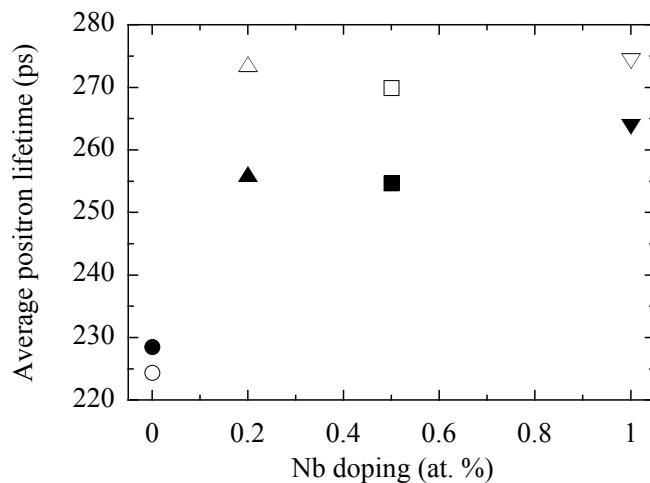


**Figure 2.10:** (a) Variation in unit cell volume per atom for PZT as a function of Zr content; (b) MIKA-doppler calculated bulk positron lifetime with Zr content; (c) MIKA-doppler calculated unrelaxed A-site (open symbols) and B-site (closed symbols) vacancy positron lifetimes, relaxed vacancy structure lifetimes are shown for $x$=0. The crystal structures used for the calculations were obtained from Ref. (109) (down triangle), Ref. (110) (circle), Ref. (111) (up triangle) and Ref. (112) (square).

**Table 2.2:** MIKA-doppler calculated positron lifetime values for $Pb(Zr_xTi_{1-x})O_3$ with $x$=0.40, 0.53 and 1.00.
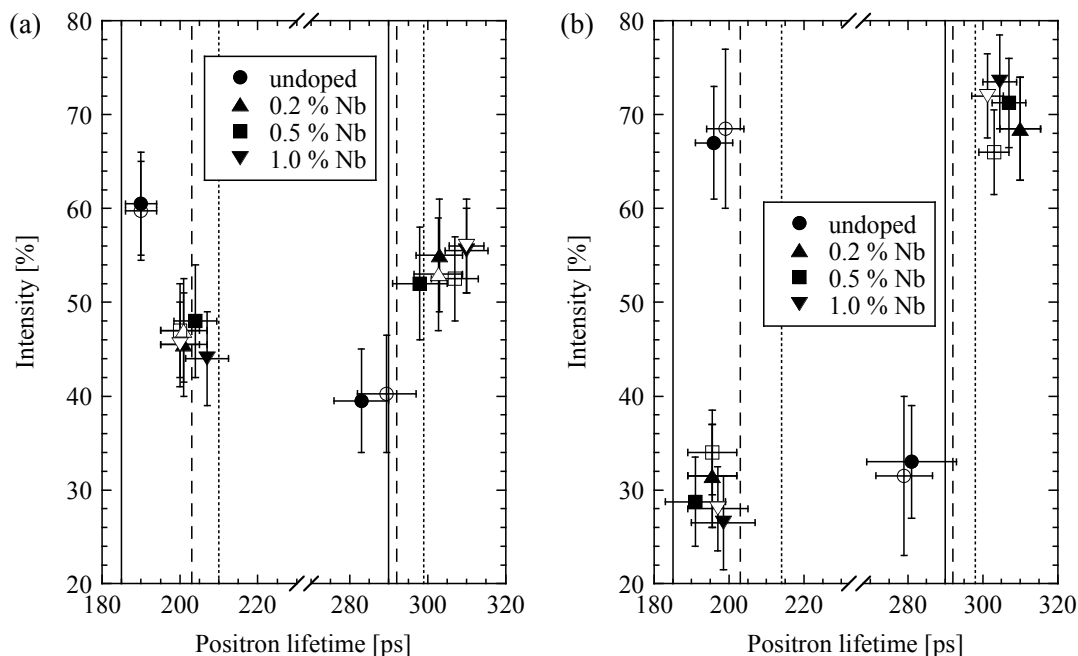
| Zr content | Bulk | $V_A$ | $V_B$ |
|---|---|---|---|
| 0.40 | 166 | 299 | 210 |
| 0.53 | 167 | 298 | 214 |
| 1.00 | 176 | 304 | 233 |

The DFT calculated positron lifetime values for unrelaxed vacancy defects in $Pb(Zr_{0.40}Ti_{0.60})O_3$ and $PbZrO_3$ were calculated and are given in Table 2.2. The variation in bulk and cation vacancy lifetime values with Zr content is shown in Fig. 2.10, along with the variation in the structural unit cell volume per atom (structures for $x$=0.6 to 0.9 were obtained from Corker *et al* (113)). The bulk lifetime and unit cell volume per atom increase approximately linearly with increasing Zr content; the bulk lifetime increases from 161 ps for $PbTiO_3$ to 176 ps for $PbZrO_3$. The calculated unrelaxed B-site vacancy value shows a similar trend, increasing from 203 ps to 233 ps. However, the unrelaxed A-site vacancy value remains relatively constant, varying from 299 ps to 304 ps over the range of Zr contents. Local structural relaxations have been calculated for the Ti and Pb vacancies in $PbTiO_3$ (114), these result in a marked reduction in the $V_B$ lifetime from 203 ps to 185 ps but have a negligible effect on the $V_{Pb}$ value (115).

The average positron lifetimes as a function of Nb-doping for both the tetragonal and rhombohedral PZT compositions are shown in Fig. 2.11. The values were all significantly greater

**Figure 2.11:** Average positron lifetime as a function of Nb doping for $x=0.58$ tetragonal (solid symbols) and $x=0.42$ rhombohedral (open symbols) $Pb(Zr_{1-x}Ti_x)O_3$ ceramic samples.



**Figure 2.12:** Positron lifetime components as a function of $Nb^{5+}$ doping concentration for tetragonal (Zr/Ti=42/58) (a) and rhombohedral (Zr/Ti=58/42) (b) PZT ceramics samples. Measurements using Kapton foil (solid symbols) and Ni foil (open symbols) supported positron sources are shown. The MIKA-doppler calculated positron lifetimes for relaxed $V_{Ti}$ (185 ps) and $V_{Pb}$ (290 ps), and unrelaxed $V_{Ti}$ (203 ps) and $V_{Pb}$ (292 ps) in $PbTiO_3$ are shown as solid and dash lines, respectively. The unrelaxed $V_B$ (210 ps) and $V_{Pb}$ (299 ps) for $Pb(Zr_{0.40}Ti_{0.60})O_3$ are shown as dot lines in Fig 2.12(a). The unrelaxed $V_B$ (214 ps) and $V_{Pb}$ (298 ps) for $Pb(Zr_{0.53}Ti_{0.47})O_3$ are shown as dot lines in Fig 2.12(b).

than the bulk lifetime (Table 2.2, Fig. 2.10) indicating the presence of vacancy defects in all the samples, undoped and doped. Both compositions exhibited a marked increase in the average positron lifetime on incorporation of 0.2 at. % Nb, this increase was greatest for the rhombohedral samples. The average lifetime values for the Nb doped samples were significantly greater than the lifetimes for B-site vacancy defects (Table 2.2, Fig. 2.10), this requires the presence of larger vacancy defects, for example A-site vacancies or complexes involving cation vacancy defects.

To gain further insight it is necessary to analyze the contributing lifetime components resulting from the multi-exponential fitting. All the PALS spectra gave best fits (chi-squared<1.2) for two positron lifetime components (Fig. 2.12). The lifetime components values were found to be greater than the bulk positron lifetime in all the samples. This observation is consistent with the large values measured for the average lifetimes and shows that the concentration of positron trapping vacancy defects was sufficiently high to cause saturation positron trapping, where essentially every implanted positron annihilates from a vacancy defect. The standard positron trapping model predicts that the component lifetime values obtained under saturation trapping are normally characteristic of the type of vacancy defects present. Further, while sensitivity to absolute vacancy concentrations is lost, in the case of saturation trapping to two types of vacancy defect the ratio of the component intensities does provide a measure of the ratio of vacancy concentration. It should also be noted that the ability of PALS to separate two physical lifetime components is restricted by the finite spectrometer timing resolution function width, if two components are not resolved then simulations confirm that a combined weighted average component results. (112).

As discussed above the existence of saturation positron trapping precludes the calculation of absolute vacancy defect concentration from the PALS spectra. In consequence, the marked increase in average lifetime values shown in Fig. 2.11 with the incorporation of Nb cannot be directly assigned to an increase in vacancy defect concentrations with Nb doping. However, the behavior of trapping to the two components shown in Fig. 2.12 clearly demonstrate that positron annihilation in the undoped samples is dominated by B-site vacancy related defects, while on the introduction of Nb trapping to A-site vacancy defects dominates over B-site vacancy trapping. Niobium doping causes an increase in the ratio $[V_A]/[V_B]$ compared with the undoped samples. Clearly this can be achieved in a number of ways, (I) an increase in $[V_A]$, (II) a suppression of $[V_B]$, (III) a combination of both. This increase in $[V_A]/[V_B]$ occurs with 0.2 at. % doping, further increasing the Nb concentration may systematically increase $[V_A]$, however, the only conclusion that can be drawn from the PALS results is that if this does occur $[V_B]$ must also then increase to maintain an approximately constant $[V_A]/[V_B]$ ratio consistent with the behavior shown in Fig 2.11 and Fig 2.12. Earlier PALS measurements on Nb doped rhombohedral (60/40) PZT report a second lifetime component of 290 – 310 ps with an approximately constant intensity of 80 – 90 % for Nb concentrations of 0.5 – 4 mol %. (116) PALS measurements of Nb doped $SrTiO_3$ have also clearly identified the presence of $V_{Sr}$ defects, and an absence of Ti vacancies. (112) The results presented here provide clear evidence

that cation vacancy compensation of $Nb_B^{5+}$ occurs dominantly by the vacancy formation at the A-site, however, they do not preclude the existence of parallel compensation mechanisms that do not involve cation vacancy formation.

The two positron lifetime component values measured to be $190-210$ ps and $285-310$ ps in the PZT samples studied were found to be in agreement with previous studies and with DFT calculated values for the two cation vacancy defects, and B-site and A-site vacancies. The defect assignments were further supported by the results of variable energy positron lifetime measurements that observed in increase in trapping to $V_B$ defects on cooling, consistent with the larger negative local charge. Positron trapping was observed to be dominated by cation vacancy defects present at concentration greater than approximately 50 ppm in all the undoped and $Nb^{5+}$-doped PZT ceramics samples. Incorporation of Nb resulted in a reversal of the intensity ratio for the two lifetime components, positron trapping to $V_B$ related defects with respect to $V_B$ defects dominated in the undoped samples but trapping to $V_B$ defects dominated for the 0.2 at. %, higher, Nb doped samples. It is concluded that one of the charge compensation mechanisms resulting from Nb dopant incorporation involves the formation of Pb vacancy defects, and/or the suppression of B-site vacancy defects.

## 2.6   Summary

Ferroelectric PZT ceramic samples within rhombohedral, MPB and tetragonal regions were chosen to study the soft and hard mechanism. High quality samples without apparent second phase were synthesized by mixed oxide route. By controlling the Zr/Ti ratio as (58/42), (42/58), and (52/48), three groups of PZT ceramics with expected phase structures are obtained, as identified by the XRD analysis. Characterizations of the temperature dependence of the dielectric properties and ferroelectric hysteresis loops prove expected soft and hard features. The dielectric properties also support that the dopants are incorporated into the crystal structure rather than segregated at grain boundary or as a second phase. Those samples will be used in the following works to clarify the soft and hard meachnisms.

# Chapter 3

# Domain structure

The dielectric and piezoelectric properties of ferroelectric ceramics are strongly correlated with the domain and defect structures. Before interpreting the results of the broadband dielectric and piezoelectric properties of the soft and hard PZT ceramics, several important questions must be addressed concerning the domain and defect structures[1]

- The high dielectric and piezoelectric properties of PZT at MPB are attributed to the fine domain structure. Is this fine domain structure a sufficient condition to explain high properties at MPB?

- Is the parabolic relationship between the average grain size and domain size, which has been observed in undoped and soft PZT, also valid in hard PZT ceramics?

## 3.1 Introduction

The domain structure of PZT ceramics either in rhombohedral, tetragonal or MBP region have been intensively investigated by different groups (117; 118; 119; 120; 121), since the first study of domains was reported by Gerson in 1960 (68). Recently, a systematic study of the domain structure as a function of the Zr/Ti ratio in undoped PZT ceramics was conducted by Schmitt *et al* (41). According to those studies, it is accepted that the domain structures are highly influenced by the crystalline symmetry. For PZT ceramics in rhombohedral phase, irregular $71°$ or $109°$ domain walls with wavy character are typical, whereas in tetragonal phase, straight $90°$ domain walls with different domain width are frequently observed. Approaching the MPB region from either rhombohedral or tetragonal region, the domain size (or domain width) shows a drastic decrease. Compared with the domain structures of undoped and soft

---

[1]The data presented in this chapter are partially published or to be published through following publication and manuscript: (1) L. Jin, Z. B. He, and D. Damjanovic, "Nanodomains in $Fe^{+3}$-doped lead zirconate titanate ceramics at the morphotropic phase boundary do not correlate with high properties," *Applied Physics Letters*, vol. 95, art. no. 012905, 2009; (2) L. Jin, Z. B. He, and D. Damjanovic, "Domain configurations and parabolic relationship between the domain size and grain size in B-site $Fe^{3+}$-doped Pb(Zr,Ti)$O_3$ ceramics," to be submitted.

PZT ceramics, there have been little publications on the hard PZT ceramics, except the works by Tan *et al* (122; 75).

The domain structure of PZT ceramics at MPB received much attention due to the high dielectric and piezoelectric properties, although the origins of the high properties are still being debated. A recent interpretation is based on the discovery of a third, monoclinic phase at the MPB by Noheda *et al* (33) using high-resolution synchrotron XRD. The high properties were associated to polarization rotation, which is assumed to be facilitated within the monoclinic phase. (35) Observation of the monoclinic phase in XRD experiments has, however, been questioned. As argued by Jin *et al* (38; 39), coherently scattering tetragonal nano-size domains would be indexed as a monoclinic phase in XRD patterns. A similar conclusion has been reached more recently in other studies (41). In addition to the monoclinic phase−nanodomain controversy, it has been proposed that nanodomains at MPB in PZT (40; 41; 42) and in other ferroelectrics (38; 123; 124; 125) are related to the high properties. It has been argued, for example, that the energy of nanodomain walls is inherently low, leading to their easy displacement and consequently to a large contribution to the electromechanical properties (38; 39). The expression "*nandomains*" here loosely refers to the structure of ferroelectric domain walls where separation of adjacent domain walls is on the order of tens of nanometers rather than hundreds of nanometers or more.

Understanding of the relationship among MPB, nanodomains and enhanced properties in PZT is complicated by the fact that small domains (tens to hundreds of nm) have been reported in undoped PZT at MPB (41; 42; 126) and in heavily modified compositions at (127; 118) and far (75) from MPB. It is thus difficult to infer from the available data what is the effect of MPB on the domain size and how the domain size influences the properties. It is of a particular importance to verify whether nanodomains can be correlated with the high properties in doped PZT. Besides the reduction of the domain size due to the MPB, the grain size effect on the domain size should also be taken into account. Theoretical calculations predict a parabolic relation between the grain size and domain size (128; 129),

$$d \propto (g)^m, \tag{3.1}$$

where $d$ is domain size, $g$ is grain size, and the coefficient $m$ is close to 1/2. This predication has been proven in BaTiO$_3$ (12; 65) and PZT (119; 130) ferroelectric ceramics, when the mean grain size is in the range between 1 to 10 µm. In addition, finer domain size, i.e. higher domain density is observed for the submicron grains, compared with the domain size predicted by the parabolic relation. The validity of this parabolic relation has been verified in undoped and soft PZT, however, whether it is applicable to the hard PZT is still not clear.

In an attempt to answer the above questions, a transmission electron microscopy (TEM) study of domain walls structure of undoped and doped PZT with an MPB composition was performed at first. In order to avoid the decreasing effect induced by the composition at MPB, the grain size-domain size relationship in hard PZT were checked with the compositions far away from MPB. Those examinations would deepen our understanding of the domain configu-

rations and dimensions in PZT system.
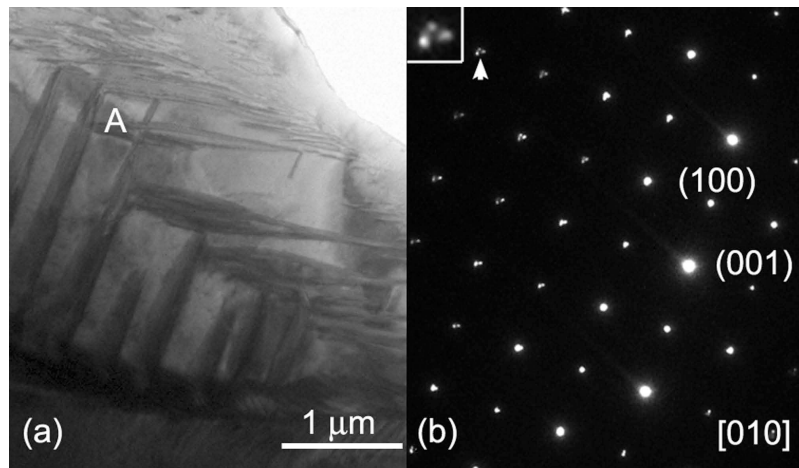
## 3.2 Experimental descriptions

The samples for TEM observation were prepared from sintered ceramic disks. Ceramics were first polished down to thickness of $100\,\mu m$, and then ultrasonically cut to small samples with a diameter of 3 mm. After that, they were polished mechanically again to a thickness of about $30\,\mu m$, followed by $Ar^+$ ion beam thinning at 4 kV using a $4°$ incidence angle till a small hole is formed in the center. Finally a lower voltage of 3 kV was used to thin samples further. Before observation by TEM, all specimens were kept at ambient temperature for more than one day to relax the strains probably caused by ion milling. TEM experiments were performed using a FEI CM20 microscope equipped with a double tilt holder and operated at 200 kV.
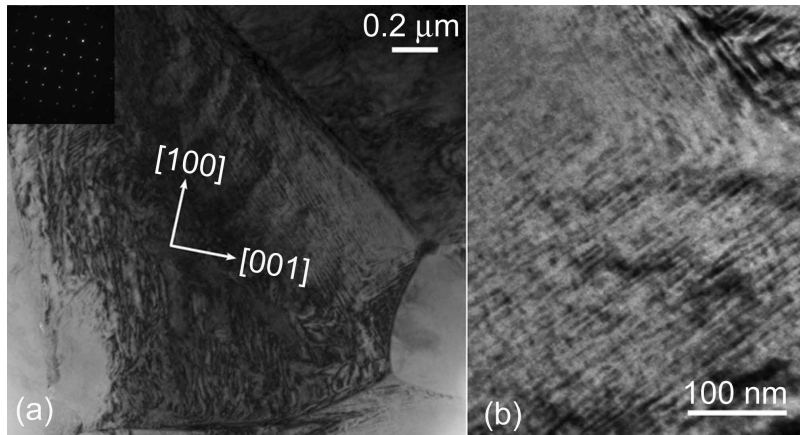
## 3.3 Domain structure

### 3.3.1 Morphotropic phase boundary



**Figure 3.1:** (a) Room temperature bright field TEM image of PZT(52/48) taken near [010] direction; (b) Corresponding electronic diffraction pattern from "A" area in (a). Inset in Fig 3.1(b) displays the point splitting along two mutually perpendicular directions indicating tetragonal symmetry.

Representative domain walls structure of an undoped sample PZT(52/48) is illustrated in Fig 3.1(a). We refer to the separation between adjacent domain walls as "domain size" or "domain width". In contrast to the domain morphology of the same composition reported in Ref. (41), our undoped samples exhibit coarser domains. The observed area is mostly composed of domains with the width in the range from 0.1 to $1\,\mu m$. Some irregular domains with finer domain walls structure are visible in the upper part of the picture. The electronic diffraction pattern in Fig 3.1(b) reveals a strong splitting along pseudocubic [100] and [001] directions,
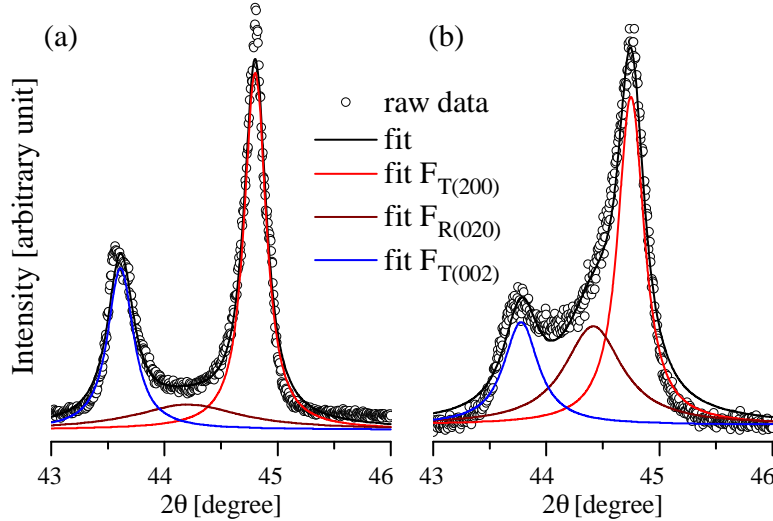
**Figure 3.2:** Room temperature bright field TEM images of high density two dimensional nanodomains in PZT(52/48)Fe1.0 at large (a) and small (b) scale.

which suggests a high lattice distortion along *a* and *c* axes. The XRD spectrum (see below) confirms the tetragonal structure.

Typical nanodomains are observed in $Fe^{3+}$-doped samples PZT(52/48)Fe1.0, as shown in Fig 3.2. The widths of nanodomains are on the order of 10 nm. These nanodomains do not possess definite crystallographic relationship with respect to each other (Fig 3.2). This is qualitatively different from small domains reported by Tan *et al* (122) in $K^+$-doped PZT with composition deep in the rhombohedral region, where the domain size was on the order of tens of nm and domain walls had a definite crystallographic orientation. Clearly, MPB has a strong influence on the domain structure of both doped and undoped samples. The extent of the splitting of the electron diffraction spots, shown in the inset of Fig 3.2(a), is weaker than in undoped ceramics [Fig 3.1(b)], indicating a smaller lattice distortion.

In undoped and donor doped PZT ceramics, the grain size and domain size were reported to be roughly related by the parabolic relation (Eq. 3.1), when the grain size ranges from 1 to 10 μm (119). The grain size of PZT(52/48) and PZT(52/48)Fe1.0 are 7.92 and 2.05 μm, respectively. According to the parabolic scaling, the domain size of PZT(52/48)Fe1.0 should be around one half of that in the undoped ceramics. However, based on the TEM data, the domain size of PZT(52/48)Fe1.0 is smaller by a factor of 10 to 100 than that in PZT(52/48). This clearly indicates that the decrease of the domain size in the $Fe^{3+}$-doped material is not only affected by the grain size and grain boundary conditions, but also by the presence of the acceptor defects.

We next examine the effect of the domain size on the properties of the ceramics. An attempt to make a correlation between the bulk properties and the domain walls structure observed by TEM is a delicate process (50). Poling, thinning and thinness of the sample as well as the very observation with TEM may change the domain wall structure. To get as varied conditions as possible, we compare piezoelectric properties of poled and dielectric permittivities of unpoled doped and undoped samples. The relative dielectric permittivities of unpoled PZT(52/48) and PZT(52/48)Fe1.0 ceramics are 1080 and 870, respectively. The piezoelectric coefficients of the

**Figure 3.3:** XRD patterns of PZT(52/48) (a) and PZT(52/48Fe)1.0 (b) at {200} reflections. $F_{T(002)}$ and $F_{T(200)}$ represent the peaks with tetragonal while $F_{R(020)}$ represents the peak with rhombohedral symmetry.
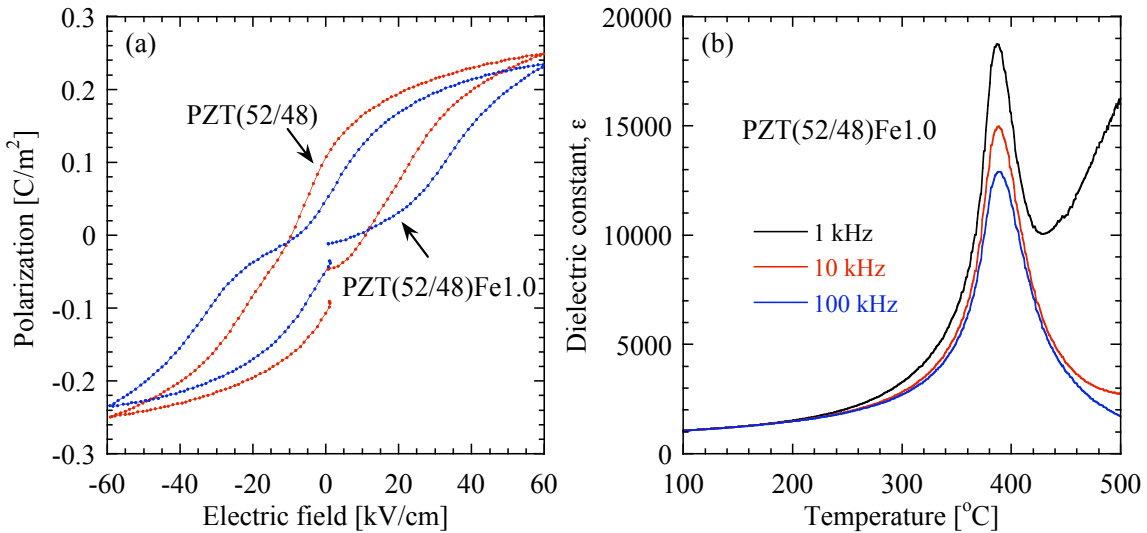
undoped and doped samples are 200 and 160 pC/N. These properties are thus decreased in the doped material by about 20%, even though the domain walls structure has become much finer.

The MPB region may contain mixture of phases and properties may depend on the crystal phase content. To verify whether the phase mixture could be responsible for the properties difference, we have examined samples with XRD. These results suggest a coexistence of tetragonal ($T$) and rhombohedral ($R$) phases in both doped and undoped samples, Fig 3.3. Quantitative evaluation of the phase content was made using the {200} XRD reflections. The tetragonal volume fraction $\chi_T$ was estimated using the relation

$$\chi_T = \frac{I_{T(200)} + I_{T(002)}}{I_{T(200)} + I_{R(020)} + I_{T(002)}}, \tag{3.2}$$

where $I_T$ and $I_R$ are the corresponding tetragonal and rhombohedral peaks intensities (131). Fig 3.3 shows the fitting results based on the Lorentzian profiles. In PZT(52/48), $\chi_T \approx 95\%$ and is decreased to $\approx 82\%$ in PZT(52/48)Fe1.0. Introduction of $Fe^{3+}$ into PZT(52/48) increases the amount of the rhombohedral phase and decreases the lattice distortion. Both lattice and domain wall contributions to the dielectric permittivity are known to be higher in PZT on the rhombohedral side of the MPB (132). Therefore, a lower $\chi_T$ in $Fe^{3+}$-doped samples would be expected to correspond to higher electro-mechanical properties than in undoped samples, while the opposite is observed.

Thus, despite the presence of nanodomains and a higher concentration of rhombohedral phase, $Fe^{3+}$-doped ceramics exhibit lower properties than undoped samples. This suggests that the hardening effect of acceptor dopant is stronger than properties enhancement related to a finer domain walls structure. That doped samples are indeed hardened by $Fe^{3+}$ doping is seen from the polarization-electric field hystereses loops shown in Fig 3.4(a). Strong loop pinching is observed in $Fe^{3+}$-doped sample, while only slight pinching is seen in undoped samples. The

**Figure 3.4:** (a) Polarization-electric field loops for PZT(52/48) and PZT(52/48)Fe1.0 at room temperature; (b) Dielectric constant vs. temperature curve for PZT(52/48)Fe1.0. Measurement was performed at 1, 10, and 100 kHz upon heating.
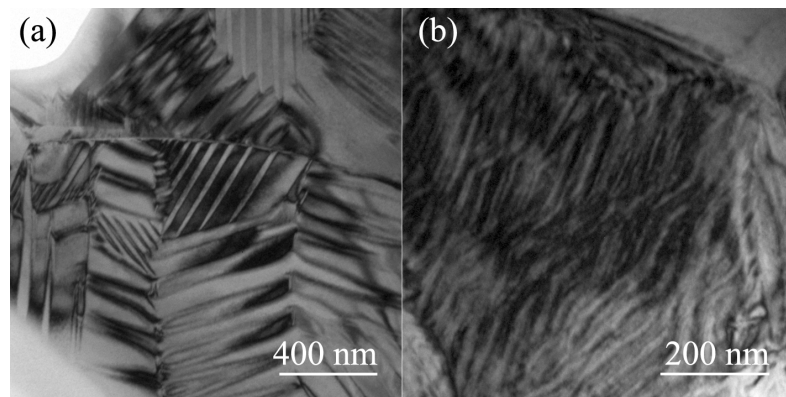
loop pinching in $Fe^{3+}$-doped PZT is due to $(Fe'_{Zr,Ti} - V_O^{\bullet\bullet})^{\bullet}$ defect dipoles (72; 98), which create a restoring force for domain walls and limit their displacements (74; 77), thus reducing their contribution to the properties. The slight loop pinching observed in undoped might originate from naturally present acceptor impurities in the starting powders or $(V_O^{\bullet\bullet} - V_{Pb}'')$ dipoles; it is known that undoped PZT exhibits a p-type conductivity (2).

Note that nanodomains showed in Fig 3.2 do not seem to be *polar nanoregions* (PNR) as reported in $(Pb,La)(Zr,Ti)O_3$ (122) and recently in PZT (133), although their dimensions are comparable. Ferroelectrics with PNR usually exhibit a dielectric relaxor behaviour. (134) This is not the case in PZT(52/48)Fe1.0 where close inspection of the temperature and frequency dependent dielectric response does not reveal any relaxor characteristics (Fig 3.4(b)).
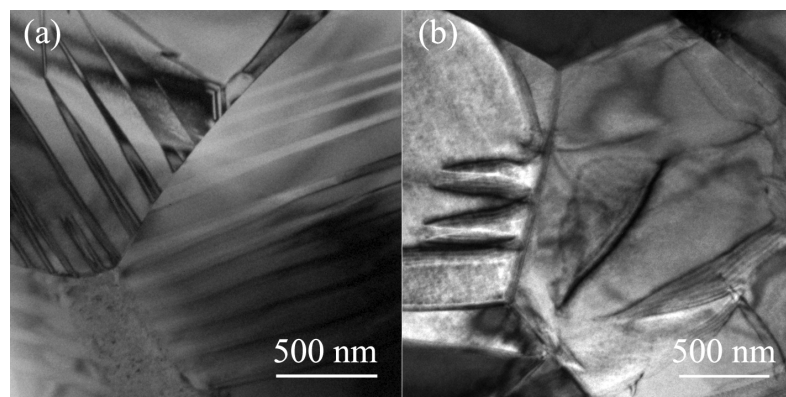
Finally, it is tempting to speculate about the origin of the fine domain wall structure in $Fe^{3+}$-doped PZT. With 1 at.% concentration, one $Fe^{3+}$ cation and associated oxygen vacancy would be placed in average in a cube of $5{\times}5{\times}5$ unit cells, which is every 2 nm and less than the size of the observed nanodomains (10 nm) (2). Oxygen vacancies are expected to disrupt the continuity of the oxygen octahedral network and spontaneous polarization. The homogeneous regions of polarization which define ferroelectric domains should be of the same scale as the regions undisturbed by the defects. This may suggest that the oxygen vacancies are concentrated within the walls region, which would be consistent with *ab initio* predictions (93) but inconsistent with the bulk model of defect dipoles in perovskite ferroelectrics (135). This conjecture thus potentially raises an important question of the placement of defect dipoles in hard ferroelectrics. It is possible that $V_O^{\bullet\bullet}$ are not homogeneously distributed.

### 3.3.2 Tetragonal vs. rhombohedral region

Fig 3.5 shows representative room temperature domain configurations of PZT(42/58)Fe1.0 and PZT(58/42)Fe1.0 ceramics observed by TEM in bright field mode. In PZT(42/58)Fe1.0 within a grain, domains are divided into several groups. In every group, broad and narrow lamellar domains appear and distribute along the same direction. This lamellar configuration is similar to the configuration reported in undoped tetragonal PZT ceramics (41; 126), but the domain size is much smaller. The width of those domains changes between 20 to 60 nm. Taking into account volume variation, an average domain size of 42 nm was obtained. In PZT(58/42)Fe1.0, in each grain highly zigzag domain walls are revealed in Fig 3.5(b). In a relatively small region those zigzag domain walls are parallel to each other. This configuration is totally different from the configurations in undoped PZT with the close Zr/Ti ratio (121; 136). Because of the small-scale periodic arrangement of the domain walls, we could estimate the domain size based on such a specific configuration. An approximate value of 17 nm is extracted from Fig 3.5(b).



**Figure 3.5:** Room temperature bright field TEM images of (a) PZT(42/58)Fe1.0 and (b) PZT(58/42) Fe1.0 ceramics.
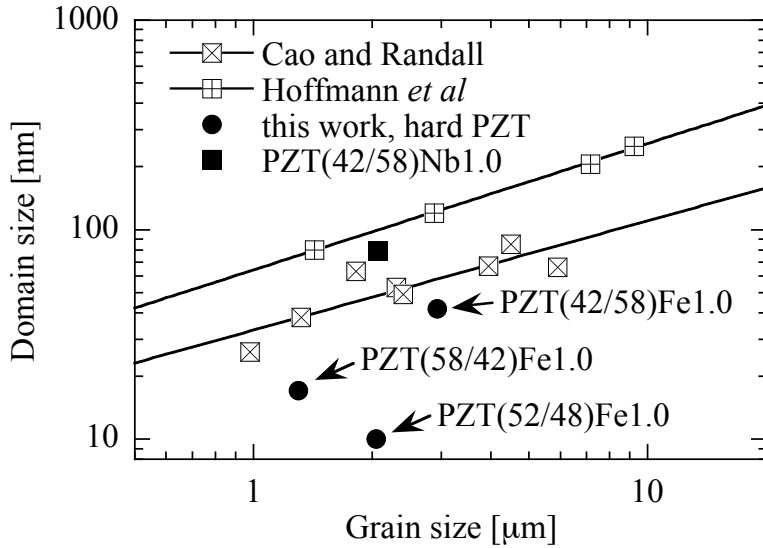


**Figure 3.6:** Room temperature bright field TEM images of (a) PZT(42/58)Nb1.0 and (b) PZT(58/42) Nb1.0 ceramics.

Bright field TEM images in Fig 3.6 show the domain configurations of PZT(42/58)Nb1.0 and PZT(58/42)Nb1.0. Compared with PZT(42/58)Fe1.0, in PZT(42/58)Nb1.0 lamellar do-

mains often distribute along an exclusive direction within each grain. The domain size becomes larger and approaches the value of that in undoped PZT (41). For PZT(58/42)Nb1.0, the domain walls are very sensitive to the electron beam, and their positions are often shifted by the beam. Shown in Fig 3.6(b), large wedge-shaped domain walls traverse within grains and stop at the grain boundary (118). Because of their irregular shape, no attempt was conducted to determine the domain size for this sample. In general, the domain size in the soft group is relatively larger than in the hard group.

**Table 3.1:** Average grain size $g$, domain size $d$, $\varepsilon'_L$ and $\varepsilon'_H$ of studied PZT samples. $\varepsilon'_L$ and $\varepsilon'_H$ are the dielectric permittivity measured at 1 kHz and 20.2 GHz at room temperature, respectively.

| Composition | $g$ ($\mu$m) | $d$ (nm) | $\varepsilon'_{1\,kHz}$ | $\varepsilon'_{20.2\,GHz}$ |
|---|---|---|---|---|
| PZT(42/58)Fe1.0 | 2.92 | 42 | 450 | 320 |
| PZT(58/42)Fe1.0 | 1.30 | 17 | 575 | 250 |
| PZT(42/58)Nb1.0 | 2.07 | 79 | 575 | 310 |
| PZT(58/42)Nb1.0 | 3.79 | –– | 685 | 235 |



**Figure 3.7:** Logarithmic plot of measured domain size vs. grain size for PZT ceramics. Parabolic fitting (solid lines) gives $m$ as 0.52 and 0.60 corresponding to the data by Cao and Randall (119), and Hoffmann *et al* (130), respectively. PZT(52/48)Fe1.0, which possesses nanodomains (10 nm) with a grain size of 2.05 μm, is also included.

Now, let us discuss the relationship between the grain size and domain size. The histogram for the grain size of each composition shows a symmetric distribution, and a mean value is taken as the grain size. As shown in Table 3.1, the grain size of all studied samples ranges between 1 to 4 μm. The grain size of those samples fulfills the precondition to discuss the parabolic relation between the grain size and domain size. Except PZT(58/42)Nb.10, the mean domain size of samples is also given in Table 3.1. Fig 3.7 shows the logarithmic plot of measured

domain size vs. grain size for PZT ceramics. Since the parabolic relation in PZT system is proven in undoped and soft PZT (119; 130), we also included those data here for comparison. The solid straight lines represent the fitting based on parabolic function. It can be seen that even for the same PZT system, the domain size reported by different groups also shows an obvious variation. Taking into account error and discrepancy in determination of the domain size, here we suppose that all the data, falling into the region confined by the parabolic fitting, satisfy such a parabolic relation. According to this criterion, it is shown that PZT(42/58)Nb1.0 supports this parabolic relation. However, for studied hard PZT samples, including the PZT(52/48)Fe1.0, the data points deviate significantly from the predication by the parabolic relation.

Note that PZT(42/58)Fe1.0 is closer to the theoretical predication than PZT(58/42)Fe1.0. As suggested in undoped PZT (41), the domains become finer when composition approaches the MPB from both tetragonal and rhombohedra phases. It is normally accepted that composition with Zr/Ti ratio of 52/48 corresponds to the MPB (2). It is evident that PZT(58/42)Fe1.0 is closer to the PZT(52/48)Fe1.0, than PZT(42/58)Fe1.0. Thus the domain size of PZT(58/42)Fe1.0 should be larger than the value of PZT(52/48)Fe1.0, but still less than in the PZT(42/58)Fe1.0. Schmitt *et al* (41) have calculated the domain size in samples with tetragonal symmetry utilizing the model of a two-dimensional adjustment, where clamping in the third direction is not present. According to Arlt (12), the domain size is calculated by the following equation,

$$d = \sqrt{\frac{\sigma_{90}g}{2(c_{11}/48)S^2}}, \tag{3.3}$$

where $\sigma_{90}$ is 90° domain wall energy, $c_{11}$ stiffness coefficient and $S = (c/a) - 1$ is the elastic strain. Compare with the domain size determined by TEM (40-230 nm) (41), Eq 3.3 suggests a large domain size of 453 nm. Without reliable values of domain wall energy, such attempts seem to be difficult to justify.

In order to correlate the domain configurations to the dielectric properties, we measured the $\varepsilon'$ of all studied samples at low frequency ($\varepsilon'_L$, at 1 kHz) and high frequency ($\varepsilon'_H$ at 20.2 GHz[2]). It will be shown in Chapter 4 that the $\varepsilon'$ measured at 20.2 GHz approaches the upper limit of the intrinsic value, while the difference of $\varepsilon'$ between $\varepsilon'_L$ and $\varepsilon'_H$ is mainly attributed to extrinsic domain wall contribution. Room temperature $\varepsilon'_L$ and $\varepsilon'_H$ of all studied samples are given in Table 3.1. For the hard and soft samples with the same Zr/Ti ratio, their $\varepsilon'_H$ are very close, which suggests that they possess the same intrinsic contribution as we supposed. The large difference is found at $\varepsilon'_L$, where soft PZT possesses larger value than hard one, although the higher domain wall density is observed in hard PZT. Arlt and Pertsev have shown that large domain wall density leads to lower permittivity (137). Their calculation results are in contradiction with the model for the interpretation of high dielectric permittivity in fine-grained ceramics (138), however, they are consistent with our observations. In hard PZT with both rhombohedral and tetragonal symmetry, the $(Fe'_{Zr,Ti} - V_O^{\bullet\bullet})^{\bullet}$ defect diploes pin the domain wall motion (139; 3). Thus the $\varepsilon'_L$ is a competing result between the high domain density and low

---

[2]The measurement techniques used to determine the microwave frequency dielectric properties will be introduced in Chapter 4.

domain wall mobility. In the case of hard PZT, it seems that instead of domain wall density, domain wall mobility plays a more crucial role.

To sum up, TEM study on hard PZT ceramics reveals fine domain configurations in both tetragonal and rhombohedral phases. The finer domain size of the hard PZT does not give parabolic relationship between grain size and domain size proposed for the PZT system. Dielectric study suggests that domain wall mobility plays a more important role than domain size in contributing to the dielectric response. In other ferroelectric systems with oxygen vacancies, finer domain configurations are expected. Localizing the oxygen vacancy (domain wall vs. bulk) is an important problem.

## 3.4 Summary

The answers to the questions concerning the domain and defect structures proposed above are summarized as follows:

- Our results suggest that the fine domain walls structure cannot by itself explain enhancement of the properties in morphotropic PZT. The mobility of the domain walls should be taken into account to explain the enhanced properties and, as shown above, the high mobility is not strictly correlated with the fine domain walls structure.

- TEM study on hard PZT ceramics reveals fine domain configurations in both tetragonal and rhombohedral phases. In addition, the results show that the parabolic scaling between grain and domain size is broken in $Fe^{3+}$-doped PZT. The finer domain size of the hard PZT cannot be predicted by the parabolic relationship proposed for undoped and soft PZT ceramics. In other ferroelectric systems with oxygen vacancy, finer domain configurations are also expected.

# Chapter 4

# Microwave dielectric response in PZT and other perovskite ferroelectric ceramics

By mean of novel measuring techniques, the upper limit of frequency of the broadband dielectric spectrum discussed in this thesis can be expanded up to $2 \times 10^{10}$ Hz. It is very interesting that a strong dielectric dispersion, which is often observed in the frequency range between $10^8$ and $10^{10}$ Hz (i.e., "microwave dielectric response") in many ferroelectric ceramics and single crystals, falls into the scope of our broadband spectrum. However, both experimental characterization and explanations and theoretical treatments of such a common dielectric dispersion are not well developed. In this chapter, this microwave dielectric dispersion is discussed. The key questions related to this microwave dielectric dispersion are[1]:

- The microwave dielectric dispersion is mainly attributed to the domain wall motion or piezoelectric grain resonance. Which factor plays a more important role in the microwave dielectric response? Which model predicts the dispersion frequency (frequency corresponding to the maximum of loss or imaginary part of permittivity) more accurately?

- Can the microwave dielectric dispersion be used to evaluate the extrinsic domain wall contributions to the permittivity?

---

[1]The data presented in this chapter are partially published or to be published through following publications and manuscript: (1) L. Jin, V. Porokhonskyy, and D. Damjanovic, "Domain wall contributions in Pb(Zr,Ti)O$_3$ ceramics at morphotropic phase boundary: A study of dielectric dispersion," *Applied Physics Letters*, vol. 96, art. no. 242902, 2010; (2) V. Porokhonskyy, L. Jin, and D. Damjanovic, "Separation of piezoelectric grain resonance and domain wall dispersion in Pb(Zr,Ti)O$_3$ ceramics," *Applied Physics Letters*, vol. 94, art. no. 212906, 2009; (3) V. Porokhonskyy, L. Jin, and D. Damjanovic, "Common features in the microwave response of perovskite ferroelectric ceramics," to be submitted.

## 4.1  Introduction

### 4.1.1  Experimental observations

The nature of the microwave dielectric dispersion in ferroelectric ceramics and single crystals has attracted much interest since the late 1940s and early 1950s. As first observed in BaTiO$_3$ (140; 141; 142; 143; 144), this microwave dielectric dispersion, which manifests itself by a rapid decrease in $\varepsilon'$ and a corresponding peak in $\varepsilon''$ (or tan$\delta$) in the frequency range from $10^8$ to $10^{10}$ Hz, has been also indentified in many other ferroelectric ceramics, such as, PZT (145; 146; 147; 148; 149; 150), (Ba,Sr)TiO$_3$ (151), LiNbO$_3$ (152), PbZrO$_3$ (153), PbTiO$_3$ (154), (1-$x$)BiScO$_3$-$x$PbTiO$_3$(BSPT) (155), and (Na$_{0.5}$ K$_{0.5}$)NbO$_3$(KNN) (156). All above reports support the existence of the microwave dielectric dispersion in ferroelectrics below the Curie point $T_C$. In most of those studies, this dispersion seems closer to a Debye-like relaxation, while the resonant character (152; 147; 144) has been clearly reported as well.

Here, we only summarize the common features of such a dispersion according to the experimental reports. In general, the dispersion frequency ($f_D$), which is habitually determined from the frequency corresponding to the peak of the loss (tan$\delta$) or imaginary part $\varepsilon''$ is located between 0.5 to 10 GHz. It is almost independent of temperature, except at temperatures near or through the phase transitions (146; 143; 147; 155). For the same material with different mean grain size, the fine grain size samples show a higher $f_D$ (148; 144). The dispersion strength ($\Delta\varepsilon$), which is defined as the difference of the $\varepsilon'$ far below and above the $f_D$, increases by increasing temperature (147). Poling and bias fields decrease the $\varepsilon'$ and tan$\delta$ (141; 145), and shift the $f_D$ to higher frequencies after poling (145). The existence of this dispersion in the paraelectric phase has been reported (157).

In a given ferroelectric system and apart from crystal anisotropy, single crystals possess larger piezoelectric and dielectric properties than ceramics of the same composition. Therefore, growth of high quality PZT single crystals is of lasting interest to the researchers (158; 159; 160; 161; 162). In single crystals, the influence of grain boundary and grain coupling on the dielectric properties could be excluded. If we can measure the dielectric properties in a single crystal sample in monodomain state (without domain walls), the contributions from the domain wall motion could also be eliminated. Then we could approach the intrinsic dielectric properties, which is essential for the understanding of the origin of the high performance in PZT. Up to the present, large-dimension PZT single crystals, which could be used for the microwave dielectric characterization, are still not available. Nevertheless, there are adequate and reliable reports in literature on the microwave dielectric properties of BaTiO$_3$ single crystals with multidomain (or polydomain) or single domain state. A survey of this works may shed some light on the origin of microwave dielectric dispersion.

According to the work by Fousek (163), Benedict and Durand (164), Lurio and Stern (165), Nakamura and Furuichi (166), and Ballantyne (167), the microwave dielectric dispersion is present in multidomain BaTiO$_3$ single crystal below $T_C$, and is apparently absent in single domain BaTiO$_3$ single crystal below $T_C$. The decrease of $\varepsilon'$ below $T_C$ at microwave frequency

region are mainly attributed to piezoelectric clamping of the macroscopic sample. The absence of the dielectric dispersion above the $T_C$ up to millimeter frequency region was consistently reported. Those observations along with the previous reports on ferroelectric ceramics, clearly indicate that the microwave dielectric dispersion in polycrystalline ceramics is intimately related to the domain structure, and is most likely due to the individual and coupled vibrations of grains and/or domains (157).

### 4.1.2 Explanations and theoretical treatments

There are three main theoretical interpretations of dispersion, based on vibrations of ions, grain resonance, and domain motion and resonance.

The earliest attempts to explain the microwave dielectric dispersion in ferroelectric $BaTiO_3$ ceramics were made by Mason and Mathias (168). In their model of $BaTiO_3$, the dielectric relaxation of the permittivity occurs in a certain frequency region, which is determined primarily by the jumping of the titanium ions between the different potential minima in the unit cell of the substance. By making specific assumptions about the size of the potential well separating Ti equilibrium positions, the relaxation frequency was placed in the microwave frequency region. The problem with this model, however, is that the relaxation relies on an ionic polarization mechanism, and the expected relaxation would properly be observed at a higher optical frequency region, around $10^{12}$ Hz, since the frequency is reversely proportional to the linear dimensions of the distance between the potential minima.

Devonshire (53) suggested that the microwave relaxation phenomenon was due to piezoelectrically active domains. In an unpoled ceramic, individual grains consist of polarized domains oriented in various directions. Consequently, the sample is macroscopically piezoelectrically inactive. In an alternating field there is no vibration of the sample as a whole, however, the *domains* remain piezoelectrically active, whereby individual or coupled groups of domains can vibrate. Thus, it is expected that the effective resonance frequency will be approximately equal to that of a single domain. Since resonance frequencies are inversely proportional to linear dimensions, domain widths on the order of microns should yield resonance frequencies in the microwave frequency region.
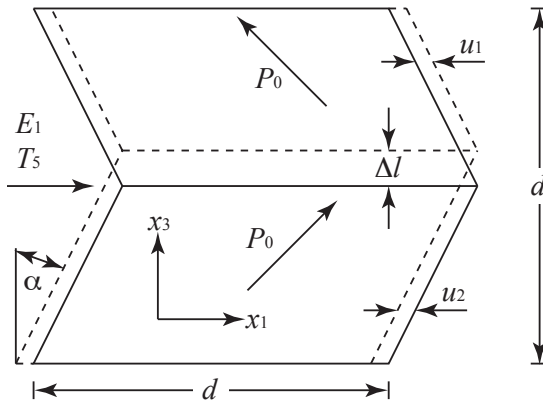
The frequency dependence of ferroelectricity, including the apparent disappearance of the ferroelectric response in the microwave region was considered by von Hippel (169). In a ferroelectric materials, such as $BaTiO_3$, permanent electric dipole moments are constructional elements of the crystal structure and are therefore, in general, firmly anchored in place, and not available for free rotation. High frequency relaxation was attributed to the change of the permanent net moment and with it, the creation of a mechanical deformation that travels with the velocity of sound. Since individual grains have dimensions on the order of $10^{-3}$ cm, and since the velocity of sound is about $10^5$ cm/sec, resonance frequencies in the 100 MHz range are expected.

Later, this explanation was tested by Xi, McKinstry and Cross (152) in the $LiNbO_3$ ce-

ramics. Since $LiNbO_3$ possesses only $180°$ domains, the frequency of domain resonance can be readily related to the grain size. They observed a dispersion around $10^8$ Hz, with a distinct *resonant character*. The $\varepsilon'$ increased slightly, then decreased rapidly before saturating out to its clamped value. The corresponding $\tan\delta$ passed through a maximum in the same frequency region. Using an equivalent circuit model for the coupling individual grain resonances by simulation, they quantitatively described real and imaginary component of the permittivity. The resonant frequency, $f_r$ of a grain is given by Eq. 4.1:

$$f_r = \frac{1}{2\pi\sqrt{L_1 C_1}} = \frac{1}{2g\sqrt{\rho s^E}}, \tag{4.1}$$

where $C_1 = (\varepsilon^T - \varepsilon^S)\varepsilon_0 g$, $L_1 = \rho g s^E/(\pi^2(\varepsilon^T - \varepsilon^S)\varepsilon_0)$, $g$ is the grain size, $\varepsilon^T$ and $\varepsilon^S$ are the dielectric constant under constant stress and constant strain, $\rho$ is the density and $\varepsilon_0$ is the permittivity of free space. $s^E$ is the mechanical compliance of $LiNbO_3$ crystal under a constant electric field. Note that the $s^E$ used in this reference is not referred to a specific mechanical compliance coefficient. Since there are three independent constants in the compliance coefficient matrix of the Curie group ($\infty\infty m$) (i.e., $s_{11}$, $s_{12}$ and $s_{44}$), we consider the $s^E$ as an average among them. Normally $s_{44}=s_{55}$ possesses the largest value among the three compliance coefficients, therefore the average $s^E$ should be less than $s_{55}$, which is equal to $1/c_{55}$ (170). Eq. 4.1 suggests that $f_r$ is inverse of the grain size $g$. A number of piezoelectric equivalent circuits were connected together to simulate the coupled resonant behavior of grains of different size and orientation in a ceramic. Circuit simulation software was used to determine the complex impedance of the network, from which dielectric parameters were obtained. The calculated spectra were in excellent agreement with the measured spectra.



**Figure 4.1:** A pair of domains with a $90°$ domain wall (bold line), embedded in an elastic and dielectric medium. The shift of the wall and the displacement of the masses is shown with dashed lines. Taken from Arlt, Böttger and Witte. (171)

Arlt *et al* (171; 148) proposed the existence of strong Debye-like relaxation in ferroelectrics due to the emission of gigahertz shear waves from ferroelastic domain walls. In tetragonally distorted perovskites, the minimization of free energy results in a characteristic domain configuration in which the domains form regular stacks with $90°$ domain walls between the laminar

domains. In an alternating field, above the acoustic resonance of the bulk sample and individual grains, domains can still be deformed, but the overall shape of the grain is preserved. The domain walls shift, resulting in a gross shear of the stack composed of lamellas of domains, and the 90° domain walls can be modeled as shear wave transducers. Having considered a pair of domains separated by a 90° domain wall such as depicted in Fig 4.1, Arlt demonstrated that the relaxation should be "Debye-like" where the frequency dependence of the total permittivity is governed by

$$\varepsilon_{\text{total}} = \frac{D_1}{\varepsilon_0 E_1} = \varepsilon_\infty + \frac{\Delta\varepsilon}{1 + i\omega\tau}, \tag{4.2}$$

with the relaxation step, $\Delta\varepsilon$, given by,

$$\Delta\varepsilon = \frac{2P_0^2}{\varepsilon_0 kd} = \frac{P_0^2}{2\varepsilon_0 c_{55}^* S_0^2} = \frac{1}{2\varepsilon_0 c_{55} Q^2 P_0^2}, \tag{4.3}$$

and the relaxation time, $\tau$, given by,

$$\tau = \frac{2Z_m S_0^2}{k} = \frac{d}{2v_{55}}. \tag{4.4}$$

In Eqs. 4.2 – 4.4, $D_1$ is the dielectric displacement, $E_1$ is the electric field, $\varepsilon_\infty$ is the intrinsic permittivity, $\omega$ is the angular frequency, $P_0$ is the spontaneous polarization, $S_0$ is the spontaneous strain, $c_{55}^*$ is the stiffness constant, $d$ is the grain size, and $Z_m$ is the input acoustic impedance of the surrounding media. The elastic shear stiffness constant of the grain in the rotated coordinate system defined by Fig 4.1 is given by $c_{55}^* = \frac{1}{4}\left(c_{11}^D + c_{33}^D - 2c_{13}^D\right)$, where $c_{11}^D$, $c_{33}^D$ and $c_{13}^D$ are the constants in the normal coordinate system. In arriving at Eqs. 4.3 and 4.4, a force constant per unit domain wall area, $k = 4c_{55}^* S_0^2/d$ and the phase velocity, $v_{55} = \sqrt{c_{55}^*/\rho}$, have been used. The relaxation frequency, $f_{u(\text{Arlt})}$, is related to the relaxation time, $\tau$, through $f_{u(\text{Arlt})} = 1/(2\pi\tau)$. Using Eq. 4.4 it follows that

$$f_{u(\text{Arlt})} = \sqrt{\frac{c_{55}^*}{\rho}} \cdot \frac{1}{\pi d} = \frac{1}{\sqrt{s_{55}^*\rho}} \cdot \frac{1}{\pi d}. \tag{4.5}$$

The domain wall emits shear waves when its thickness is much larger than the wavelength of the emitted acoustic wave. However, when the domain wall diameter is smaller than the wavelength of the emitted shear wave, the acoustic input impedance, $Z_m$, must be replaced by a complex impedance, which is strongly frequency dependent. Consequently, for large emitters (i.e., domain wall diameters $\geqslant$ the sound wavelength), the relaxation is Debye-like, as suggested by Eq. 4.4, however for small emitters (i.e., domain wall diameters $\leqslant$ the sound wavelength), the solution for $\varepsilon_{\text{total}}$ shows a decrease over a much broader frequency range (171; 148). Note that the Eq. 4.5 is derived from an oversimplified model. According to Fig 4.1, a 90° domain wall is developed during cooling from a free square paraelectric crystallite with a width of $d$. In this case, the domain width $d$ is comparable to the grain size $g$. We note that this is not so in real samples. In BaTiO$_3$ and in many other ferroelectrics several or many domain walls form regular or periodic stacks instead of being uncorrelated to each other. In this case the

domain size $d$ is much smaller than the grain size $g$. Since the accurate determination of the domain size is rather difficult, the estimation of the $f_{u(\text{Arlt})}$ based on Eq. 4.5 through the grain size would generate a much lower $f_{u(\text{Arlt})}$ compared with the value determined by experimental data.

### 4.1.3   Evaluation of the extrinsic domain wall contributions

It is well known that in ferroelectric materials the motion of domain walls accounts for a large part of the experimentally observed piezoelectric and dielectric response (61; 49; 172; 173; 174). In practice, the domain wall contributions are most often controlled by dopants, leading to electromechanically hard or soft materials.1 In addition to dopants, domain wall contributions are dependent on microstructure and crystal structure of ceramics and, in general, it is found that the density of domain walls, domain structure, domain wall mobility and the ceramics grain size are inter-related, and all depend on dopant concentration (119; 42). Within such a complex relationship among many parameters that influence properties it is difficult to separate effects due to individual factors. It is advantageous when intrinsic properties are known either from a theory or direct measurements. This is unfortunately not the case for PZT, where single crystal data are not available and for which intrinsic (lattice) properties can be obtained only indirectly from the phenomenological Landau-Ginzburg-Devonshire (LGD) theory. One approach in separating lattice and domain wall contributions has been to measure the properties of ceramics as a function of temperature and compare them with those obtained from the LGD theory (70). The difference between these obtained values is taken as an estimate of domain wall contributions. A good agreement between the dielectric properties measured in ceramics at low temperatures where domain walls are assumed to be frozen and values predicted from the LGD theory were taken as an indication that this method works well (50). However, the recent discovery of a monoclinic phase in the MPB region of PZT (33) has put some doubts in estimates derived from LGD approach based only on tetragonal and rhombohedral phases.

Another approach to estimate domain wall and lattice contributions is to examine properties of ferroelectric ceramics as a function of frequency. The microwave dispersion can be attributed to the motion of domain walls. It is reasonable to assume that above this dispersive region the properties approach their intrinsic values. Interestingly, while temperature dependent measurements performed in the conventional frequency range clearly indicated expected differences in domain wall contributions for soft (donor-doped) and hard (acceptor-doped) materials which disappeared at low temperatures (70), it is not known whether such behavior is reflected in the "microwave" range. In this chapter we combine the microwave dielectric spectroscopy and low temperature dielectric measurements to study domain wall contributions to the dielectric properties of undoped, Nb-, and Fe-doped PZT with the same composition near MPB. The motivation is to see whether permittivity measured beyond the frequency range of the microwave dispersion is a good estimate of the intrinsic permittivity. If so, those measurements can be used to investigate extrinsic contributions to the permittivity as a function of temperature and can be

compared with the existing estimates based on LGD theory. Furthermore, it is of interest to see whether dopants and domain configuration significantly affect the permittivity at frequencies above the microwave dispersion range.

## 4.2   Experimental descriptions

### 4.2.1   High frequency dielectric characterization (1 MHz to 1.8 GHz)

For dielectric characterization, poling, and electromechanical measurements, the samples were shaped into the form of small cylinders, with typical dimensions of about 0.9 mm in diameter and 5 mm in length. The base surfaces (perpendicular to the length direction) were electroded gold by sputtering. The impedance spectra in the frequency range from 1 MHz to 1.8 GHz were collected by means of HP4396A network analyzer. Nonuniform fields distribution across the sample has been accounted for during permittivity calculation (156). For each composition the dielectric spectra were collected first starting with a well aged unpoled state and then immediately after each poling step. In order to produce intermediate poling states PZT and KNN samples were exposed to incrementally increasing electric field $E_z$ at ambient temperature. The exposure time was typically about 30 min. In the final state, corresponding to the highest field intensity, samples reached values of piezoelectric coefficient $d_{33}$ and electromechanical coupling $k_{33}$ typically reported for their composition. BSPT66-Mn samples initially were in a fully poled state, which was reached as described in Ref. (175). Its intermediate states were obtained by thermal depoling at incrementally increasing temperatures. Temperature dependences dielectric spectra of poled samples were measured using Delta Design 9023 temperature chamber.

### 4.2.2   Microwave dielectric characterization (3 GHz to 20 GHz)

From 3.4 GHz to 20.2 GHz the method of sleeve resonator was employed (176). Transmission spectra around $TE_{011}$-mode and its radial harmonics $TE_{0m1}$ were acquired by HP 8722D Network Vector Analyzer. It is necessary to point out here that $\varepsilon'$ and $\varepsilon''$ obtained at these resonant modes are probed exclusively by azimuthal electric field component $E_\Theta$, whereas the former method (1 MHz$-$1.8 GHz) provides dielectric constant values probed by $E_z$ component. Here we assume cylindrical system of coordinates, where sample axis is taken as $z$-axis. Therefore, direct comparison between two datasets is possible for isotropic samples only. Note that The method used to obtain the dielectric properties at high frequency is based on isotropic materials. After poling, due to anisotropic properties, the method could not give us any information. The only one point shown for poled samples is just a rough estimation. Temperature dependences dielectric spectra were measured also using Delta Design 9023 temperature chamber.

### 4.2.3  Determination of elastics, dielectric and piezoelectric coefficients

The samples used for microwave dielectric characterization are typically small cylinders, in which the diameter is much smaller than the length. The poling is always performed by applying the electric field along the longitudinal direction. The longitudinal piezoelectric resonance (i.e., the extension mode) could be excited along such a poling direction. In order to evaluate the poling effect, we can make use of the longitudinal piezoelectric constant $d_{33}$ and electromechanical coupling factor $k_{33}$ as indexes. Those coefficients were determined by the resonance method (177). For the impedance spectrum, a HP4194A impedance analyzer was used.

First we determine the sound velocity $V_s$ through Eq. 4.6

$$V_s = 2l f_{\text{anti}}, \tag{4.6}$$

where $l$ is the length of the rod, and $f_{\text{anti}}$ is the antiresonance frequency, which is determined from the frequency corresponding to the maximum impedance. $s_{33}^D$ is expressed as

$$s_{33}^D = \frac{1}{\rho V_s^2}, \tag{4.7}$$

where $\rho$ is the density of sample. The $k_{33}$ is defined as

$$k_{33} = \sqrt{\frac{\pi}{2} \cdot \frac{f_{\text{reso}}}{f_{\text{anti}}} \cdot \tan\left[\frac{\pi}{2} \cdot \frac{(f_{\text{anti}} - f_{\text{reso}})}{f_{\text{anti}}}\right]}, \tag{4.8}$$

where $f_{\text{reso}}$ is the resonance frequency, which is determined from the frequency corresponding to the minimum impedance. The quasistatic dielectric constant $\varepsilon_{33}^T$ is obtained by Eq. 4.9

$$\varepsilon_{33}^T = \frac{C_0^T l}{A}, \tag{4.9}$$

where $C_0^T$ is capacitance of the rod measured at 1 kHz and $A$ is the area of the main surface. Combining with $s_{33}^D$ and $k_{33}^2$, we can calculate $s_{33}^E$

$$s_{33}^E = \frac{s_{33}^D}{1 - k_{33}^2}, \tag{4.10}$$

and $d_{33}$

$$d_{33} = k_{33} \cdot \sqrt{\frac{\varepsilon_{33}^T}{s_{33}^E}}. \tag{4.11}$$

The mechanical quality factor $Q_m$ is determined through Eq. 4.12

$$Q_m = \frac{1}{2\pi f_{\text{reso}} C_0^T Z_{\text{min}}} \cdot \frac{f_{\text{anti}}^2}{f_{\text{anti}}^2 - f_{\text{reso}}^2}. \tag{4.12}$$
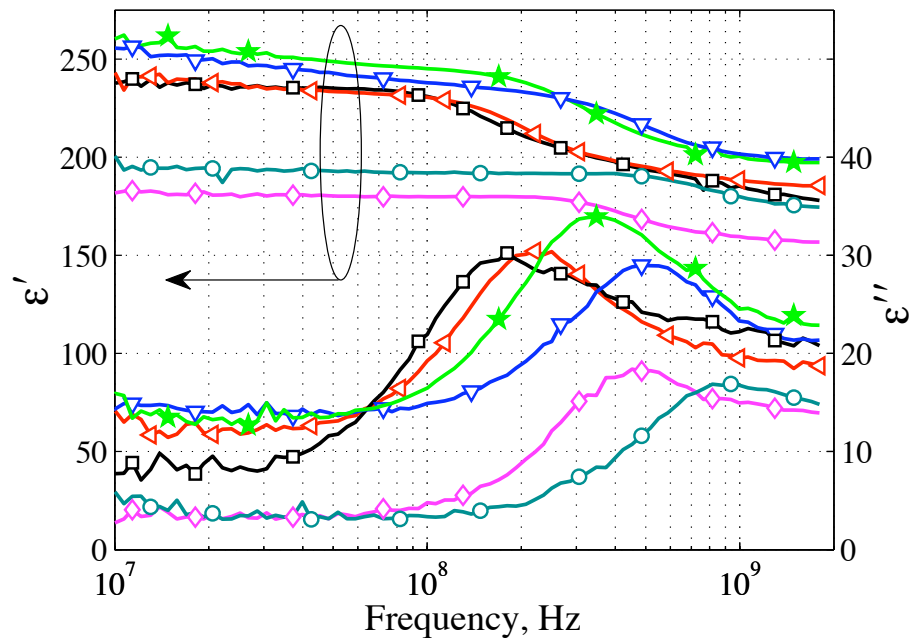
where $Z_{\text{min}}$ is the impedance corresponding to the $f_{\text{reso}}$.

## 4.3   Microwave dielectric dispersion

We first discuss dielectric dispersion at microwave frequency and discuss its origins. The microwave dielectric dispersion is studied first in rhombohedral PZT ceramics, since these rhombohdral PZT samples could be readily poled.

### 4.3.1   Rhombohedral PZT ceramics

In unpoled state all samples, soft and hard alike, exhibited strong dispersion in agreement with earlier studies (148; 146). The loss spectra reveal single peak located from 0.7 to about 3.4 GHz. The upper bound of this range was determined by means of the sleeve resonator technique (176). The data are not shown here. Hereafter the frequency of corresponding loss maximum will be referred to as $f_u$. For poling, the samples were exposed to the voltage equivalent of 25 kV/cm at $100-130\,°C$. The field was kept on for at least 30 min. at elevated temperature and during cooling. Once the samples had been poled their electro-mechanical properties (e.g. coupling coefficient $k_{33}$, sound velocity $V_s$, etc.) were determined by means of piezoelectric resonance method employed in the longitudinal-bar mode. The results for $k_{33}$ (see Tab. 4.1) agree with the values typically reported for PZT indicating that the samples were fully poled.
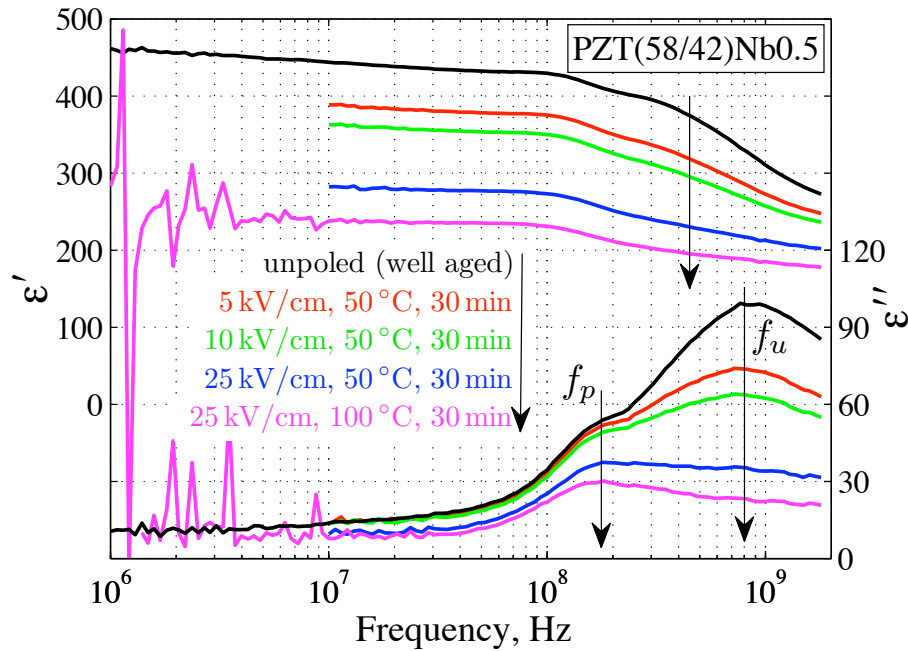


**Figure 4.2:** Permittivity $\varepsilon'$ and loss $\varepsilon''$ spectra of well poled samples. The symbols are introduced solely to facilitate distinction between different data sets: □-PZT(58/42)Nb0.5; ◁-PZT(58/42)Nb0.2; ★-PZT(58/42)Nb0.7; ▽-PZT(58/42)Nb1.0; ◇-PZT(58/42)Fe0.5; ◯-PZT(58/42)Fe1.0.

Fig 4.2 shows selected loss and permittivity spectra of poled samples. In well poled samples we observe single loss maximum. It is centered at somewhat lower frequencies (designated here $f_p$) compared to the peak position of corresponding unpoled state $f_u$. The separation between $f_u$ and $f_p$ amounts to at least 0.5 GHz (Fig. 4.3).

Table 4.1: Microstructural and electro-mechanical properties of studied PZT samples.

| Composition | $\bar{D}_e$ (μm) | $\bar{L}$ (μm) | $\bar{D}$ (μm) | $f_p$ (GHz) | $V_s$ (m/s) | $d_{33}$ (pC/N) | $k_{33}$ | $Q_m$ | $\lambda_A$ (μm) | Density % |
|---|---|---|---|---|---|---|---|---|---|---|
| PZT(58/42)Fe1.0 | 0.83 | 0.87 | 1.3 | 0.937 | 4073 | 77.8 | 0.51 | 59 | 4.35 | 97.6 |
| PZT(58/42)Fe0.5 | 2.13 | 2.02 | 3.32 | 0.485 | 4028 | 57.8 | 0.36 | 115 | 8.30 | 96.5 |
| PZT(58/42)Nb1.0 | 2.43 | 2.55 | 3.79 | 0.485 | 3987 | 102.7 | 0.6 | 57 | 8.22 | 95.3 |
| PZT(58/42)Nb0.85 | 2.63 | 2.58 | 4.10 | 0.398 | 3971 | 100 | 0.55 | 72 | 9.98 | 97.4 |
| PZT(58/42)Nb0.7 | 3.51 | 3.60 | 5.48 | 0.348 | 3971 | 93 | 0.53 | 73 | 11.41 | 97.7 |
| PZT(58/42)Fe0.1 | 3.89 | 3.98 | 6.21 | 0.306 | 3871 | 80.3 | 0.49 | 139 | 12.65 | 95.8 |
| PZT(58/42) | 6.05 | 5.95 | 9.43 | 0.267 | 4103 | 90 | 0.61 | 50 | 15.37 | 99.7 |
| PZT(58/42)Nb0.5 | 6.74 | 6.71 | 10.51 | 0.180 | 3964 | 88 | 0.52 | 107 | 22.02 | 96.1 |
| PZT(58/42)Nb0.2 | 10.84 | 10.44 | 16.91 | 0.221 | 4415 | 77 | 0.67 | 66 | 19.98 | 96.1 |
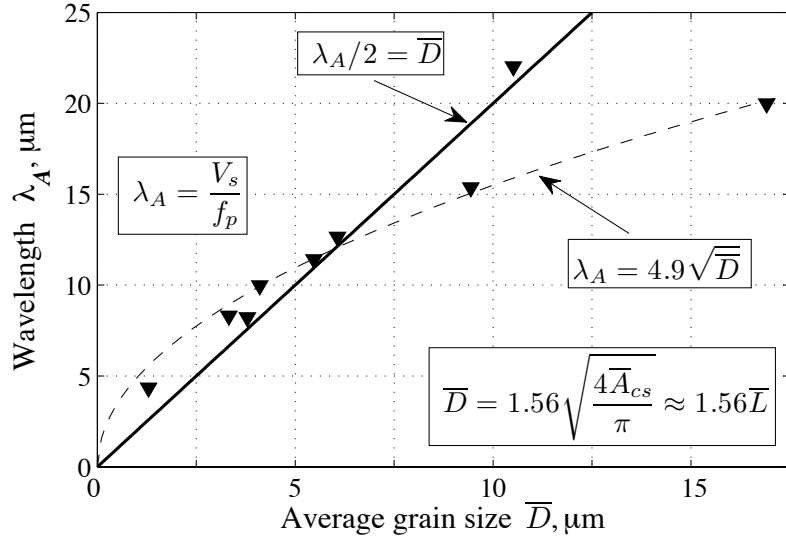
**Figure 4.3:** The influence of poling on room temperature PZT(58/42)Nb0.5 spectra. The arrows indicate evolution of spectra and corresponding consecutive poling conditions.

To learn more about the relationship between peaks in poled and unpoled ceramics, one of the samples, PZT(58/42)Nb0.5, was poled gradually. Its dielectric spectra collected first in unpoled state and then after each consecutive poling step are summarized in Fig 4.3. Rapid permittivity and loss variations below 10 MHz, which are seen here in the last spectrum, are due to piezoelectric resonances of the sample. At higher frequencies each subsequent poling step monotonously lowers permittivity and loss. More importantly, the data indicate that the loss maximum located around $f_u$ gets gradually suppressed remaining in its original position with respect to the frequency axis. Finally, it completely disappears from the spectrum in well poled samples. Meanwhile, the second peak gets revealed from the feature seen as a hump on the loss spectrum of unpoled sample. Close proximity between $f_p$ and the hump position indicates that domain configuration has no influence on corresponding polarization mechanism. The presence of such hump [seen also in PZT(58/42)Fe0.1] itself suggests that two different dissipation processes take place simultaneously in unpoled specimens. Therefore, we will discuss these processes separately.

For specimens of given composition $f_p$ proved to be reproducible within the measurement resolution and independent of sample dimensions. As $f_p$ tends to be higher for the samples with finer microstructure, an obvious choice was to look for its correlation with average grain size $\overline{D}$. We find it more convenient, however, to plot the acoustic wavelength $\lambda_A$, which corresponds to $f_p$, as a function of $\overline{D}$, as it accounts for the variation of sound velocity $V_s$ among different compositions ($\lambda_A = V_s/f_p$). The results are shown in Fig 4.4. The solid line represents here the longitudinal resonance condition $\overline{D} = \lambda_A/2$.[2] It demonstrates reasonable agreement

---

[2]The other one-dimensional modes are expected to provide similar resonance criteria in given circumstances.

**Figure 4.4:** The acoustic wavelength $\lambda_A$, which corresponds to the loss peak frequency $f_p$, vs average grain size $\overline{D}$. The solid line indicates the calculated longitudinal resonance condition: $\overline{D} = \lambda_A/2$. The dashed line is the square root fit of the data.
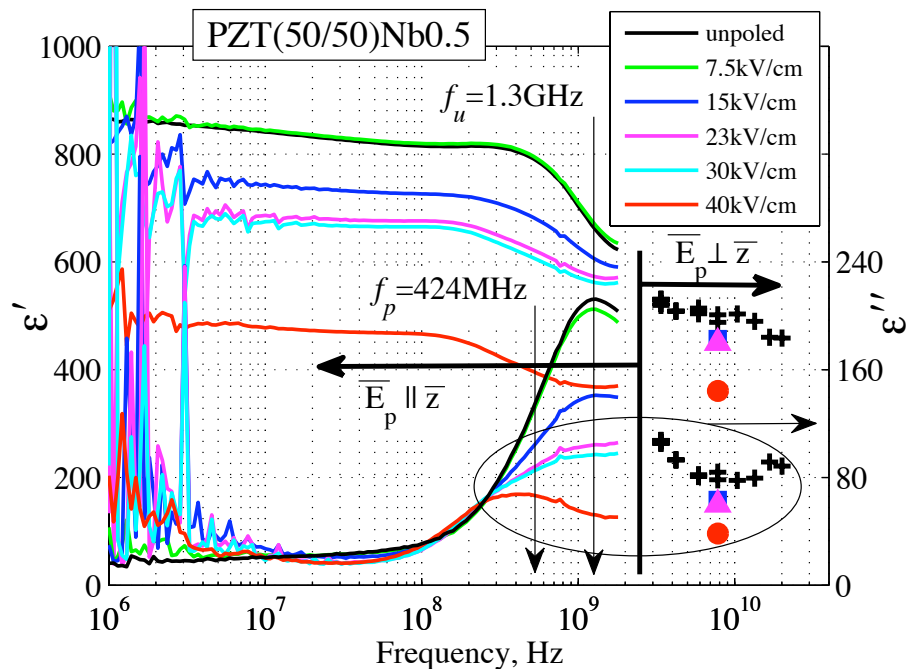
with the data for $\overline{D} < 11$ μm. It is possible to go beyond this limit using a fit based on square root function, which is shown in dashed line in Fig 4.4. Though, it does not provide any principal improvement over the linear dependence, as one of data points (at 10.5 μm) is still found considerably deviated from the fit. Square-root law could also indicate resonance of domains, whose width is reported to be proportional to $\sqrt{\overline{D}}$ (119). We exclude this possibility because square fit obtained here would suggest domain width larger than $\overline{D}$. Alternatively, one could try to find the reason for observed deviation from the linear behavior for PZT(58/42)Nb0.2, which is the composition with the largest grain size. Indeed, there is a factor that, in our opinion, may explain it. Namely, it is known that the grains smaller than about 10 μm tend to contain a single stack of lamellar domains, whereas larger grains split into several clusters (119; 65). At present it is not clear how well boundaries between such clusters can scatter acoustic waves and how they are affected by poling. However, it is not unreasonable to assume that a cluster of lamellas could behave as a grain with effective size that is smaller than the size of the whole grain. On condition that this assumption is correct, $f_p$ is expected to saturate for coarse-grain ceramics. Having that in mind, we can draw the following conclusion. The tendency for $\lambda_A$ to be linearly dependent on $\overline{D}$ considered together with the fact that $f_p$ does not depend on the poling state (i.e., domain pattern), indicates that the piezoelectric resonance of grains is responsible for the loss peak observed around $f_p$. This conclusion should be applied with the reservation that it concerns the ceramics with grain size smaller than about 11 μm.

Drastic suppression of dispersion around $f_u$ induced by poling supports the idea that it is of domain-related nature. The best explanation for such poling behavior can probably be offered by the model of the shear wave sound emission (171). It essentially implies constructive interference of acoustic waves in periodic domain structures. Poling is expected to break the domain wall periodicity and density. However, other domain wall processes cannot be excluded. We

shall discuss this possibility more in section 4.3.2.

## 4.3.2    Tetragonal PZT and other perovskite ferroelectric ceramics
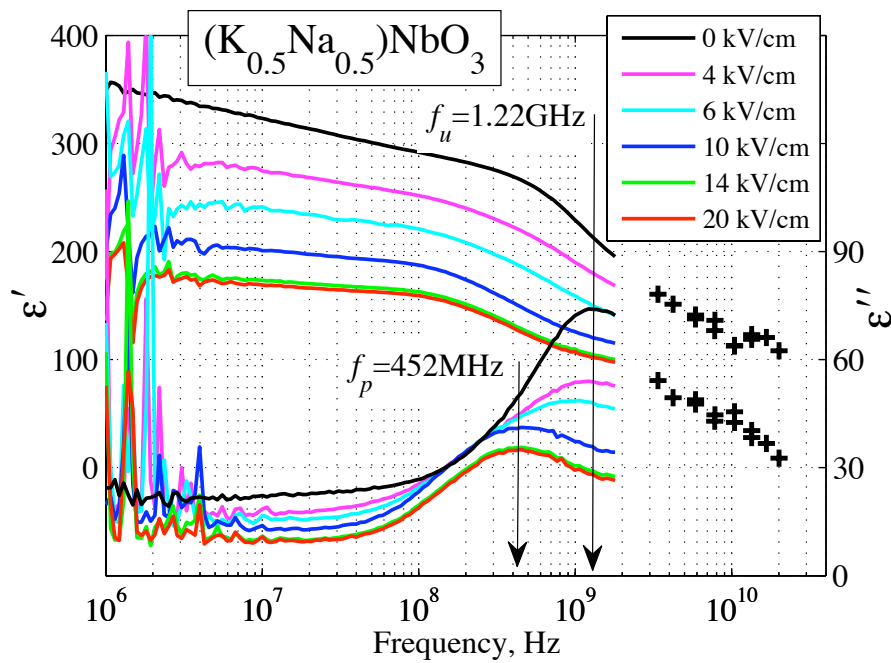
Let us consider first room temperature spectra of unpoled ceramics.[3] In the case of tetragonal PZT(50/50)Nb0.5 the spectrum of unpoled ceramics is very close to the spectrum obtained after treatment with the field of 7.5 kV/cm (shown in green in Fig. 4.5). In agreement with earlier reports, PZT, KNN and BSPT exhibit deep dispersion at microwaves (146; 148; 155). The permittivity of PZT(50/50)Nb0.5 demonstrates a drop from about 850 to 460. In KNN (Fig 4.6) and BSPT66-Mn (Fig 4.7) $\varepsilon'$ reduces from 360 to 100 and from 850 to 200 respectively. The value of $\varepsilon'$ at 20.1 GHz observed in KNN sample agrees very well with recent time-domain THz data reported in the range from 0.25 to 1.0 THz for fine- and coarse-grained KNN ceramics (178). In the case of BSPT66-Mn permittivity at 20.1 GHz is about twice as high as the net polar phonon contribution (155). All our samples demonstrate well pronounced single loss peak. The frequency of loss maximum $f_u$ is about 1.3 GHz for PZT(50/50)Nb0.5 and KNN (see Figs 4.5 and 4.6). In BSPT66-Mn it is much broader and appears at somewhat lower frequency of 588 MHz.
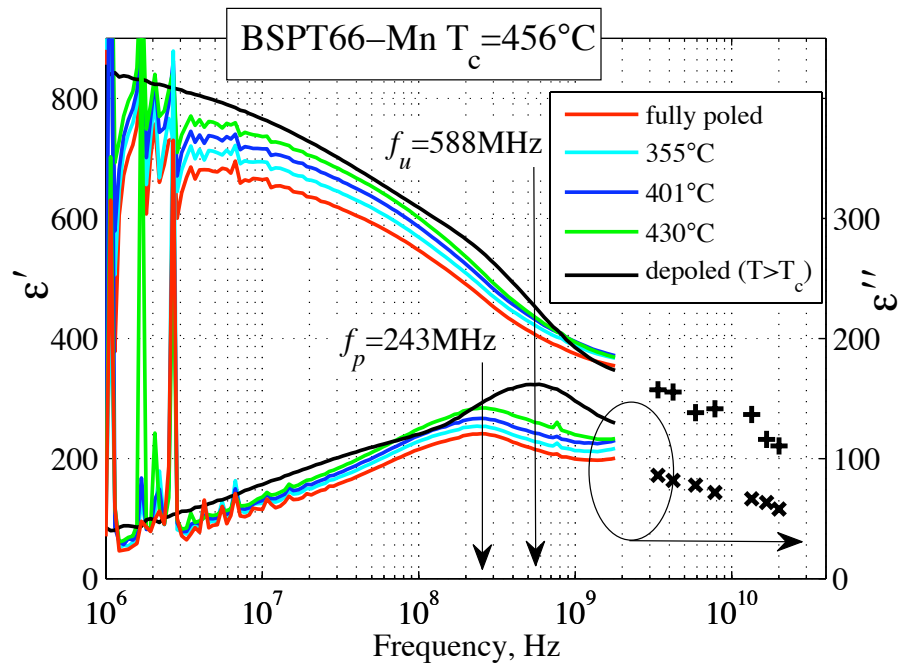


**Figure 4.5:** Room temperature permittivity $\varepsilon'$ and loss $\varepsilon''$ spectra of PZT(50/50)Nb0.5 measured after consequent poling treatment. The electric field intensity for each poling step is shown in the legends.

With respect to poling the evolution of spectra shown in Figs 4.5 and 4.6 is similar to the response of rhombohedral PZT discussed in section 4.3.1. Namely, application of electric field leads to progressive suppression of the loss peak observed around $f_u$. The field intensity, at which this process becomes evident is rather low compared to the coercive field $E_c$. For example, more than a twofold reduction of loss $\varepsilon''(f_u)$ is observed in KNN after exposure

---

[3]By *unpoled* we understand as sintered, aged ceramics, for which macroscopic remnent polarization $P_r$ is assumed to be zero.
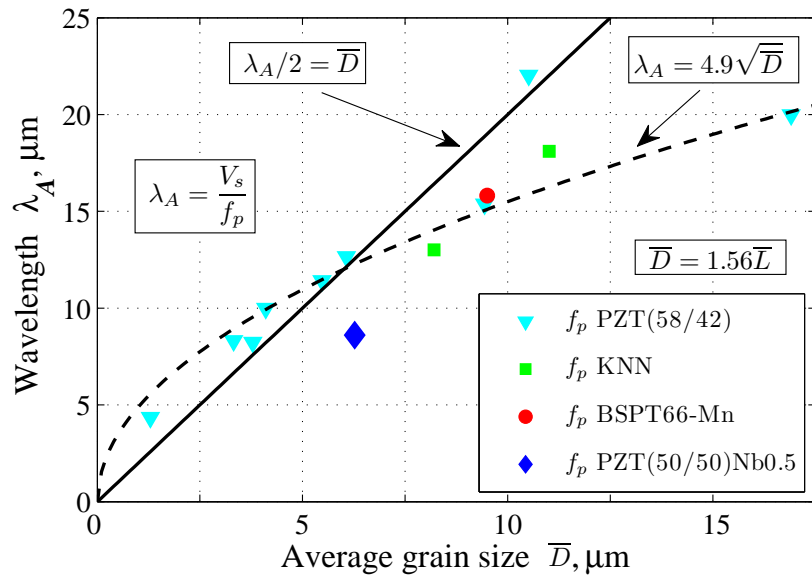
**Figure 4.6:** Room temperature permittivity $\varepsilon'$ and loss $\varepsilon''$ spectra of $(K_{0.5}Na_{0.5})NbO_3$ measured after consequent poling treatment. The electric field intensity for each poling step is shown in the legends.



**Figure 4.7:** Room temperature permittivity $\varepsilon'$ and loss $\varepsilon''$ spectra of BSPT66-Mn. Initially fully poled sample was treated at elevated temperatures, shown in the legend, to reduce remnant polarization.

with 10 kV/cm, while well open saturated loops indicate $E_c \sim 20$ kV/cm. As loss value decreases, no peak shift along frequency axis is observed. At 7.8 GHz permittivity and loss of PZT(50/50)Nb0.5 both reduce gradually with increasing poling field intensity as indicated in Fig 4.5 with color symbols. Finally, the $f_p$ gets revealed at somewhat lower frequency. For BSPT66-Mn the effect of the depoling on the dielectric properties is depicted in Fig 4.7. This sample was initially poled showing a loss maximum at 243 MHz. The final state was reached via gradual thermal depoling. In the intermediate states the spectra show gradual increase of loss in the frequency range above 10 MHz. However, the position of loss maximum $f_p$ does not change until annealing at $T > T_C$. Once $T_C$ was crossed the spectrum became smooth below 10 MHz indicating disappearance of piezoelectric resonances. At the same time loss increased considerably reaching a new maximum at 588 MHz.



**Figure 4.8:** Correlation between the average grain size $\overline{D}$ and the acoustic wavelength that corresponds to the frequency of loss peak in poled samples $f_p$. The solid line indicate mechanical resonance condition: $\overline{D} = \lambda_A/2$.

In Sec. 4.3.1, it has been suggested that the dispersion taking place around $f_p$ originates from piezoelectric resonances of individual grains. This argument is based on the observation of simple linear relationship between average grain size $\overline{D}$ and acoustic wavelength $\lambda_A$, which corresponds to $f_p$ and the velocity of sound $V_s$. With $f_p$ values from Figs. 4.5, 4.6 and 4.7 we can update a plot of acoustic wavelength $\lambda_A$ versus average grain size $\overline{D}$ as shown in Fig 4.8.

On the whole, our new data indicate the same linear trend. Though, the deviation from the resonance condition is noticeable. Among the reasons for such deviation one might suspect rather rounded shape of the loss peak, which may make difficult determination of $f_p$, which is prone to distortion due to the proximity of another polarization mechanism taking place at $f_u$. Besides that, the choice of elastic constant, through which the sound velocity is calculated, is somewhat arbitrary. It is conditioned simply by the convenience of experiment and the fact that $s_{33}^D$ gives sound velocity $V_s$ which is quite close to its upper limit, see for example Tab. 4.2.

These circumstances suggest that the $\lambda_A$ vs. $\overline{D}$-plot as shown in Fig 4.8 is probably at its limits of providing any further evidence either in favor or against the idea of piezoelectric resonance of individual grains being responsible for the dispersion observed around $f_p$. Therefore, it is necessary to approach this problem from a different angle. Such opportunity naturally appears, if we consider the temperature dependence of loss maximum in the poled state $f_p(T)$.

**Table 4.2:** Comparison of sound velocities (m/s) corresponding to some piezoelectric resonance modes. The numerical values for elastic constants and densities are taken from Refs. (175; 179; 180). The last raw corresponds to effective shear sound velocity. $\sigma$ is Poisson ratio.
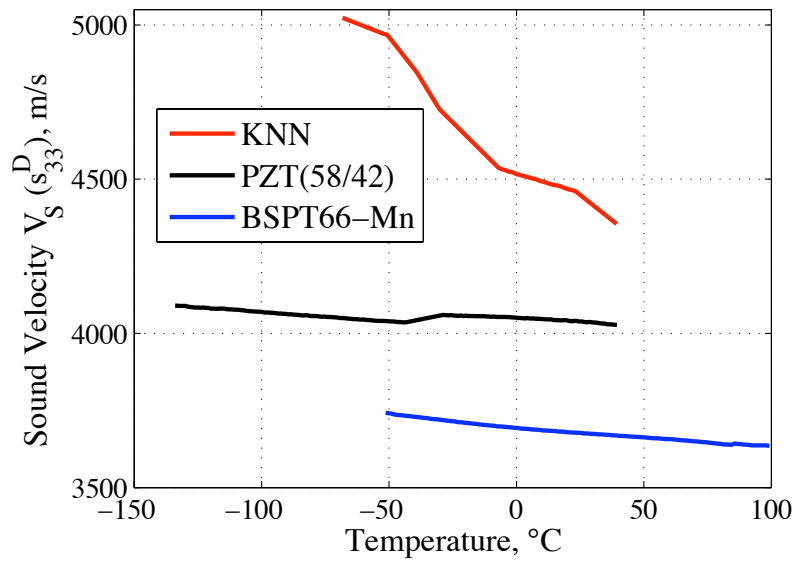
|  | BSPT66-Mn | PZT(50/50)Nb0.5 | BaTiO$_3$ | PZT(58/42) | KNN |
|---|---|---|---|---|---|
| $(c_{33}^D/\rho)^{1/2}$ | 4359 | 4227 | 5477 | 4550 | 6922 |
| $(c_{11}^E/\rho)^{1/2}$ | 4111 | 3965 | 5130 | 4304 | 6636 |
| $(s_{33}^D\rho)^{-1/2}$ | 3840 | 3764 | 4970 | 4020 | 5914 |
| $(s_{11}^E\rho(1-\sigma^2))^{-1/2}$ | 3457 | 3459 | 4598 | 3690 | 5495 |
| $(s_{11}^E\rho)^{-1/2}$ | 3291 | 3268 | 4390 | 3530 | 5225 |
| $(c_{44}^D/\rho)^{1/2}$ | 2560 | 2325 | 3162 | 2445 | 3765 |
| $(c_{44}^{*D}/\rho)^{1/2}$ | 2304 | 2267 | 3013 |  |  |

Indeed, for the piezoelectric resonance of individual grains the following expression, which is similar to Eq. 4.1, should hold
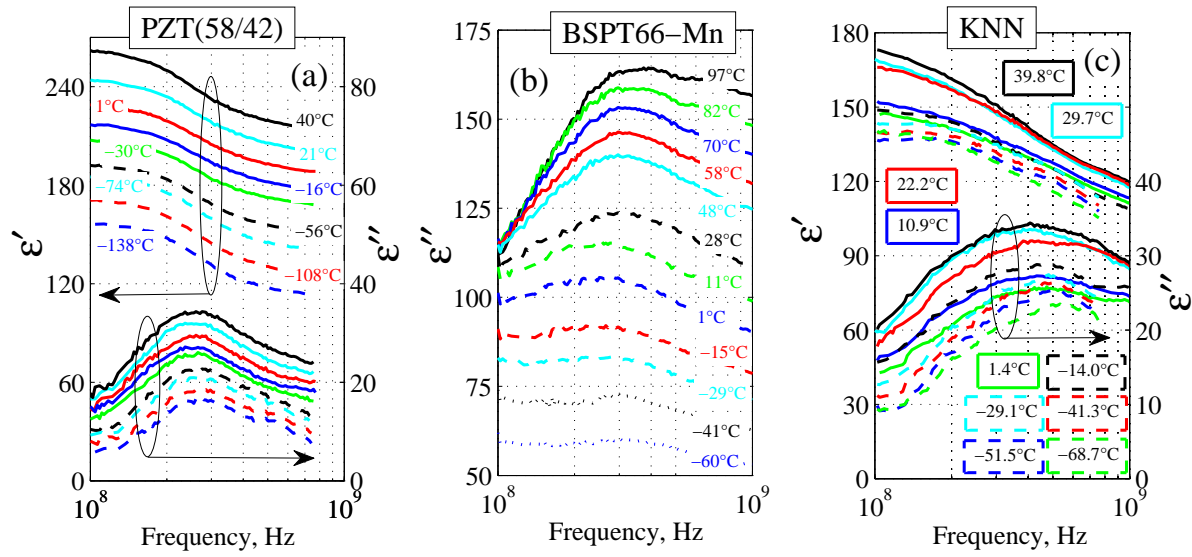
$$f_p(T) = \frac{V_s(T)}{2\overline{D}} = \frac{1}{\sqrt{\rho s_{33}^D(T)}} \cdot \frac{1}{2\overline{D}}, \qquad (4.13)$$

where $\rho$ is the sample density and $\overline{D}$ is the mean grain size. The only source of temperature dependence for $f_p$ in Eq. 4.13 is the variation of appropriate elastic constant with temperature, which is in its turn reflected in temperature dependence of sound velocity $V_s(T)$. Therefore, let us compare $V_s(T)$ with $f_p(T)$. For this experiment the following three samples were used: KNN, PZT(58/42) and BSPT66-Mn. The sound velocity as a function of temperature for them is presented in Fig. 4.9. The upper temperature limit for KNN and PZT(58/42) samples in Fig 4.9 was restricted to avoid their thermal depoling. In the case of BSPT66-Mn, the shape of loss spectra does not permit reliable extraction of $f_p$ above about 100 °C and below −50 °C, see Fig 4.10(c). Within temperature limits shown in Fig 4.9 all samples exhibit a tendency to increase $V_s$ towards low temperatures. While it is rather weak in PZT(58/42) and BSPT66-Mn, in KNN it is more pronounced resulting in an increase of $V_s$ by about 15%.

Selected spectra of poled samples around $f_p$ are shown in Fig 4.10. Permittivity and loss of PZT(58/42) monotonically go down as temperature decreases. However, the loss peak tends to preserve its shape and hardly shows any shift along the frequency axis. Essentially the same conclusion concerning $f_p$ is valid in the case of BSPT66-Mn. That shape of loss peak demonstrates far deeper variation. It resembles the behavior of BSPT without manganese, where

**Figure 4.9:** Temperature dependencies of sound velocity $V_s$ (corresponding to $s_{33}^D$ compliance constant) for poled KNN, PZT(58/42) and BSPT66-Mn samples.



**Figure 4.10:** Dielectric spectra of poled PZT(58/42), KNN and BSPT66-Mn. For BSPT66-Mn only the loss spectra are shown in panel (b). The temperatures labels are depicted within the panels. They are located either next to corresponding spectrum or the frame matches its line-style and color.

a relaxation process slows down propagating towards lower frequencies as temperature decreases (155). At low temperatures the loss intensity around fp approaches the flat background, which is due to $1/f$-noise behavior (155). The spectra of KNN demonstrate the same general trend to decrease permittivity and loss intensity towards low temperatures. At the same time, however, the loss peak tends to shift to higher frequencies. Starting from about 400 MHz at 40 °C it goes trough 500 MHz between −40 °C and −50 °C, and finally reaches 550 MHz at −70 °C. Thus, its overall variation is about 38%. Unfortunately, poor quality of data does not allow to quantify this tendency in a more detailed way reliably. These data will be discussed in section 4.3.3.

### 4.3.3 Common features in the microwave dielectric response

Let us discuss in the first place the response of samples to poling and other common features of microwave spectra. Concerning poling effects it is sufficient to follow the loss spectra $\varepsilon''$ only, because compared to $\varepsilon'$ they offer simpler interpretation in the case when a number of polarization mechanisms reveal themselves simultaneously. Despite possible overlap between different dispersion ranges, a maximum of loss still corresponds to a polarization mechanism with certain dynamical properties. The peak area or the loss value at its maximum characterizes the contribution of given mechanism to the static permittivity. As to the effect of poling, we assume that essentially it forces the domains with favorable polarization direction to grow for the expense of unfavorable ones. The latter do not have to disappear. Regarding this as a starting point, we would like to point out the following features, which are common to all our samples. The poling is found to strongly suppress the intensity of loss peak around $f_u$ revealing at the same time the loss maximum around $f_p$. Actually the presence of corresponding polarization mechanisms in all samples indicates that the crystal symmetry variation among them is not a critical factor. In other words these mechanisms can tolerate corresponding variation of domain morphology. This statement holds at least for orthorhombic, rhombohedral and tetragonal phases, which are represented by KNN (orthorhombic), PZT(58/42) series (rhombohedral), and PZT(50/50)Nb0.5 together with BSPT66-Mn (tetragonal), respectively.

As a rule above $f_u$ the loss in unpoled samples remains at rather high level indicating further dispersion at higher frequencies, which is not related to polar phonons. A comparison of $\varepsilon'$ at 20 GHz with the permittivity fit of IR-spectra suggest that there is considerable space for such dispersion (155; 178). So far we have not seen any evidence that the polarization mechanisms responsible for loss maxima at $f_u$ and $f_p$ are interrelated. Therefore, we will treat in detail the question of their microscopic origin separately.

As it has already been pointed out, the data shown in Fig 4.8 rather support the idea of simple linear relationship between $\overline{D}$ and $\lambda_A$. Concerning the temperature dependence of $f_p$, it is apparent that $f_p$ is not thermally activated, because in KNN $f_p$ shifts to higher frequencies as temperature is decreased. The temperature dependence of sound velocities $V_s(T)$ presented in Fig 4.9 being inserted into Eq. 4.13 provides a good qualitative estimation of $f_p(T)$. Quan-

titatively $V_s(T)$ for PZT(58/42) and BSPT66-Mn is expected to be better than the accuracy of $f_p(T)$-value extraction from the raw data. In the case of KNN the net shift of $f_p$ is more than twice as large as the net increase of sound velocity. According to the $V_s(T)$ shown in Fig 4.9, the $f_p(T)$ of all studied samples should shift to higher frequency as the temperature is decreased. This predication contradicts with the experimental data we have shown in Fig 4.10. At present this issue cannot be properly addressed.
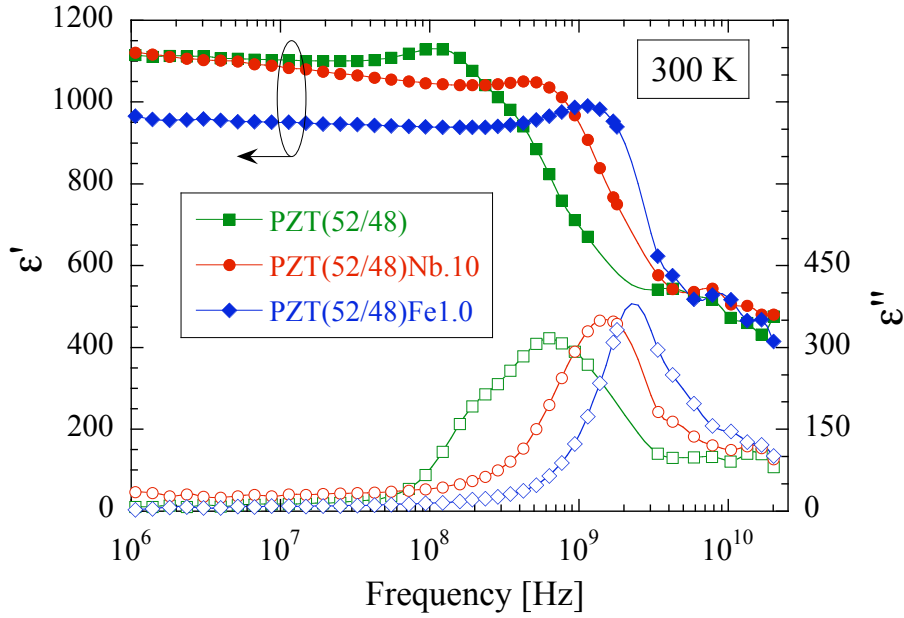
It is instructive to compare sound velocities due to different elastic constants in commonly used resonance geometries. Such comparison is presented in Tab. 4.2. For presented materials it is possible to arrange the resonance modes in descending order with respect to corresponding sound velocities. The $(\rho s_{33}^D)^{-1/2}$ values being at most just 15% lower than the larges one, makes observed $f_p$ values effectively the upper limit for the effects due to piezoelectric resonance on the scale of grain size.

Even though at present we cannot answer the question about the microscopic origin of dispersion around $f_u$, it is instructive to test the existing models against the new findings. Treating $f_p$ as a reference one could test the accuracy of Arlt's model. (171; 148; 181; 182) In its original form it was formulated for a cluster of lamellar $90°$-domains that occupy an entire grain. The essential features of this model are shown in Fig. 4.1, where the domain shape in the initial state is depicted in solid line. The position of corresponding loss maximum was estimated by Eq. 4.5. The sound velocity corresponding to $c_{55}^{*D}$ for tetragonal samples turns out to be comparable to those of $c_{44}$ as shown in Tab. 4.2. Having the structure similar to Eq 4.13, Eq. 4.5 can also be considered as the frequency, with which the sound wave of velocity $\sqrt{c_{55}^{*D}/\rho}$ covers the distance of $\pi\overline{D}$. Due to lower speed, which is always the case for positive values of $c_{13}^D$, and the distance longer by a factor of $\pi/2$, $f_{u(\text{Arlt})}$ is expected to be lower than $f_p$. In contrast with this expectation, our results show that $f_u$ is always higher that $f_p$. Knowing the grain size and elastic constants, we can estimate the ratio of $f_u$ to $f_{u(\text{Arlt})}$, to be 7.6 and 11.3 for BSPT66-Mn and PZT(50/50)Nb0.5, respectively. Even though in a more sophisticated formulation Pertsev and Arlt (183) indicated that Eq. 4.5 underestimates the frequency of loss peak in unpoled ceramics, they have not provided any means that can be readily applied in order to get more accurate result. Therefore, we believe that our comparison is instructive, as despite its limitations pointed out in Ref. (183), Eq. 4.5 has still been quite widely used (155; 178; 144).

## 4.4 Domain wall contributions in PZT ceramics at MPB

Fig 4.11 shows the $\varepsilon'$ and $\varepsilon''$ spectra of studied PZT samples from 1 MHz to 20.2 GHz at room temperature. In each spectrum we observed a good match between data sets corresponding to two aforementioned techniques. This observation speaks for reliability of our data. In agreement with earlier studies (146; 148), all samples exhibit steep dispersion of the permittivity. It sets in above 100 MHz and is accompanied by a pronounced loss maximum. Here we use the term "steep" to facilitate distinction from quasi-linear dependence of $\varepsilon'$ on $\log(f)$ associated with the nearly constant loss behavior ($1/f$-noise) (155), which is a much broader feature.
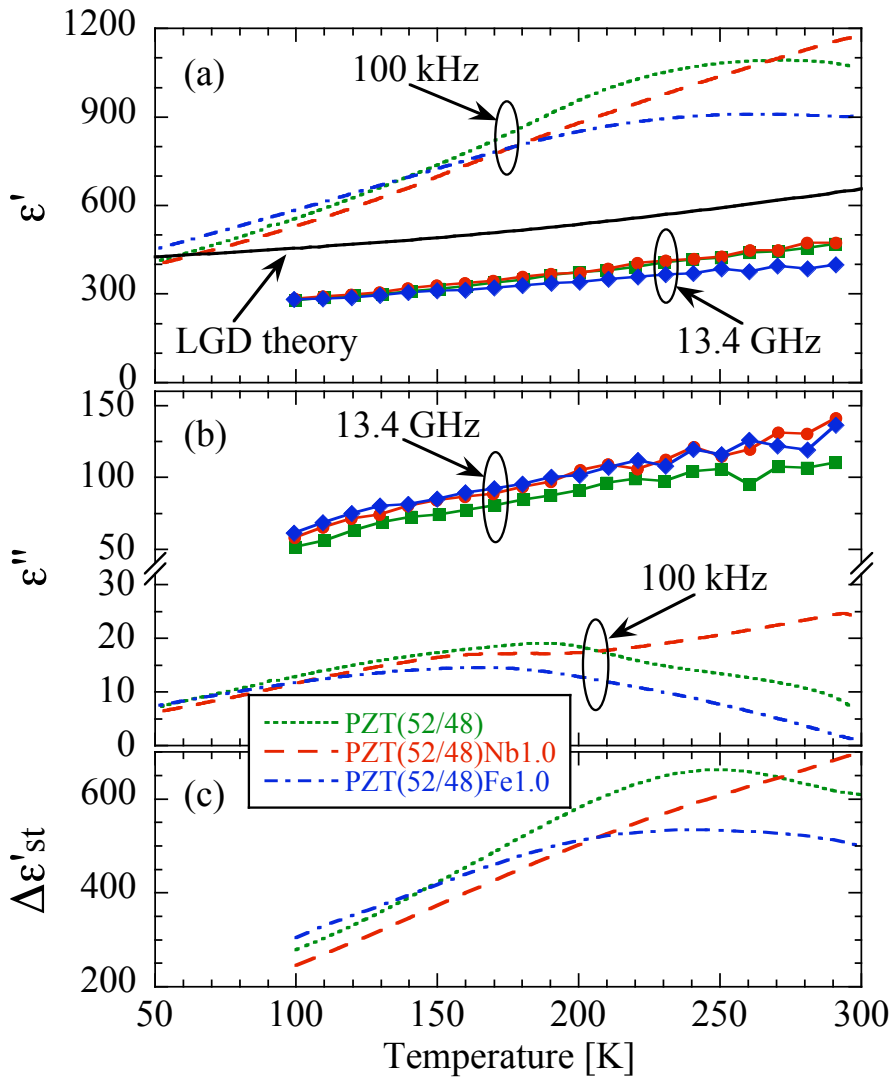
**Figure 4.11:** Permittivity $\varepsilon'$ (full symbols) and loss $\varepsilon''$ (open symbols) spectra of studied PZT samples at room temperature. The thin lines are a guide to the eye. For a given composition, $\varepsilon'$ and $\varepsilon''$ share the same color and symbol type.

The $1/f$-noise dispersion could be readily seen in Fig 4.11 in the spectra of PZT(52/48)Nb1.0 below 100 MHz. Unlike $1/f$-noise, the steep dispersion is accompanied by a pronounced loss peak. The peak's position, $f_u$, is located around 0.68 and 1.49 GHz in PZT(52/48) and PZT(52/48)Nb1.0, respectively. The loss spectrum of PZT(52/48)Fe1.0 shows a monotonous increase towards 1.8 GHz and a monotonous decrease above 3.4 GHz, indicating that $f_u$ is located between these two frequencies.

Compared to the high value of loss around the $f_u$, the loss usually falls to a relatively lower level far away below and above the $f_u$. In the case of materials studied here, all loss spectra in Fig 4.11 tend to level off above 10 GHz at the value of about 100, which is roughly 20-25% of the maximum value. This observation, in the first place, indicates a possible overlap with another process whose dispersion range centers above our upper frequency limit. We shall return to this observation later. Secondly, it is obvious that the major part of the steep dispersion is accomplished within the interval from 100 MHz to 10 GHz. Therefore, we can estimate the contribution of the steep dispersion, $\Delta\varepsilon'_{\mathrm{st}}$, to the permittivity from the difference of the permittivity far away below and above $f_u$. For convenience and easier comparison with the data in the literature we choose these frequencies as 100 kHz and 13.4 GHz; therefore $\Delta\varepsilon'_{\mathrm{st}}=\varepsilon'(100\,\mathrm{kHz})-\varepsilon'(13.4\,\mathrm{GHz})$. From earlier studies on PZT (148), BSPT (155), and KNN (156), it is known that the position of loss maximum $f_u$ observed at "microwaves" reveals negligible temperature dependence. This result gives an opportunity to estimate the temperature dependence of $\Delta\varepsilon'_{\mathrm{st}}$ from those of $\varepsilon'(100\,\mathrm{kHz})$ and $\varepsilon'(13.4\,\mathrm{GHz})$ shown in Fig 4.12(a).

The temperature dependence of $\varepsilon'(100\,\mathrm{kHz})$ is similar to previously published results for MPB region (70; 184; 185). The qualitative difference between hard and undoped on one and

soft samples on the other side has been linked to the higher concentration of oxygen vacancies in the former samples; oxygen vacancies are associated with acceptor dopants and are known to control the mobility of domain walls (186; 187). Our measurements reveal much smaller variation between the hard, soft and undoped samples and weaker temperature dependence at 13.4 GHz than at 100 kHz. This gives further supports to the idea that the low frequency anomalies are indeed related to domain wall motion that becomes suppressed at higher frequencies.
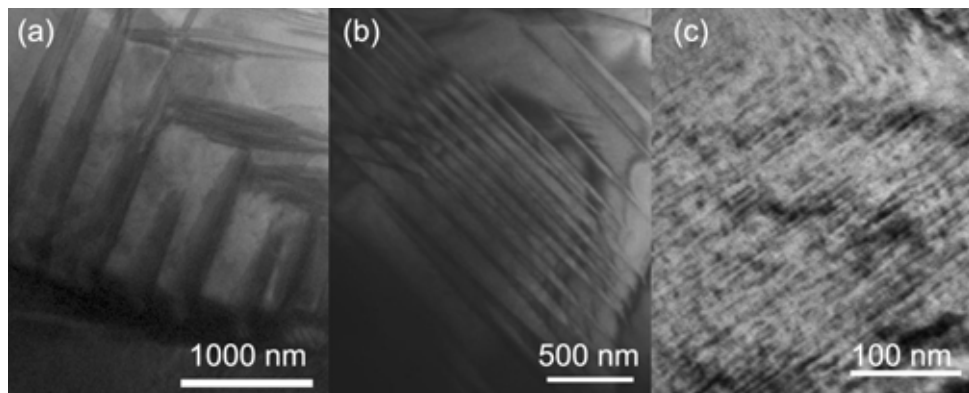


**Figure 4.12:** Permittivity $\varepsilon'$ (a), loss $\varepsilon''$ (b), and dispersion strength $\Delta\varepsilon'_{st}$ (c) versus temperature. $\Delta\varepsilon'_{st}$ represents the difference between values measured at 100 kHz (color thin lines) and 13.4 GHz (symbols). The data corresponding to a given composition are shown in the same color. The estimation based on LGD theory (50) is shown in a thick line in (a). Note the change in the vertical scale in (b).

We next compare the high frequency permittivity values with the prediction of LGD theory for polycrystalline samples (50). The latter is shown as the full line in Fig 4.12(a). At this point it is important to understand all contributions to the $\varepsilon'(13.4\,\text{GHz})$. Besides intrinsic (lattice) contribution, $\varepsilon'(13.4\,\text{GHz})$ contains contribution from the dispersion process associated with the loss above 13.4 GHz mentioned earlier. Therefore, the value of $\varepsilon'(13.4\,\text{GHz})$ can only

be regarded as the upper limit of the intrinsic contribution. Nevertheless, it shows considerably lower values compared to the theoretical prediction. A part of the discrepancy could be explained by the fact that the permittivity at 13.4 GHz should correspond to the clamped (constant strain) permittivity that is lower than the free (constant stress) permittivity calculated by the LGD (50) and shown in Fig 4.12(a). However, this difference is expected to be small in unpoled samples even if individual grains are partly piezoelectric and their electromechanical resonances contribute to microwave dispersion (see section 4.3).[4] Note that extrapolation of $\varepsilon'(100\,\text{kHz})$ and $\varepsilon'(13.4\,\text{GHz})$ to 0 K leads to a good agreement between the two, as should be expected when all extrinsic contributions are frozen. Therefore, we conclude that over a broad temperature range the LGD theory predicts higher permittivity values than observed here at 13.4 GHz. Apart from possible question about averaging procedure used to calculate LGD values reported in Ref (50), our data suggest a need for a revision of LGD analysis for compositions near MPB. Our conclusion is, therefore, that the "microwave" measurements can be used to estimate upper limit of the intrinsic contributions and are at present more reliable than theoretically derived values for MPB compositions.

At microwave frequencies the loss $\varepsilon''$ monotonously increases with increasing temperature, Fig 4.12(b), and is at least five times as high as $\varepsilon''$ probed at 100 kHz. Such behavior of loss is consistent with the temperature dependence of $\Delta\varepsilon'_{\text{st}}$ depicted in Fig 4.12(c). The multifold decrease of $\Delta\varepsilon'_{\text{st}}$ towards low temperatures seen in Fig 4.12(c) is also revealed by BSPT (155) and KNN (156). The temperature dependence of $\Delta\varepsilon'_{\text{st}}$ reflects freezing of extrinsic contributions at low temperatures further validating our procedure of estimation of extrinsic contributions. Their contributions to the permittivity are estimated according to $\Delta\varepsilon'_{\text{st}}/\varepsilon'(100\,\text{kHz})\times 100\%$. For all studied samples, the extrinsic contribution makes up over 50% of the quasi-static dielectric permittivity $\varepsilon'(100\,\text{kHz})$.



**Figure 4.13:** Room temperature bright field TEM image of (a) PZT(52/48), (b) PZT(52/48)Nb1.0, and (c) PZT(52/48)Fe1.0 ceramics.

As domain wall motion is intimately related to the steep dispersion in ferroelectrics (146;

---

[4]The clamped $\varepsilon^S$ and free $\varepsilon^T$ permittivity is related by electromechanical coefficient $k$ through Eq. 1.5, i.e., $\varepsilon^S = \varepsilon^T(1-k^2)$. In unpoled state, the $k$ is almost close to zero. In this case, the difference between the clamped and free permittivity is very small.

148; 144), an examination of domain morphology is of interest here. The TEM images presented in Fig 4.13 provide such an opportunity. The representative domain patterns shown here clearly demonstrate progressive decrease of domain size as we move from PZT(52/48) through PZT(52/48)Nb1.0 to PZT(52/48)Fe1.0. Rough estimation of domain sizes along with the grain size $\overline{D}$ is summarized in Table I, where $\overline{D}$ is extracted from SEM images. As it was already pointed out, very strong reduction of domain size observed in PZT(52/48)Fe1.0 cannot be accounted by the variation of the grain size alone, where a square root of dependence $\sim \sqrt{\overline{D}}$ is usually expected (119; 65). It is worth noting that the increase of the domain wall density does not lead to any enhancement of extrinsic response, as recently suggested for MPB compositions (42) of PZT and reported for piezoelectric properties of $BaTiO_3$ (188); other factors besides domain wall density must be taken into account. In addition, it appears that the domain wall density by itself has no impact whatsoever on dielectric properties above 13.4 GHz. The only enhancement of extrinsic contribution we observe in addition to microwave dispersion is due to the nearly constant loss behavior in PZT(52/48)Nb1.0. In PZT(52/48)Fe1.0, this polarization mechanism is most likely suppressed by the pinning centers associated with $Fe^{3+}$-ions (77). As for the positive role of $Nb^{5+}$-ions, one option could be higher domain wall mobility promoted by the presence of $Nb^{5+}$-ions and associated defects disorder (189). Interestingly, within resolution of our measurements, the dopants do not seem to affect the polarization response above the region of steep dispersion.

**Table 4.3:** Average grain size and domain size of studied PZT samples.

| Composition | grain size ($\mu$m) | domain size (nm) |
|---|---|---|
| PZT(52/48) | 7.92 | 100~1000 |
| PZT(52/48)Nb1.0 | 2.91 | 20~300 |
| PZT(52/48)Fe1.0 | 2.05 | ~10 |

# 4.5   Summary

- Much higher loss intensity found around $f_u$ compared to the intensity of loss peak around $f_p$ clearly demonstrates that the piezoelectric resonance of grains cannot be considered as the main mechanism responsible for strong microwave dispersion observed in ferroelectrics. On the other hand, due to the fact that loss associated with grain resonance dominates the loss in poled state, it can play the role of a frequency limiting factor for application sensitive to energy loss in piezoceramics.

- The temperature dependencies of the loss peak frequency in the poled state $f_p(T)$ and sound velocity $V_s(T)$ are consistent with the idea that the loss peak around fp is caused by the piezoelectric resonance of individual grains. The comparison of sound velocities in Eqs. 4.13 and 4.5 with mutual position of corresponding loss peaks $f_p$, $f_u$ suggests that Arlt's model significantly underestimates $f_u$.

- The permittivity probed in the microwave range [in our case $\varepsilon'(13.4\,\text{GHz})$] can be used to estimate the upper limit of the intrinsic dielectric permittivity in PZT ceramics. The extrinsic contribution to the permittivity $\Delta\varepsilon'_{\text{st}}$ accounts for more than 50% of the quasi-static dielectric permittivity $\varepsilon'(100\,\text{kHz})$ in all (undoped, soft and hard) studied samples. Our results also suggest that the phenomenological LGD theory with presently available free-energy coefficients overestimates intrinsic permittivity for MPB compositions.

# Chapter 5

# Lattice dynamics and dielectric dispersion in THz frequency range

In microwave frequency range (i.e., from 300 MHz to 300 GHz) ([190](#)), the corresponding wavelength of the signal is on the order of 1 m to 1 mm. Above this frequency range, other techniques are needed to characterize the dielectric response of ferroelectric ceramics, such as Raman, infrared (IR) and THz spectroscopy. In the frequency range covered by those techniques, the dielectric contributions mainly come from the crystalline lattice, which belongs to the study of lattice dynamics. At present, lattice dynamic studies on PZT ceramics are rather limited. A tentative study of the lattice dynamics and dielectric dispersion in THz frequency range will be presented in this chapter. The presented work was performed in the Institute of Physics, Academy of Sciences of the Czech Republic ([191](#)). Much attention focuses on two questions[1]:

- Raman spectra are very sensitive to structural transitions. A new low-temperature phase in the tetragonal side of the phase diagram due to the tilt of the oxygen octahedra has been suggested by first-principle calculations ([192](#)). Could such phase transition be verified experimentally by means of Raman spectra?

- By introducing the acceptor and donor dopants into PZT, obvious difference between them in dielectric response are clearly revealed up to the microwave frequency range. The difference is mainly attributed to the domain dynamics. Could those dopants result in the changes in dielectric response of crystalline lattice?

## 5.1  Introduction

The crystal structure of the lead zirconate-lead titanate solid solution is closely related to the Zr/Ti ratio. PZT on the titanate-rich side belongs to a tetragonal phase (P4$mm$ space group)

---

[1]The data presented in this chapter are partially published in the following publication: E. Buixaderas, D. Nuzhnyy, P. Vanek, I. Gregora, J. Petzelt, V. Porokhonskyy, <u>L. Jin</u>, and D. Damjanovic "Lattice dynamics and dielectric response of soft and hard PbZr$_{0.42}$Ti$_{0.58}$O$_3$," *Phase Transitions*, vol. 83, pp. 917-930 , 2010.

down to low temperatures. On the contrary, PZT on the rhombohedral side undergoes a doubling of the unit cell due to the oxygen octahedra tilting (i.e., from high temperature $R3m$ space group to low temperature $R3c$ space group), just above room temperature (2). As mention in chapter 1, the modifications to the phase diagram of PZT solid solution mainly focus on the MPB region, where a new monoclinic phase is detected at low temperature, based on x-ray and neutron diffraction measurements (33; 34; 32; 26). On further cooling a monoclinic ($Cm$) to monoclinic ($Cc$) transition occurs to an octahedrally tilted phase (193). However, such monoclinic phases are also debated since the coexistence of tetragonal and rhombohedral domains could produce similar diffraction patterns (40). Recently, Pandey *et al* suggested that the whole rhombohedral side of the phase diagram has a monoclinic symmetry (194). Based on a first principle calculations, a new low-temperature phase is also predicted in the tetragonal side of the phase diagram due to the tilt of the oxygen octahedra, although this phase has not been confirmed experimentally (192). Compared with the Raman and infrared (IR) studies of $(Pb_{1-x}La_x)(Zr_{0.4}Ti_{0.6})O_3$ (PLZT) (195; 196), where an increased number of phonons were revealed at low temperature, similar observations are expected in PZT, because of the structure similarity between PLZT and PZT.

In chapter 3, we have shown that the domain structure is drastically changed by introducing the acceptor and donor dopants into PZT solutions. In chapter 4, the difference in dielectric properties in GHz region between the hard and soft PZT ceramics is clearly revealed. However, it is believed that the intrinsic properties should be the same for the PZT samples with the same Zr/Ti ratio, because the low doping level (1% at.) is not expected to result in a large change in the crystalline lattice. For PZT ceramics, at present no attempt has been conducted to detect the dielectric properties above the GHz region. Above this region, other techniques are needed to characterize the dielectric properties of PZT, such as Raman, infrared and TH spectra. The aim of this chapter is to investigate the lattice dynamics of pure and doped tetragonal PZT ceramics and investigate the possible occurrence of the oxygen octahedra tilt at low temperatures, as well as the influence of the donor and acceptor doping on the dynamic dielectric behavior.

## 5.2 Experimental descriptions

### 5.2.1 Piezoelectric and dielectric characterization

The low temperature elastic properties of studied samples were characterized by means of impedance spectrum (177). Before the measurement, the samples in thin disk shape were poled at 50 kV/cm in silicon oil. The conductance ($G$) of studied samples as a function of frequency (from 100 kHz to 1 MHz) was swept by a HP 4194A impedance analyzer. For radial piezoelectric resonance mode, there is a maximum of the conductance near the resonance frequency ($f_s$). The relationship between the elastic constant $s_{11}^E$ and $f_s$ is related by Eq. 5.1 (197)

$$s_{11}^E(1 - \sigma^{E2}) = \frac{\eta_1^2}{\pi^2 \rho (f_s \cdot d)}, \tag{5.1}$$
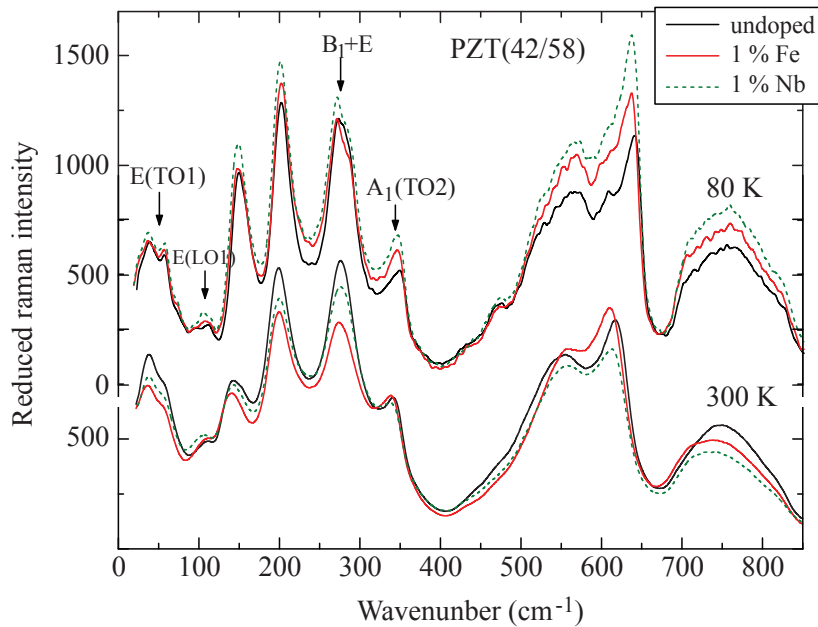
where $\sigma$ is the Poisson ratio, $\rho$ is density, $d$ is the diameter of the thin disk, and $\eta$ is the lowest positive root of $(1 + \eta^E)J_1(\eta) = \eta J_0(\eta)$, $J_0$ and $J_1$ are first kind Bessel functions of zero and first order, respectively. The resonance frequency determined from the conductance maximum as a function of temperature was recorded during cooling. For comparison, the dielectric constant of studied samples with respect to the temperature were also checked by a HP 4284A *LCR* meter. Both the piezoelectric and dielectric properties were measured from 300 to 50 K.

### 5.2.2   Raman, IR and THz spectra

The Raman, IR and THz spectra presented in this chapter were provided by Prof. Jan Petzelt's group from Institute of Physics, Academy of Sciences of the Czech Republic, Prague. The details of those experiments could be found in Ref. (191).
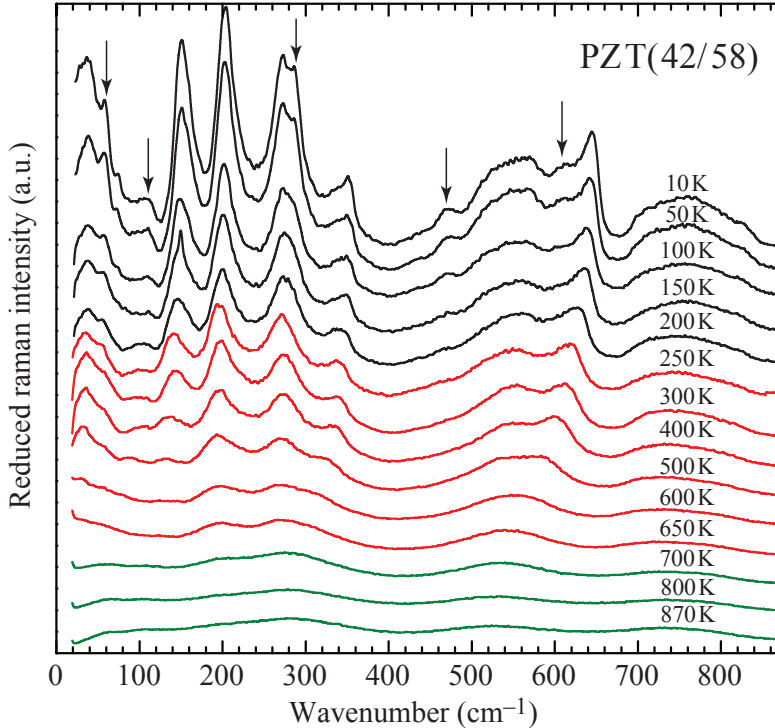
## 5.3   Results and discussion

### 5.3.1   Phase transition in tetragonal phase



**Figure 5.1:** Raman spectra of undoped, soft and hard PZT(42/58) ceramics at 300 K and 80 K. Arrows denote split peaks at low temperatures. Taken from Buixaderas *et al* (191).

The Raman spectra of undoped, soft and hard PZT(42/58) ceramics at 300 and 80 K are shown in Fig 5.1. No significant differences among the spectra appear at room temperature. On cooling, however, small differences can be observed in the splittings of the E(TO1) ($\sim$70 cm$^{-1}$), E(LO1) ($\sim$115 cm$^{-1}$) and A$_1$(TO2) ($\sim$350 cm$^{-1}$) modes and the B$_1$+E doublet ($\sim$270 cm$^{-1}$). The assignment of symmetries was taken from tetragonal PLZT (198).
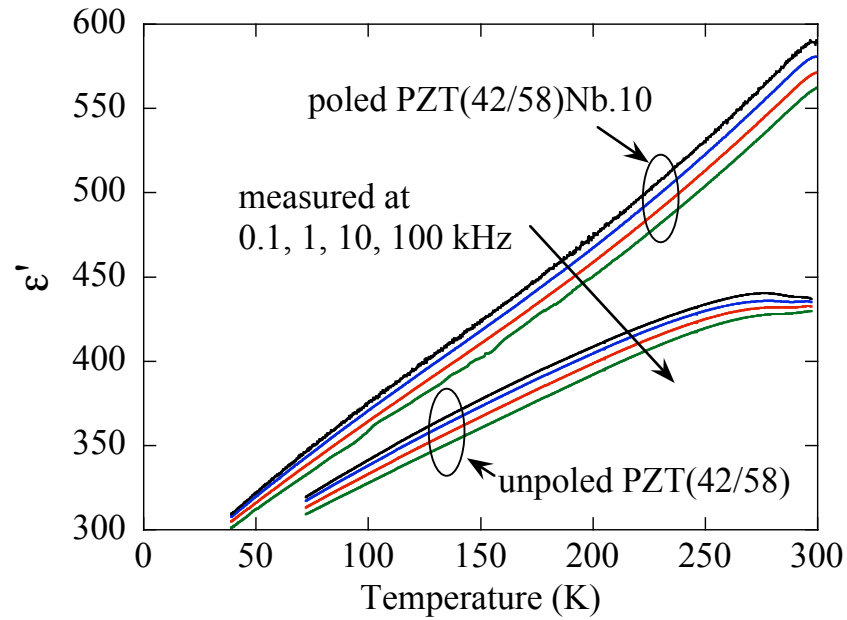
**Figure 5.2:** Temperature dependence of the Raman spectra of undoped PZT(42/58) ceramic. Arrows denote new peaks at low temperatures. Taken from Buixaderas *et al* (191).
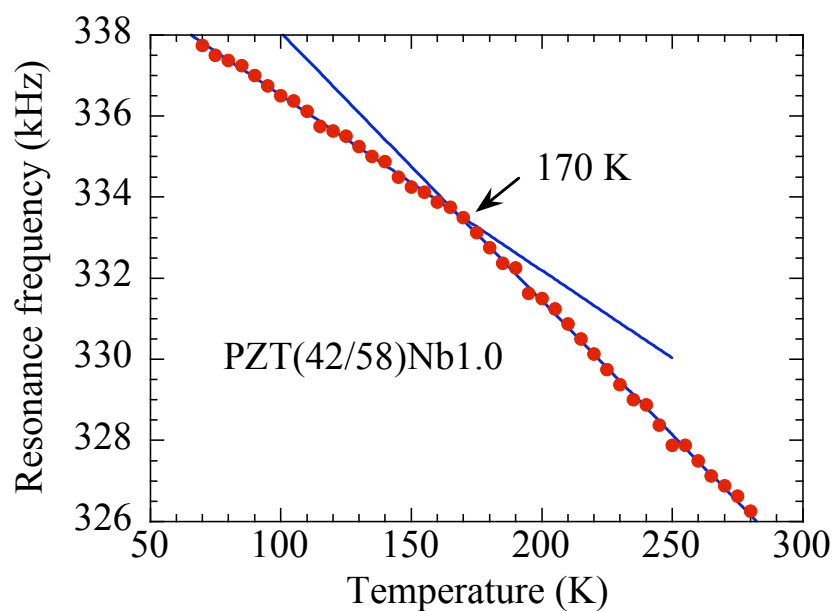
The temperature dependence of the Raman spectra of the undoped PZT(42/58) is shown in Fig 5.2. At high temperatures, in the cubic phase, Raman spectra show three broad bands, although no Raman activity is allowed in the P$m3m$ space group. The origin of these bands was discussed in tetragonal PLZT (198) and is related to off-centred cations. In the tetragonal phase, Raman spectra develop new peaks corresponding to split $A_1$+E doublets. The most intense modes are transverse, although some weak longitudinal ones are also detected. In ceramics, no direct assignments of mode symmetries are possible from the Raman measurements. Therefore, the assignment of symmetries was followed in tetragonal PLZT (198), using the effective medium approach (199). On further cooling new modes appear, which seems to signalize the appearance of a new phase (Fig 5.2).

In order to find more evidences to support the existence of such a phase transition, low-frequency dielectric response of undoped PZT(42/58) was first measured from 300 to 50 K on cooling. As shown in Fig 5.3, the permittivity $\varepsilon'$ measured at different frequencies decreases by lowering the temperature, except the abnormal response near 300 K, which is mainly due to the aging effect by the oxygen-vacancy defect dipoles (200). There is no clear evidence to suggest the existence of the phase transition below 200 K.

Since such a phase transition is related to the tilt of the oxygen octahedra, it might be detected by observing the anomalies in the elastic properties via piezoelectric technique (2). Elastic anomalies are sometimes more distinct and less ambiguous than dielectric anomalies. The latter can be caused by charge relaxation processes as well as by structural phase transitions. Furthermore elastic properties in ferroelectrics may be sensitive to structural modifi-
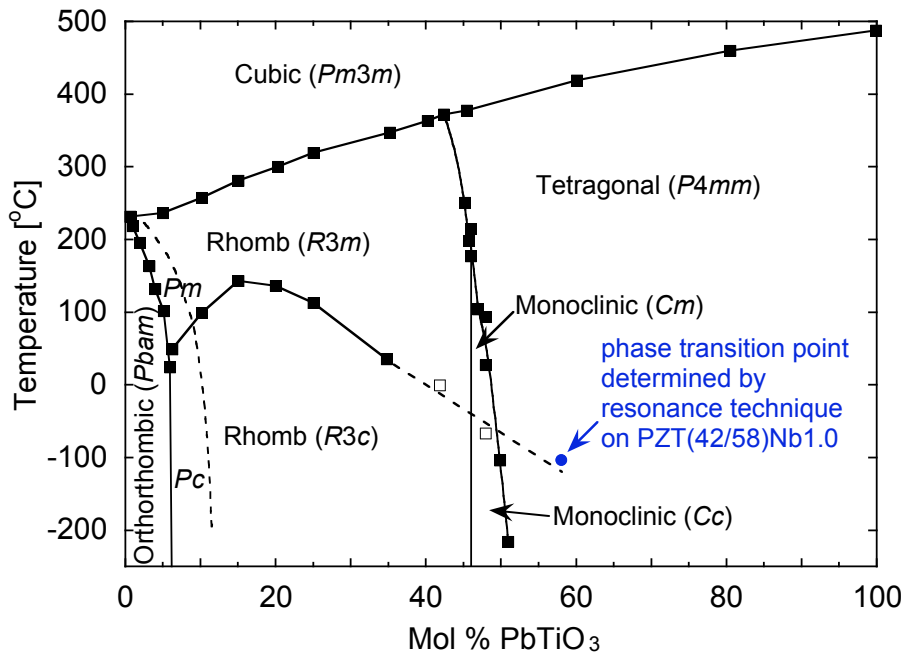
**Figure 5.3:** Temperature dependences of the permittivity $\varepsilon'$ of PZT(42/58) ceramic in unpoled state and PZT(42/58)Nb1.0 ceramic in poled state during cooling from 300 to 50 K.



**Figure 5.4:** Temperature dependences of radial mode resonance frequency $f(T)$ of PZT(42/58)Nb1.0.

cations that do not leave a clear signature in the dielectric behavior. Such is the case for the transition between the low- and high-temperature rhombohedral phases in Zr-rich PZT (23). Therefore we inspected the changes of the resonance frequency of the sample at temperatures below 300 K. For such measurements the samples need to be poled. Unfortunately, undoped PZT(42/58) and PZT(42/58)Fe1.0 could not be well poled, because of the high $c/a$ ratio. Thus PZT(42/58)Nb1.0, which could be readily poled, was used for these measurements. As shown in Fig 5.3, the permittivity $\varepsilon'$ of poled PZT(42/58)Nb1.0 measured at different frequencies decreases by decreasing the temperature. No clear evidence could be found to support the existence of a phase transition below 200 K. However, compared to the dielectric response, a clear change in the resonance frequency with respect the temperature is revealed in Fig 5.4. The resonance frequency is increased by cooling, but its slope changed at 170 K. Below and above 170 K, the $f(T)$ could be well fitted by a linear fitting. Therefore the turning point may suggest the phase transition temperature, which is very close to the temperature determined by the Raman spectra as shown in Fig 5.2.
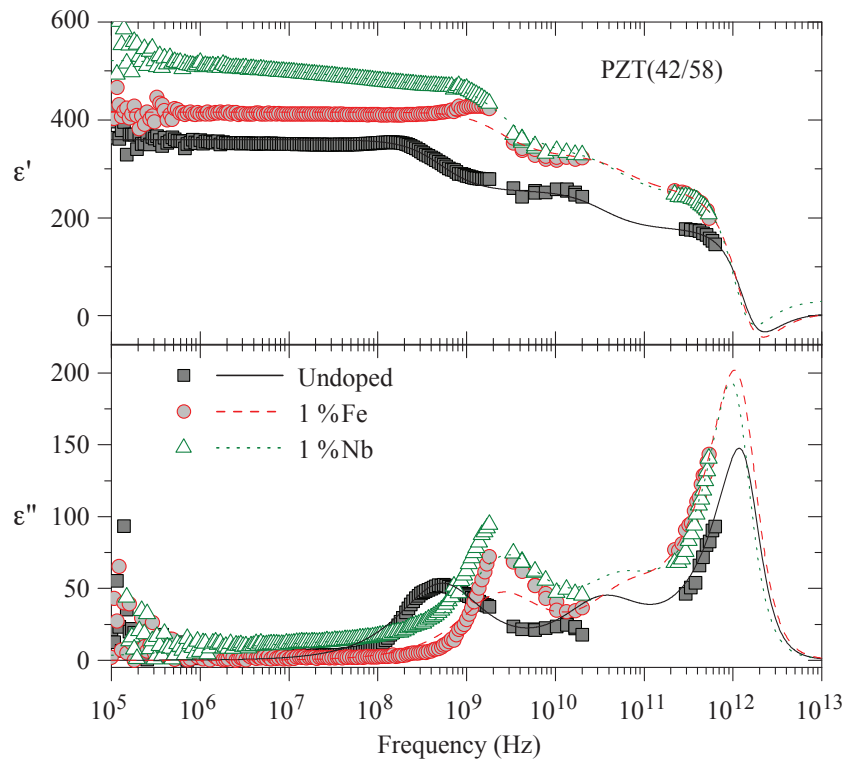


**Figure 5.5:** A self-consistent PbZrO$_3$-PbTiO$_3$ phase diagram is compiled from a number of sources to include complete space group details. Open squares indicate revised data points for the position of the $R3m$-$R3c$ transition (after Eitel and Randall (201)) and $Cm$-$Cc$ transition (after Hatch *et al* (193)) confirming the tilt boundary (dashed line) is continuous across the rhombohedral-monoclinic phase boundary. Taken from Eitel and Randall (201). The blue data point suggests the phase transition temperature, which is determined by piezoelectric resonance measurement from PZT(42/58)Nb1.0. The dashed line is extrapolated from rhombohedral region to the tetragonal region. According to the phase diagram suggested by Kornev *et al* (192) by first principle calculation, the phase at the high-Ti side below the dash line is a $I4cm$ phase.

Compared with the phase diagram of PZT determined by Jaffe *et al* (2), recent studies pay

much attention to the low temperature region. A monoclinic-monoclinic phase transition is confirmed near the MPB region due to the tilt of the oxygen octahedra. A similar phase transition related to such octahedral tilting is also reported in the rhombohedral region. Those modifications are included in Fig 5.5. The open square symbols represent those phase transition points. The dashed line is extrapolated from rhombohedral region to the tetragonal region to cover those phase transition points. It is interesting that the phase transition point determined from PZT(42/58)Nb1.0 by the piezoelectric resonance method is almost exactly on the extension of this extrapolated dashed line, which suggest that the tilts goes continuously from the rhombohedral phase through monoclinic phase to tetragonal phase. In order to confirm this conjecture, more data points in the tetragonal side are needed to be verified by means of the piezoelectric properties characterization.

### 5.3.2 Dielectric properties in THz frequency range



**Figure 5.6:** Frequency dependence of the complex dielectric permittivity $\varepsilon^*(v)$. Symbols correspond to experimental data and lines to the fits with Eq 5.2. Taken from Buixaderas *et al* (191).

Combing with the low frequency dielectric properties (from 100 kHz to 1.8 GHz), the THz frequency range dielectric properties of undoped and doped PZT(42/58) are shown in Fig 5.6. Both hard and soft dopings not only increase the permittivity values in the microwave and THz frequency range, but also increase the loss above the GHz range. The dielectric data were fitted with a sum of Cole-Cole dispersion terms (below THz) and a damped oscillator:

$$\varepsilon^*(\omega) = \varepsilon'(\omega) - i\varepsilon''(\omega) = \sum_j \frac{\Delta\varepsilon_j}{1 + (i\omega/\omega_j)^{1-\alpha_j}} + \frac{\Delta\varepsilon_{SM}\omega_{SM}^2}{\omega_{SM}^2 - \omega^2 + i\gamma_{SM}\omega} + \varepsilon_{IR}, \qquad (5.2)$$

where $\Delta\varepsilon_j$ is the dielectric strength of the Cole-Cole relaxation; $\omega_j$ its mean relaxation frequency, $\alpha_j$ a real index between 0 and 1 which determines the deviation from the Debye model and characterizes the width of the distribution of the Debye relaxation frequencies, $\Delta\varepsilon_{SM}$, $\omega_{SM}$ and $\gamma_{SM}$ the dielectric strength, frequency and damping of an effective oscillator in the THz range (including central mode (CM) and E(TO1) modes[2]), respectively, and $\varepsilon_{IR}$ the dielectric contribution of phonons with frequencies higher than 3 THz and electrons. Table 5.1 presents the results of the fit.

**Table 5.1:** Parameters of the IR modes obtained from the fit of the reflectivity and THz spectra using Eqs A.1 and A.2 at selected temperatures. $\omega$ and $\gamma$ are given in $cm^{-1}$. Taken from Buixaderas *et al* (191).

|  | undoped | | | 1% Fe | | | 1% Nb | | |
|---|---|---|---|---|---|---|---|---|---|
|  | $\omega$ | $\Delta\varepsilon$ | $\alpha, \gamma$ | $\omega$ | $\Delta\varepsilon$ | $\alpha, \gamma$ | $\omega$ | $\Delta\varepsilon$ | $\alpha, \gamma$ |
| Cole-Cole | – | – | – | – | – | – | 0.2 MHz | 66 | 0.6 |
| Debye | 0.5 GHz | 100 | 0 | 2.4 GHz | 84 | 0 | 2.7 GHz | 128 | 0 |
|  | 34 GHz | 80 | 0 | 55 GHz | 70 | 0 | 52 GHz | 82 | 0 |
| Oscilator | 1.5 THz | 150 | 2 THz | 1.4 THz | 226 | 2 THz | 1.2 THz | 218 | 1.5 THz |
| $\varepsilon_{IR}$ | 32 | | | 32 | | | 32 | | |

Below phonon frequencies, several mechanisms appear: a soft central mode located near 1 THz and two Debye relaxations in the GHz range. Both types of doping increase the permittivity values below phonon frequencies, not only increasing the dielectric contribution of central mode, but also modifying the dielectric response near the GHz range, where domain walls and piezoelectric resonances in the grains contribute. Soft ceramics show higher permittivity values and no saturation of permittivity at low frequencies, which was fitted by a Cole-Cole relaxation with a broad distribution of relaxation times ($\alpha =0.6$).

From parameters in Table 5.1, it is seen that doping slightly lowers the frequency of the effective THz oscillator (more in the case of the soft ceramics, from 1.5 to 1.2 THz) and increases its contribution to the permittivity (from 150 to more than 200). This observation suggests that doping results in changes in the dielectric properties at least up to THz frequency range.

As shown in Table 5.1, two Debye relaxations are obtained to fitting the broad dielectric properties. Besides the low frequency Debye relaxation (between 0.1 and 10 GHz), another high frequency Debye relaxation, which is revealed by the fitting instead of experimental characterization, is observed at 34 GHz for PZT(42/58), and at 55 GHz and 52 GHz for PZT(42/58)Fe1.0 and PZT(42/58)Nb1.0, respectively. As has been discussed in chapter 4,

---

[2]In the tetragonal phase below $T_C$, two excitations: the CM ($v \sim 20\,cm^{-1}$) and the E(TO1) modes ($v \sim 60\,cm^{-1}$), are resolved by IR and Raman spectra. The CM clearly hardens, and the E(TO1) mode frequency remains practically constant down to room temperature. On further cooling, the E(TO1) mode splits: a component near $80\,cm^{-1}$ and a new mode at almost $90\,cm^{-1}$ appear.

the relaxation frequency (or dispersion frequency) is normally related to the domain size. By means of doping, the domain size of both hard and soft samples is decreased. Therefore, higher relaxation frequencies would be expected in doped samples. For the low frequency Debye relaxation, such a relationship is proved by the higher relaxation frequency in hard (2.4 GHz) and soft (2.7 GHz) samples compared with undoped one (0.5 GHz). For the high frequency Debye relaxation, even though no direct experimental observations could be conducted, a similar trend in hard and soft samples revealed by the fitting suggests that this relaxation is also probably related to the domain walls. Compared with undoped sample, the $\Delta\varepsilon$ of both Debye relaxations are decreased in hard and increased in soft samples. These observations are consistent with the previous reports on the low-frequency dielectric properties of hard and soft PZT ceramics.

The larger effect in soft materials is accompanied by the broad Cole-Cole relaxation, responsible for the logarithmic increase of the permittivity and the frequency-independent losses in soft samples. The origin of this broad, low frequency dielectric dispersion in soft materials and its absence in hard ones will be discussed in terms of domain wall motion in chapter 6.

## 5.4   Summary

- The temperature dependence of the Raman spectra of undoped PZT(42/58) ceramic suggest a phase transition below 200 K, which is attributed to the tilt of the oxygen octahedra, as has been indentified in the rhombohedral and MPB regions. Temperature dependence of the resonance frequency, which is determined by means of piezoelectric resonance technique, indentifies this phase transition temperature at 170 K. This observation is consistent with previous conjecture that the tilt of the oxygen octahedron goes continuously from the rhombohedral phase through monoclinic phase to tetragonal phase.

- The dielectric properties of doped samples at THz range show a lower oscillating frequency compared with undoped sample, but the contributions to the permittivity are increased in those two samples. Fitting reveals another Debye relaxation between the GHz and THz range. The influences by the dopants on the relaxation frequency and relaxation strength $\Delta\varepsilon$ of this high frequency Debye relaxation are similar to the low frequency Debye relaxation. This suggests that they might be ascribed to the same origin (i.e., domain wall motion) but with different characteristic size.

# Chapter 6

# Broad logarithmic dielectric dispersion in Pb(Zr,Ti)O$_3$ ceramics

In the previous chapters, we have shown that the difference in dielectric properties between the soft and hard PZT ceramics above the main microwave dielectric dispersion is very small. In this chapter, the dielectric properties of soft and hard PZT ceramics are studied in a broad frequency range from $10^{-2}$ to $2 \times 10^{10}$ Hz, where the main contributions to the dielectric and piezoelectric properties by domain wall motion could be detected. Besides the microwave dielectric dispersion, another dielectric dispersion characterized by a logarithmic decrease of permittivity with increasing frequency, which spreads in a relatively broad frequency region (at least 8 decades), will be discussed as a key to understand the softening and hardening effects. The following issues concerning the logarithmic dielectric dispersion will be emphasized[1]:

- What are the dielectric properties of the soft and hard PZT ceramics below GHz? What is the origin of those dielectric responses?

- In both soft and hard PZT ceramics, a broad logarithmic dielectric dispersion could be observed. What is the difference of the dielectric response between the soft and hard samples?

- There is a drastic increase of both the permittivity $\varepsilon'$ and loss $\varepsilon''$ at low frequency in hard PZT ceramics. Can such an increase be attributed to the domain wall motion or charge migration (such as hopping)?

---

[1]The data presented in this chapter are mainly adopted from the manuscript: L. Jin, V. Porokhonskyy, and D. Damjanovic, "Broad logarithmic dielectric dispersion in Pb(Zr,Ti)O$_3$ ceramics: The influence of the crystalline symmetry and doping on the disorder," to be submitted.

## 6.1 Introduction

The main contributions to the ac dielectric permittivity $\varepsilon'$ of ferroelectric materials originate from the crystalline lattice (intrinsic) and domain wall motion (extrinsic) [8; 9]. The intrinsic dielectric properties include the polar phonon and electron contributions, which are observed in the infrared (IR) frequency, and visible and ultraviolet range [202]. Domain wall motion contributes to the $\varepsilon'$ at a lower frequency region, usually below hundreds of GHz, due to their larger characteristic size compared with polar phonons and electrons. Domain walls always couple with crystalline defects or imperfections, which are present even in high purity materials [9]. Their contributions to the $\varepsilon'$ is divided into several parts associated with different mechanisms. When the probing frequency is decreased from IR range, the first pronounced dielectric dispersion, which manifests itself by a strong, steplike dispersion of the $\varepsilon'$ accompanied by the a peak of $\varepsilon''$, is usually observed in the frequency range from 0.1 to 10 GHz (usually called the GHz region) [152; 146; 148; 144]. The piezoelectric grain resonance was separated from this dispersion (see chapter 4) and the main contribution to this microwave dielectric dispersion can be ascribed to the reversible domain wall motion, which is different between hard and soft materials because of the difference in their domain wall potential energy [87; 189; 203]. A domain wall in a hard material moves in a V-potential as suggested by Robels and Arlt [74], while energy of a domain wall in a soft materials is best described by a *random* potential [204]. Note that not all relaxations of the domain wall could be observed in this frequency window, since the relaxation frequency $f_R$ (normally determined by the frequency corresponding to the loss peak) generally varies inversely as the domain size. For example, a relaxation is observed below 1 MHz in periodically poled KTiOPO$_4$ (PPKTP) single crystal [205], where larger artificial domains with the size of 4.5 μm were fabricated. In relaxor ferroelectric (Pb$_{1-x}$Nb$_x$)(Zr$_y$Ti$_{1-y}$)$_{1-x/4}$O$_3$ (PLZT) ceramics, nanometer-scale polar nanoregions (PNR) or nanoclusters, instead of domain walls, respond to the external ac driving field, and shift the relaxation out of the GHz frequency window [202].

The microwave dielectric dispersion is often modeled by a Debye- or polydispersive Debye relaxation equation [182; 206]

$$\varepsilon^* = \frac{\Delta\varepsilon_m}{1+(i\omega\tau)^\alpha}, \qquad (6.1)$$

where $\varepsilon^*$ is the complex permittivity, $\Delta\varepsilon_m$ the relaxation amplitude, $\tau$ the relaxation time constant, $\omega = 2\pi f$ the angular frequency with $0 < \alpha < 1$. According to Eq. 6.1, $\varepsilon'$ approaches to a saturated value when $f \ll f_R$. This expression, however, contradicts with the experimental evidences. Except in BaTiO$_3$ [144], where a typical Deybe relaxation was reported in the GHz frequency region, other ferroelectric materials, such as, PPKTP [205], Sr$_{0.61-x}$Ce$_x$Ba$_{0.39}$Nb$_2$O$_6$ [207], isotopically modified SrTi$^{18}$O$_3$ [208], PLZT [202], Pb(Fe$_{1/2}$Nb$_{1/2}$)O$_3$ [209], Rb$_2$ZnCl$_4$ [210], and RbH$_2$PO$_4$ [211], show an obvious increase of $\varepsilon'$ by lowering the frequency below $f_R$, while $\varepsilon''$ also displays a polydispersive response without obvious loss peak. This kind of dielectric dispersion is generally termed the "non-Debye" response, in order to distinguish it from the Debye relaxation. This dispersion originates from domain wall motion along a certain direction

with a net dislocation. Different terminologies were used to indicate this non-Debye domain wall motion, such as "creep" or "slide" (9; 205; 212). The creep corresponds to hoping of domain walls between two potential minima with a broad distribution of potential barriers between them. This is analogous to variable range hopping of charge carriers (213). Nattermann *et al* (214) proposed that in ferroics with quenched disorder, the creep of domain wall motion contributes to permittivity $\varepsilon^*$ as given in Eq. 6.2:

$$\varepsilon^* \propto \frac{\ln(1/\omega\tau_0)^\Theta}{1+i\omega\tau}, \tag{6.2}$$

where $\tau$ is microscopic relaxation time and $\tau < \tau_0$, and $\Theta$ is roughness exponent, which is $\approx 0.83$ in three-dimensions. As the probing frequency is increased from a very low value (i.e., $f \ll 1/\tau$), this law predicts a nearly linear decrease of $\varepsilon'$ with respect to $\log(f)$, and a linear increase of $\log(\varepsilon'')$ with $\log(f)$. Kleemann *et al* (207) named this behavior as $\log(f)$ law and believed that this phenomena was a rare event. At present, it is comfirmed only in $KH_2PO_4$ after subtracting the contributions by several Debye components (215). On the other side, Rychetsky *et al* (202) reported another non-Debye dispersion in relaxor ferroelectric PLZT, which manifests itself by a good linear decrease $\varepsilon'$ and a nearly constant loss $\varepsilon'$ with respect to increasing the frequency in a broad frequency range. Here, we define such a linear decrease relation of $\varepsilon'$ with $\log(f)$ as *logarithmic dispersion*, and will use this term through this chapter. Eq. 6.3 can be used to fit such a logarithmic dispersion,

$$\varepsilon'(f) = \varepsilon'_a - \alpha\log(f). \tag{6.3}$$

where $\varepsilon'_a$ is a constant and $\alpha$ is the slope of such a logarithmic dispersion. Compared with Eqs 6.2 and 6.3, it can be seen that there is no difference in $\varepsilon'$. The difference between them mainly comes from response of $\varepsilon''$ to the frequency, i.e., whether the $\varepsilon''$ is dependent or independent with the frequency. We notice that such dispersions were reported in "disordered" systems. In some ionic conductors (216; 217; 218) and highly disordered dielectrics including polymers (219; 220), dipolar glasses (221) and relaxor ferroelectics (202; 222), the nearly constant loss (NCL) behavior is universally observed, although the origion of this NCL is still not well understood (223; 224). In addition, a constant loss is expected according to the Kramers-Kronig relation if the response of the $\varepsilon'$ can be described by Eq. 6.3. Therefore, a $\log(f)$ law with a NCL behavior of the dielectric dispersion seems to be a common phenomena in the disordered ferroelectrics.

The definition of "disorder" in ferroelectrics is not clear. It often refers to nanodomains (206; 207), polar nanoregions (202), or polar nanoclusters (225). In brief, the disorder is frequently used to indicate the domain state. As presented in chapter 3, a random distribution of nanodomains with the size of tens of nanometers is observed in a hard PZT ceramic with composition at MPB. However, its $\varepsilon'$ shows a nearly constant permittivity with respect to frequency below several hundreds MHz. On the contrary, the logarithmic dispersion is observed in soft donor-doped PZT, where large domains are observed. The difference between those two materials mainly stems from the dipolar defects. In hard PZT it is well accepted that $(Fe'_{Ti,Zr} - V_O^{\bullet\bullet})^\bullet$
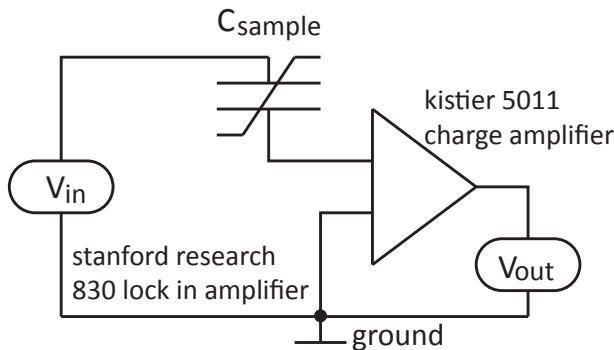
defect dipoles in a well-aged state distribute in an ordered fashion ([72]; [73]; [226]; [77]; [80]; [85]; [3]). Those defect dipoles couple with domain walls and polarization and pin (or immobilize) the motion of domain wall. In soft PZT, however, there is no evidence to suggest an ordered distribution of the $(\mathrm{Nb}^{\bullet}_{\mathrm{Ti,Zr}} - \mathrm{V}''_{\mathrm{Pb}})'$ defect dipoles.

In this chapter we show that classic ferroelectric PZT could also behave as a disordered system by introducing the disordered defect dipoles as in soft PZT, even though without random nanodomains. The soft PZT due to its supposed random distributions of the dipolar defects is a good candidate to test the non-Debye logarithmic dispersion as described by Eq. 6.3. Except the doping kind, the phase symmetry also influences the dielectric response of PZT. By means of the broadband dielectric spectra, we study the dielectric properties of soft and hard PZT with rhombohedral and tetragonal symmetry from 10 mHz to 20.2 GHz. A logarithmic dispersion, as described by Eq. 6.3, is verified over at least 8 decades below the $f_R$ in soft PZT with rhombohedral symmetry.

Four types of samples are needed due to the combinations of the doping kind and crystalline symmetry. According to the doping kind, they are divided into soft and hard groups. According to the crystalline symmetry, they are also divided into rhombohedral and tetragonal groups. These classifications will facilitate our discussion below.

## 6.2 Experimental descriptions

### 6.2.1 Dielectric characterizations



**Figure 6.1:** Schematic drawing of a electrical circuit for measurement of the dielectric permittivity and loss at low frequency (from 1 mHz to 10 kHz).

Thin disks samples (8 mm in diameter and 0.6 mm in thickness) were used for the dielectric characterization from 10 mHz to 1 MHz. In order to decrease the influence of space charge on the dielectric characterization at low frequency, silver paste was painted on the main surface and sintered at 800 °C as the electrodes. As shown in Fig 6.1, to determine the effective permittivity from 10 mHz to 100 Hz, a periodic low voltage signal generating the electric field with an amplitude $E_0$ was applied to electroded samples and the resulting charge response $Q$

was measured using a charge amplifier (Kistler 5011). $E_0$ was on the order of 1 V/mm. The output signal of the charge amplifier was analyzed with a lock-in amplifier (Stanford Research SR830), which also served as the voltage source. $\varepsilon^*(\omega)$ was calculated from Eq. 6.4:

$$J = \frac{I}{A} = i\omega\varepsilon_0\tilde{\varepsilon}(\omega)E(\omega) = i\omega\varepsilon_0\left\{\varepsilon'(\omega) - i\left[\varepsilon''(\omega) + \frac{\sigma_0}{\varepsilon_0\omega}\right]\right\}E(\omega), \qquad (6.4)$$

where $I$ is the total measured current, $A$ is the sample surface area, $\sigma_0$ is the dc conductivity, $E(\omega) = E_0\exp(i\omega t)$ is the electric field across the sample, $\varepsilon_0$ is the permittivity of vacuum, $\tilde{\varepsilon}(\omega)$ is the effective (measured) relative dielectric permittivity, and $\varepsilon^* = \varepsilon' - i\varepsilon''$ is the complex relative dielectric permittivity[2]. Here $I = \partial Q(\omega)/\partial t$ and $\tilde{\varepsilon}(\omega) = Q(\omega)/(\varepsilon_0 E_0 A)$. With $Q(\omega) = Q_0(\omega)\exp[i(\omega t - \delta)]$, where $\delta$ is the frequency dependent phase angle between the charge and the field, it follows that

$$\tilde{\varepsilon}'(\omega) = \frac{Q_0(\omega)\cos\delta(\omega)}{\varepsilon_0 E_0 A}, \qquad (6.5)$$

and

$$\tilde{\varepsilon}''(\omega) = \frac{Q_0(\omega)\sin\delta(\omega)}{\varepsilon_0 E_0 A}. \qquad (6.6)$$

From 100 Hz to 1 MHz, a HP 4284 *LCR* meter was used to measure the capacitance $C_p$ and loss tangent $D$ as a function of frequency. They were transfered into the $\varepsilon'$ and $\varepsilon''$ based on a parallel plate capacitance model through $\varepsilon' = C_p d/\varepsilon_0 A$ and $\varepsilon'' = \varepsilon' D$.

For the dielectric characterization of the properties from 1 MHz to 20 GHz, see the experimental descriptions in chapter 4.
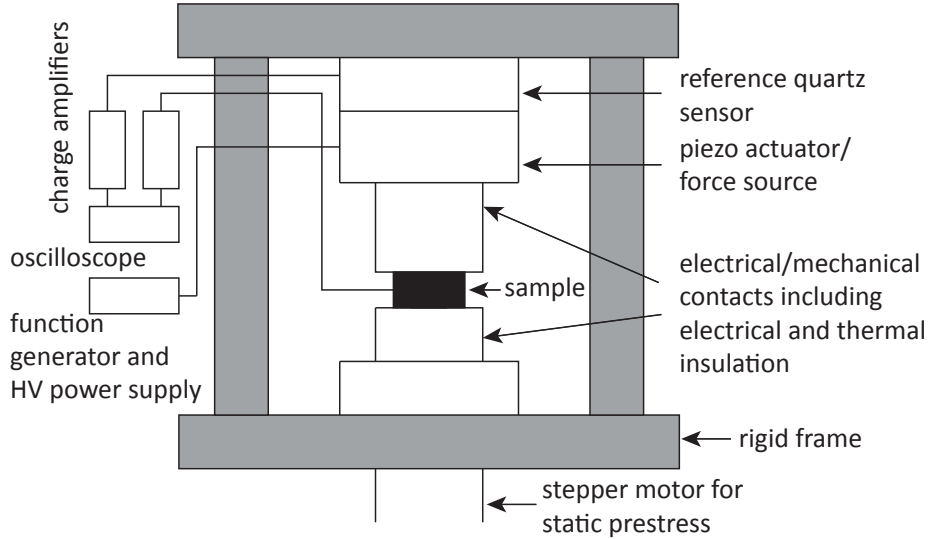
## 6.2.2 Piezoelectric characterization

For frequency-dependent piezoelectric characterization, PZT ceramic samples were in shape of a rectangular prism, with dimensions $4\times4\times2$ mm. All samples were electroded by silver paste over the largest surfaces of the samples. The poling field was applied along the thickness of the samples. PZT samples were poled to saturation with an electric field of 20 kV/cm which was applied for 30 min at 120 °C. Before the measurement, all studied samples were kept for 1 week at room temperature in order to completely age samples and avoid the aging during measurements, especially in the hard PZT.

The apparent longitudinal piezoelectric charge coefficient $d_{33}$ of the ceramics was measured by means of the Berlincourt method (227). As shown in Fig 6.2, an ac pressure, $X = X_0\sin(\omega t)$, where $\omega$ is the angular frequency and $t$ is the time, was applied to the samples. The applied pressure was measured via a reference quartz sensor that was placed mechanically in series with the sample and the source of the alternating force. The piezoelectrically induced charge density is expressed as $Q = Q_0 f(\omega t)$, where $f(\omega t)$ is a periodic function of time and $Q_0$ is

---

[2]For simplicity, we shall interchange terms permittivity and relative permittivity. The effective permittivity is introduced since the measuring instruments cannot discriminate between the true dielectric response, which does not contain $\sigma_0$, and the effective (measured) response that does. Note that besides the "true" polarization mechanisms, $\varepsilon^*$ includes contributions from any ac motion of charges, such as hopping conductivity (219; 213).
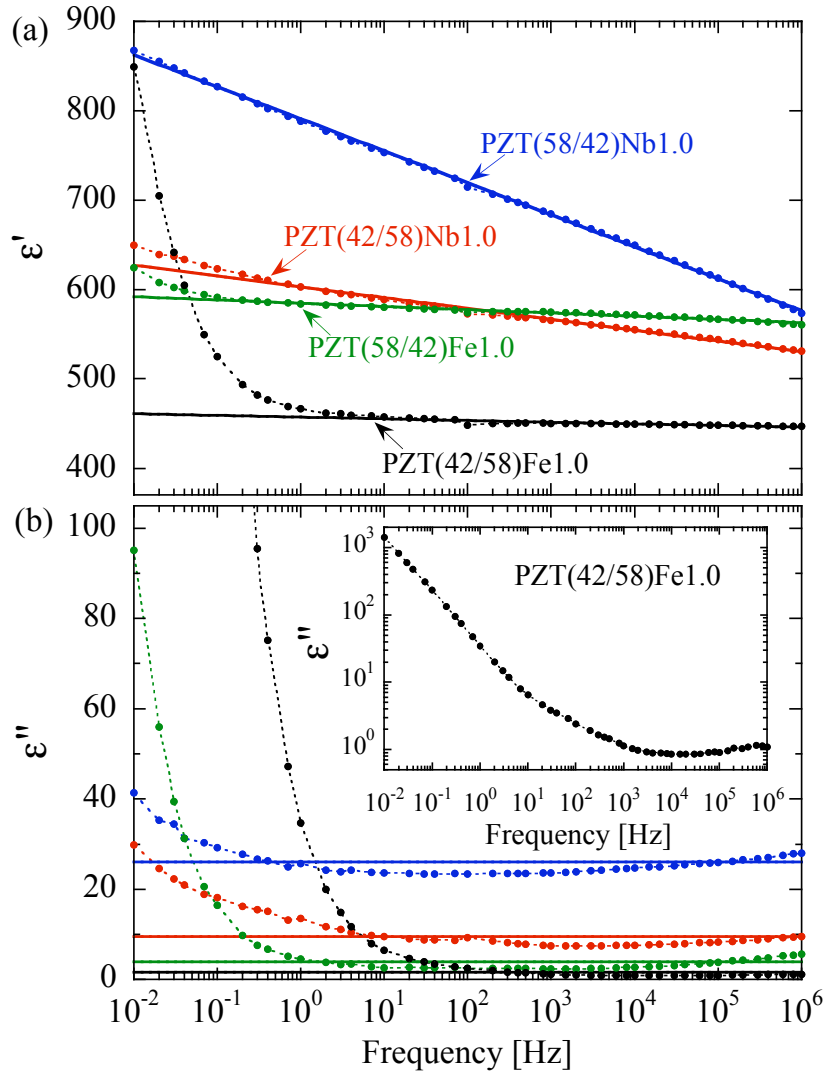
**Figure 6.2:** Schematic drawing of the Berlincourt–type $d_{33}$ meter used for the measurements.

the absolute amplitude of the charge. The piezoelectrically induced charges from the sample and the reference sensor were converted into voltage via charge amplifiers and the resulting waveforms were analyzed with an oscilloscope. Therefore the piezoelectric coefficient was calculated as $d_{33} = Q_0/X_0$. All measurements were made under d.c. pressure of 8 MPa to ensure a good transfer of force between the source, the sample and the reference sensor. The accuracy of the measurements of $d_{33}$ is better than 0.5 pC/N. The phase angle between the two waveforms was determined with an accuracy better than 0.005 rad. The frequency dependence of the piezoelectric coefficient from 10 mHz to 100 Hz was examined under a fixed a.c. pressure of 2 MPa.

## 6.3    Results and discussions

Fig. 6.3 shows the $\varepsilon'$ and $\varepsilon''$ spectra of studied PZT samples from 10 mHz to 1 MHz at room temperature. As shown in Fig. 6.3(a), the main feature between $\varepsilon'$ and $\log(f)$ of all studied samples is the linear relationship. The difference is the slope between $\varepsilon'$ and $\log(f)$, which is reflected by the $\alpha$ in Eq. 6.3. A larger $\alpha$ suggests a large increase of the $\varepsilon'$ by lowering the frequency in an order of magnitude, and reflects a high domain wall mobility, as suggested by Damjanovic (228). In principle, only in the disordered system (soft PZT), the logarithmic dispersion would be expected. Fig. 6.3(a), however, suggests some degree of disorder even in well-aged, hard samples. Thus we fit $\varepsilon'$ of all samples using Eq. 6.3. The solid straight lines represent the fitting results and fitting parameters are summarized in Table 6.1. As reflected by the linear correction coefficient $R$, the fitting is better in the soft group than in the hard group. Among all the sample, the $\varepsilon'$ of PZT(58/42)Nb1.0 shows a good fitting over 8 decades of frequency. For the other three samples, similar logarithmic dispersions with different $\alpha$ are observed. Note that in PZT(42/58)Fe1.0, its nearly constant permittivity corresponds to the

smallest $\alpha$, although the small and positive value suggests that there is still a small increase of the $\varepsilon'$ as the frequency decreases. In the low frequency side, however, there are deviations from the logarithmic dispersion as indicated by the fitting, which is especially obvious in PZT(42/58)Fe1.0. Those deviations can be ascribed to the oxygen vacancy hopping for hard group and electronic conduction for soft group (4), and will be identified by the piezoelectric response discussed below.
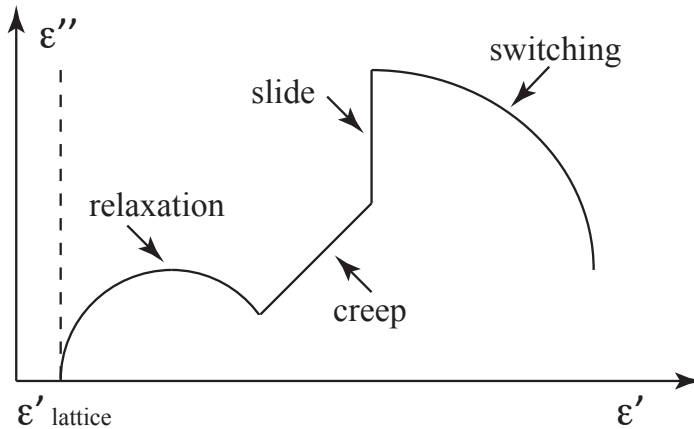


**Figure 6.3:** Permittivity $\varepsilon'$ (a) and loss $\varepsilon''$ (b) spectra of PZT samples at room temperature from 10 mHz to 1 MHz. The inset of (b) is the loss of PZT(42/58)Fe1.0. The solid lines in (a) are the logarithmic fittings based on Eq 6.3 and the solid lines in (b) are the fittings based on nearly constant loss behavior. The dash lines are a guide to the eye. For a given composition, both $\varepsilon'$ and $\varepsilon''$ share the same color.

For the corresponding $\varepsilon''$, the data at high frequency side show nearly constant loss behavior. We performed the fitting based on constant loss behaviors, i.e., $\varepsilon''(f) = \varepsilon''_{\text{constant}}$. The fitting range for every sample is the same as fitting of $\varepsilon'$ given in Table 6.1. As shown in Fig. 6.3(b), such fitting describes the data well. However, the drastic deviation from the fitting at low frequency side is also obvious.

**Table 6.1:** Fitting parameters of $\varepsilon'$ based on Eq. 6.3 and $\varepsilon''$ of the data shown in Fig 6.3. $R$ is the linear correlation coefficient of the fitting for $\varepsilon'$.

| Sample | $\varepsilon'_a$ | $\alpha$ | $R$ | Fitting range | $\varepsilon''_{constant}$ |
|---|---|---|---|---|---|
| PZT(58/42)Nb1.0 | 790 | 35.7 | 0.99 | $10^{-2} - 10^6$ Hz | 26 |
| PZT(42/58)Nb1.0 | 600 | 12.1 | 0.99 | $10^{-1} - 10^6$ Hz | 9.5 |
| PZT(58/42)Fe1.0 | 580 | 3.6 | 0.98 | $10^{-1} - 10^6$ Hz | 3.9 |
| PZT(42/58)Fe1.0 | 460 | 1.9 | 0.96 | $10^1 - 10^6$ Hz | 1.6 |

As summarized in Table 6.1, both the doping type and crystalline symmetry influence the value of $\alpha$. The soft group possesses larger $\alpha$ than the hard group. This could be explained by the weak pinning effect by the disordered defect dipoles. Due to the absence of the pinning centers in soft PZT, high mobility of domain walls is expected. The high domain wall mobility is reflected by the large value of $\alpha$. On the contrary, domain walls in hard materials cannot move readily because of the strong pinning effect caused by the ordered defect dipoles. In addition, in both soft and hard groups, the $\alpha$ in rhombohedral phase is larger than in tetragonal phase. One reason for this could be that there are eight directions in rhombohedral phase for the domain movement, instead of six directions in tetragonal phase (61). Furthermore, it could be that tetragonal phase has a large spontaneous strain and polarization, and that both make local domain wall switching more difficult in tetragonal phase than in rhombohedral phase (2). Therefore higher mobility of the domain wall, which is related to a high value of $\alpha$, is expected in rhombohedral phase.
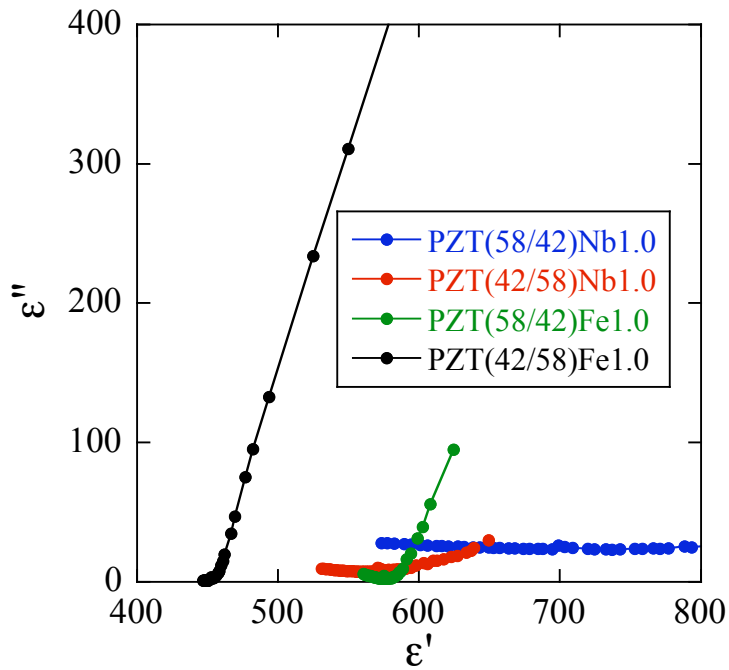


**Figure 6.4:** Schematic Cole-Cole plot, $\varepsilon'$ versus $\varepsilon''$, for a randomly pinned ferroic domain wall in ac driving fields, exhibiting segmental relaxation, creep, slide, and switching. The lattice contribution to the $\varepsilon'$ is denoted as $\varepsilon'_{lattice}$. The lattice contribution to the $\varepsilon''$ is neglected. Taken from Kleemann *et al* (206).

In Fig. 6.3(b), the characteristic response of $\varepsilon''$ to the frequency is divided into two regions. At the high frequency side (above 10 Hz), a NCL behavior is observed in all studied samples.

Soft group possesses larger $\varepsilon''$ than the hard group consistent with a higher domain wall mobility. While at the low frequency side (below 10 Hz), a steep increase of $\varepsilon''$ becomes obvious, especially in the hard group. As suggested in Ref. (4), this steep increase is mainly due to the conductive properties of the sample. Note that the conductivity in tetragonal phase is more obvious than in rhombohedral phase for both hard and soft groups. However, the origin of this phenomenon is still unknown. Without the conductivity, the NCL is expected in the whole frequency range from 10 mHz to 1 MHz.
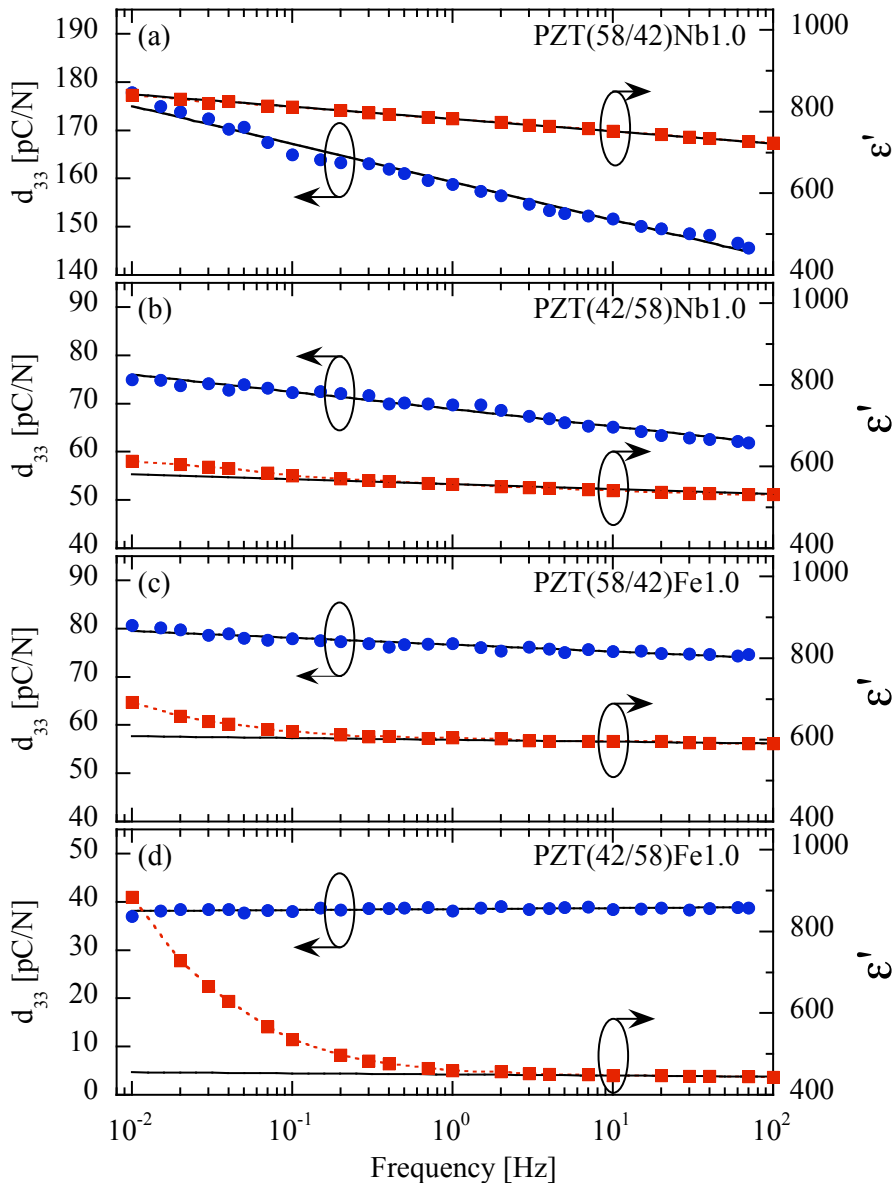
Since both $\varepsilon'$ and $\varepsilon''$ depend on frequency, their relationship could be presented in another way, i.e., Cole-Cole plot. According to the theory developed for the magnetic and dielectric materials with random domain wall pinning (or more generally, pinning of moving interfaces), there are four kinds of relationships between the $\varepsilon'$ and $\varepsilon''$ in Cole-Cole plot (9; 205; 206). As shown in Fig. 6.4, from high frequency to low frequency, the first dispersion is relaxation, which is represented as the semi-circle. The second relationship between $\varepsilon'$ and $\varepsilon''$ is a straight line with an obvious positive slope, which usually is referred to as the "creep" indicating the domain wall motion in a certain direction. Its frequency dependence shows an increase by decreasing the frequency. Keeping on decreasing the frequency to lower values, the $\varepsilon'$ becomes constant while the $\varepsilon''$ increases strongly. This region corresponds to domain wall *slide*. In Cole-Cole plot, this corresponds to a straight-line perpendicular to the horizontal axis. The last process is the switching. This phenomenon, however, is very scarce and has not been reported in ferroelectric materials at weak fields.



**Figure 6.5:** Cole-Cole plot, $\varepsilon'$ versus $\varepsilon''$ of PZT samples at room temperature. The dielectric properties of those samples were measured from 10 mHz to 1 MHz.

Compared with the theoretical description of dielectric response expressed by the Cole-Cole plot, Fig. 6.5 shows the Cole-Cole plot between the $\varepsilon'$ and $\varepsilon''$ from 10 mHz to 1 MHz for

samples investigated here. The conductive behavior of PZT(42/58)Nb1.0, PZT(58/42)Fe1.0 and PZT(42/58)Fe1.0, which has been verified by Morozov and Damjanovic (4), is reflected by the straight lines with a large and positive slope. The most interesting feature is a nearly flat line observed in PZT(58/42)Nb1.0. As shown in Fig. 6.5, it is clear that there is a nearly straight line parallel to the horizontal axis (PZT(42/58)Fe1.0). That is exactly logarithmic dependence, which could not be explained by any of those mechanisms proposed for the domain wall motion in Ref. (9; 205; 206) and presented in Fig. 6.4. In Fig. 6.4 the tilt straight line is assigned as creep. However, the tilt straight lines shown in Fig. 6.5 are related to the conductive behaviors. While the flat straight line observed in PZT(58/42)Nb1.0 is the creep behavior as expected by Kleemann (206).



**Figure 6.6:** Frequency-dependent $d_{33}$ and $\varepsilon'$ of poled PZT samples at room temperature from 10 mHz to 1 MHz. The solid lines across $d_{33}$ and $\varepsilon'$ show the fitting based on Eqs. 6.7 and 6.3 respectively. The dash lines are a guide to the eye.

At low frequencies, the dielectric dispersion in hard group rapidly increases and becomes stronger than in soft group (see Fig. 6.3). The dielectric dispersion in this low frequency range is thus probably dominated by conductive hopping charges (213). Interestingly, the creep regime of domain wall dynamics has a similar functional dependence on the frequency as the hopping charges. This simultaneous presence of the ac conductivity and domain wall displacement is not a problem in soft materials where domain walls contribution to the complex susceptibility is probably an order of magnitude stronger than the conductivity effects (205). However, in hard materials even enhanced domain wall dynamics at low frequencies may be completely screened by the conductivity. One way to avoid the interference of the ac conductivity with domain wall contributions is to study the dispersion in the direct piezoelectric effect or anelastic response of materials. The former is sensitive to elasto-electric defects, such as ferroelastic domain walls while the latter is due to the dynamics of any elastic species, including ferroelastic domain walls or nonelectric elastic defect dipoles (229), but not to pure conductivity.

In order to separate conductive contributions at low frequency, the frequency-dependence of the piezoelectric constant $d_{33}$ was measured. Since we applied the ac stress field to the sample, only the ferroelastic domain walls (non-180° domain walls) respond to the driving field. If response of ferroelastic domain wall at low frequencies for $\varepsilon'$ and $d_{33}$ is similar, it is due to domain and not to conductivity. The contributions to the dielectric and piezoelectric properties by the non-180° domain wall motion should be similar way respect to the frequency. Therefore a compassion between the frequency-dependent $d_{33}$ and $\varepsilon'$ could indentify whether the rapid increase in $\varepsilon'$ at low frequency is due to conductivity and 180° domain wall motion.

**Table 6.2:** Fitting parameters of $d_{33}$ based on Eq. 6.7 and $\varepsilon'$ based on Eq. 6.3 of the data shown in Fig 6.6. $R$ is the linear correlation coefficient.

| Sample | $d'_0$ | $\beta$ | $R$ | Fitting range |
|---|---|---|---|---|
| PZT(58/42)Nb1.0 | 159 | 7.8 | 0.99 | $10^{-2} - 10^2$ Hz |
| PZT(42/58)Nb1.0 | 68.8 | 3.6 | 0.98 | $10^{-2} - 10^2$ Hz |
| PZT(58/42)Fe1.0 | 76.6 | 1.4 | 0.95 | $10^{-2} - 10^2$ Hz |
| PZT(42/58)Fe1.0 | 38.4 | -0.2 | 0.57 | $10^{-2} - 10^2$ Hz |
| Sample | $\varepsilon'_a$ | $\alpha$ | $R$ | Fitting range |
| PZT(58/42)Nb1.0 | 780 | 30.1 | 0.99 | $10^{-2} - 10^5$ Hz |
| PZT(42/58)Nb1.0 | 560 | 11.8 | 0.99 | $10^{-1} - 10^5$ Hz |
| PZT(58/42)Fe1.0 | 600 | 4.3 | 0.98 | $10^1 - 10^5$ Hz |
| PZT(42/58)Fe1.0 | 450 | 2.6 | 0.99 | $10^1 - 10^5$ Hz |

The frequency dependence of the piezoelectric constant $d_{33}$ and $\varepsilon'$ of all studied samples are shown in Fig. 6.6. In order to avoid the aging effect, all the samples were kept for 1 week before the measurement after poling. It is interesting to note that for all samples $d_{33}$ displays a linear response with respect to $\log(f)$ in the whole frequency window. Here we used Eq. 6.7 to

fit the piezoelectric response,

$$d_{33}(f) = d_0 - \beta \log(f). \tag{6.7}$$
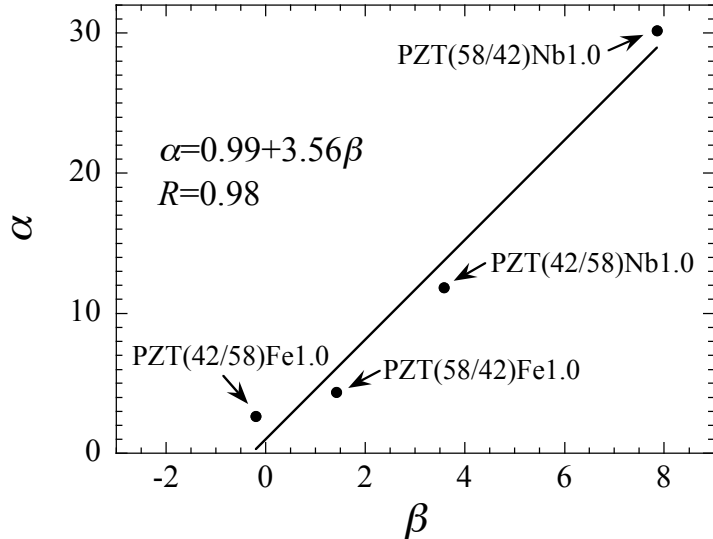
Fitting parameters are given in Table 6.2. As reflected by the $R$, the soft group shows a better fitting than the hard group. If the motion of the domain walls was completely immobilized by the defect dipoles and crystalline potentials, constant piezoelectric response, which originates only from the crystalline lattice instead of the domain wall motion, would be expected. As suggested by data for PZT(42/58)Fe1.0, its $d_{33}$ approaches to such a frequency-independent piezoelectric response. A small but negative $\beta$ in PZT(42/58)Fe1.0 suggest a possible piezo-electric Maxwell-Wagner relaxation at very low frequencies (230). The $\beta$ in the soft group is larger than in the hard group. In both soft and hard groups, the $\beta$ is larger in the rhombohedral phase than in the tetragonal phase.

For comparison, the $\varepsilon'$ of all the samples after poling is also shown in Fig. 6.6. Both the shape and value of the $\varepsilon'$ of all the samples are similar before and after poling. The $\varepsilon'$ was measured form 10 mHz to 1 MHz. In order to compare with $d_{33}$, which was measured below 100 Hz, here we only show the $\varepsilon'$ below 100 Hz. Due to the poling-induced piezoelectric reso-nance effect, strong interference on the $\varepsilon'$ above 100 kHz was observed in all the samples. Here we fit all the $\varepsilon'$ based on Eq. 6.3 but set the upper limit frequency to 100 kHz. The fittings are shown in Fig. 6.6 and parameters are given in Table 6.2. Compared with the hard group, where the deviations from the logarithmic response is rather obvious, the $\varepsilon'$ in the soft group is well fitted by Eq. 6.3. Even though a small deviation is observed in PZT(42/58)Nb1.0 at very low frequency, the magnitude of the deviation of PZT(42/58)Nb1.0 is also small compared with other two hard PZT samples. The most important observation through Fig. 6.6 is the similar-ity between $d_{33}$ and $\varepsilon'$ vs. frequency in soft group and the difference in the hard group. If the dispersions in dielectric and piezoelectric properties originate from the ferroelastic domain wall motion, their response with respect to the frequency should be similar. This is the case observed in the soft group. If the dielectric responses of hard PZT ceramics deviating from the logarithmic function are attributed to ferroelectric 180° domain wall, similar deviations should also be observed in soft PZT ceramics, since both of hard and soft PZTs possess the 180° do-main walls. The absence of the deviation from the logarithmic dispersion in soft PZT ceramics at the same frequency range eliminates this possibility. Therefore the difference between $d_{33}$ and $\varepsilon'$ vs. in hard group can be probably ascribed to the hopping charges contributing to $\varepsilon'$, as suggested by Morozov and Damjanovic (4)[3].

Fig. 6.7 show the relation between $\alpha$ and $\beta$ determined from poled samples. For all studied samples, correlation between $\alpha$ and $\beta$ is high. A linear relation could be found by a simple linear fitting. In general, the soft group possesses large $\alpha$ and $\beta$ compared with the hard group. For the samples with the same dopant, the rhombohedral phase shows larger $\alpha$ and $\beta$ values

---

[3]Our measurements in PZT single crystals (D. Damjanovic, private communication) show similar low fre-quency dielectric dispersion as in ceramics. Thus, significant grain boundary conductivity or their blocking of bulk conductivity can probably be excluded in ceramics. However, electrode polarization, which often accompa-nies ionic hopping conductivity (213) cannot be ruled out as an origin of the low frequency dispersion.
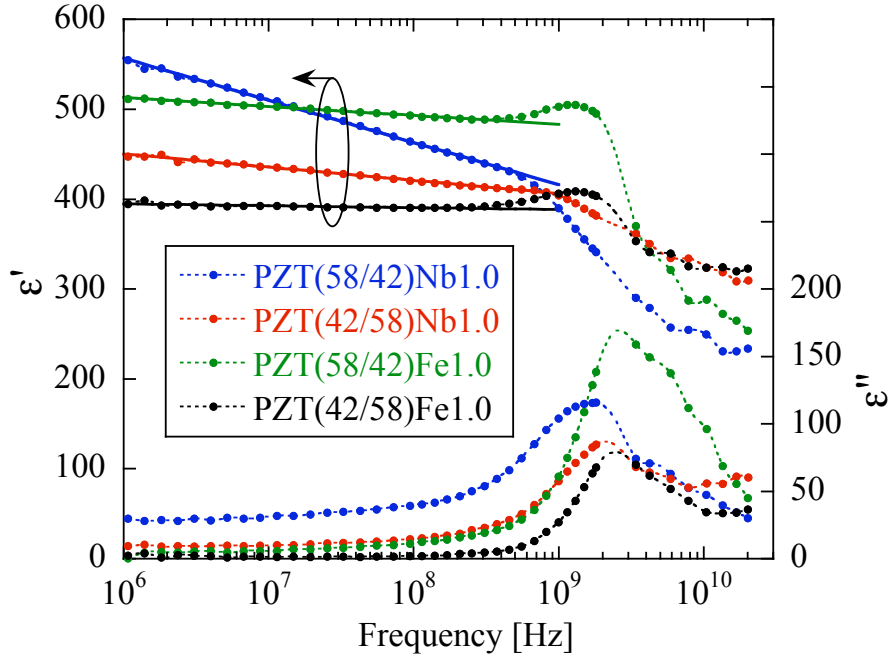
**Figure 6.7:** $\beta$ vs. $\alpha$ of poled PZT samples determined by the fitting based on Eqs. 6.7 and 6.3, respectively. The solid line represents a linear fitting.

than in tetragonal phase. The values of $\alpha$ and $\beta$ are dependent of the magnitude of the disorder in the samples. Due to the absence of pinning in soft materials, high disorder of the defect dipoles correlates to a high domain wall mobility, which results in large values of $\alpha$ and $\beta$, since the dielectric and piezoelectric properties originate from the same domain wall motion. In Fig. 6.7, it can be seen that the defect dipoles in PZT(58/42)Nb1.0 exhibit the largest degree of "disorder". On the contrary, in PZT(42/58)Fe1.0 $\alpha$ and $\beta$ are almost zero, which suggests a completely ordered distribution of the defect dipoles. In hard PZT it has been shown that the domain wall mobility is highly influenced by the distributions of defect dipoles (77). Here we show that the crystalline symmetry could also influence the domain wall mobility. The domain wall mobility could be controlled by both doping kind and crystalline symmetry. Omitting the influence by the conductive hopping charges at low frequency region, all the dielectric and piezoelectric response vs. frequency were well fitted by the logarithmic dispersions. The linear relation between $\alpha$ and $\beta$ supports that these responses come from the same domain wall motion.

Compared with the $\alpha$ obtained in the unpoled state, the corresponding $\alpha$ after poling in soft group becomes smaller. This is most likely caused by the decrease of the domain wall density after poling. The relatively small increase of $\alpha$ in the hard group may also be related to decrease of the domain wall density. This lower domain wall density may result in a weaker pinning effect by the lower coupling efficiency between the domain walls and defect dipoles. Therefore the domain wall mobility is increased a little, and a larger $\alpha$ is observed after poling in hard materials

In Fig. 6.3 we see deviations of the $\varepsilon'$ from the logarithmic dispersion at low frequencies. On the other side, however, this logarithmic dispersion seems to continue to the higher frequency. Next, the $\varepsilon'$ and $\varepsilon''$ spectra of all studied PZT samples were measured from 1 MHz to

**Figure 6.8:** Permittivity $\varepsilon'$ (a) and loss $\varepsilon''$ (b) spectra of PZT samples at room temperature from 1 MHz to 20 GHz. The solid lines are the logarithmic fittings based on Eq 6.3, while the dash lines are a guide to the eye. For a given composition, both $\varepsilon'$ and $\varepsilon''$ share the same color.

1.8 GHz. The data shown in Fig. 6.8 are divided into two regions according to the characteristics of the response. From one to several hundred MHz, the frequency dependence of the $\varepsilon'$ of all samples obeys the logarithmic law, while $\varepsilon''$ increases slowly with increasing the frequency. The relaxation of domain walls is observed in the frequency range from several hundred MHz to 20.2 GHz, where sharp dispersion of the $\varepsilon'$ is accompanied by a peak of $\varepsilon''$.

**Table 6.3:** Fitting parameters of $\varepsilon'$ based on Eq. 6.3 of the data shown in Fig 6.8. $R$ is the linear correlation coefficient.
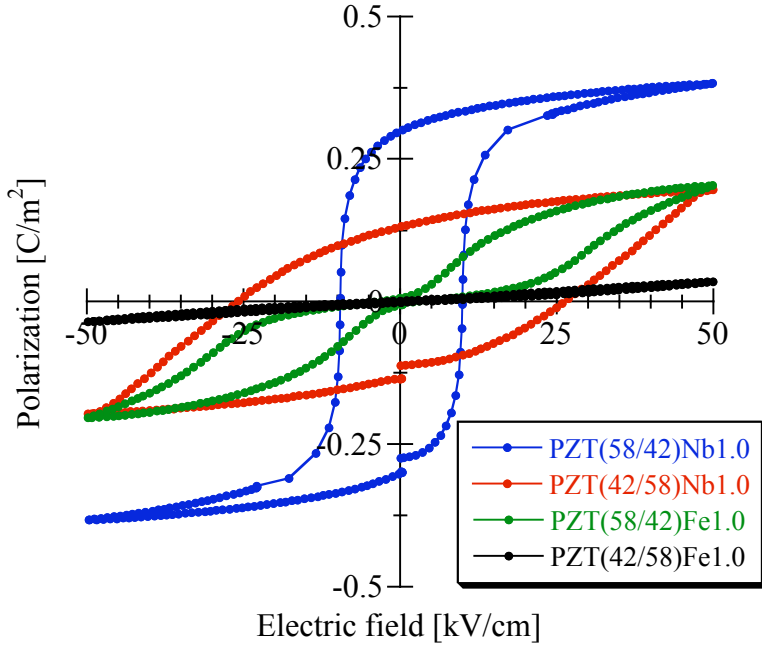
| Sample | $\varepsilon'_a$ | $\alpha$ | $R$ | Fitting range |
|---|---|---|---|---|
| PZT(58/42)Nb1.0 | 840 | 46.9 | 0.99 | $10^6 - 5 \times 10^8$ Hz |
| PZT(42/58)Nb1.0 | 540 | 14.7 | 0.99 | $10^6 - 5 \times 10^8$ Hz |
| PZT(58/42)Fe1.0 | 570 | 9.9 | 0.99 | $10^6 - 2 \times 10^8$ Hz |
| PZT(42/58)Fe1.0 | 410 | 2.2 | 0.81 | $10^6 - 2 \times 10^8$ Hz |

In Fig. 6.8 the fitting results of $\varepsilon'$ by Eq. 6.3 are shown as solid lines and fitting parameters as given in Table 6.3. The $\alpha$ of PZT samples in rhombohedral group shows a large increase compared with the value of the same compositions obtained from Fig. 6.3(a). While the $\alpha$ in tetragonal group displays a rather limited increase. The explanation of the variations of the $\alpha$ is mainly related to the interference by the relaxation of domain walls. It can be seen that the $\varepsilon''$ of the samples in rhombohedral group show a obvious increase when the frequency approaches loss peak frequency $f_R$. According to the Debye relaxation equation Eq. 6.1, the increase of the

$\varepsilon''$ near the $f_R$ is accompanied with a rapid decrease of the $\varepsilon'$. When the frequency increases from one to several hundred MHz, the dominant mechanism of dielectric dispersion by the domain walls transfers from the creep to the relaxation. Kleemann *et al* (231) name such a transformation as "*dynamic phase transition*". This transformation results in a rapid decrease of $\varepsilon'$, and also a larger $\alpha$. That means that there is a competition of two mechanisms (an overlap). So $\alpha$ determined at high frequency data is not a true $\alpha$, which is only related to the creep of domain walls. The domain wall motion in tetragonal group is much more difficult than in rhombohedral group. Therefore the influence of the relaxation on the creep is weaker in tetragonal group. Although the values of the $\alpha$ changes little bit when frequency approaches $f_R$, the general trend of the logarithmic dispersion still hold for all studied samples at least up to several hundred MHz.

Now let us discuss briefly the relaxation in the GHz region. Strictly speaking, here we should use the term "dispersion" instead of the "relaxation" to indicate drastic changes of both $\varepsilon'$ and $\varepsilon'$, since the spectra of the $\varepsilon'$ possesses some characteristics of the resonance. According to the Debye-relaxation equation, the $\varepsilon'$ decreases monotonously by increasing the frequency. This description contradicts with the fact that some humps are observed in the hard PZT. By means of poling, the contribution by piezoelectric grain resonance to the $\varepsilon'$ has been separated. This was possible because the main contribution to this dispersion still originates from the relaxation of domain walls. Note that at 20.2 GHz, the $\varepsilon'$ of the samples with the same symmetry seems to converge to the same value. Above $f_R$, the contribution by the domain wall motion is drastically limited and intrinsic dielectric properties would be approached. The close intrinsic value of the $\varepsilon'$ of the samples with the same crystalline symmetry also supports our assumption that the different $\varepsilon'$ of the soft and hard PZT observed at low frequencies mainly originates from the extrinsic domain wall motion, i.e., the creep and relaxation.
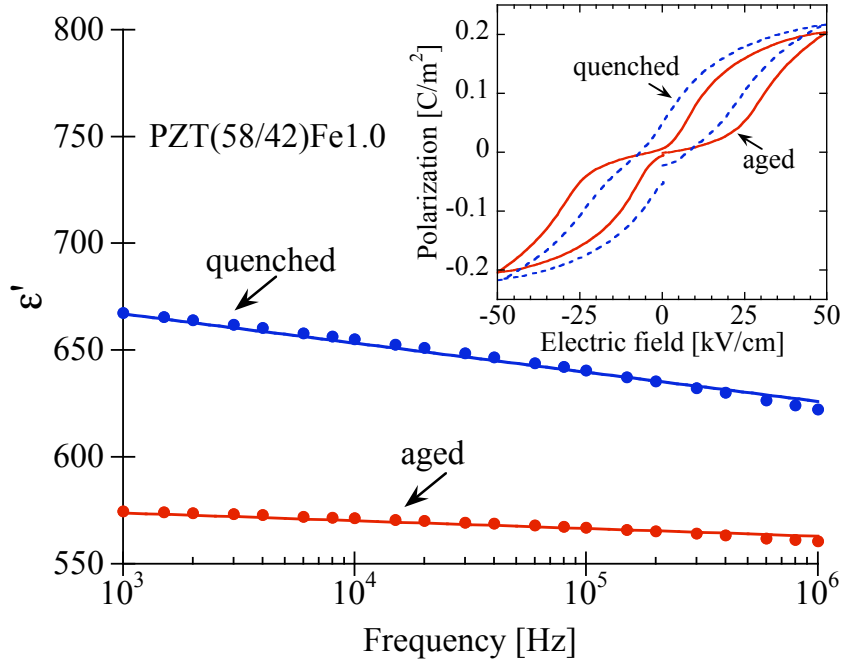
As shown in Figs. 6.3, 6.6 and 6.8, the $\alpha$ is not only influenced by the degree of "disorder", but also by the crystalline symmetry. For the soft group, the doping level is set the same, therefore, the degree of the "disorder" of the $(\mathrm{Nb}^{\bullet}_{\mathrm{Ti,Zr}} - \mathrm{V}''_{\mathrm{Pb}})'$ defect dipoles should also be the same for the rhombohedral and tetragonal samples. Thus the different $\alpha$ between PZT(58/42)Nb1.0 and PZT(42/58)Nb1.0 should be mainly due to the crystalline symmetry. For the hard group, the amount of the $(\mathrm{Fe}'_{\mathrm{Ti,Zr}} - \mathrm{V}^{\bullet\bullet}_{\mathrm{O}})^{\bullet}$ defect dipoles is also the same. Therefore the different pinning effects are mainly ascribed to the difference in the crystalline symmetry. In order to clearly depict the influences of the doping and crystalline symmetry, the hysteresis loops are shown for all studied samples (Fig. 6.9). In PZT(58/42)Nb1.0, we observe a high maxiumum and remnant polarization, small coercive field and large square hysteresis. All those features suggest that the domain wall motion and switching is much easier than in other three samples. For PZT(42/58)Nb1.0, lower maximum and remnant polarization, and much higher coercive field reflect a relative difficulty in the domain wall motion and switching, compared with PZT(58/42)Nb1.0. In the hard group, the most obvious feature is the loop pinching. For PZT(58/42)Fe1.0, although open hysteresis is induced by the stronger field, the pinning loops suggests the difficulty of the domain wall motion at weaker field (strong restoring force). At

**Figure 6.9:** Hysteresis loops of PZT ceramics at room temperature.

extreme case, in PZT(42/58)Fe1.0, even when the field is increased to 50 kV/cm, we fail to in-
duce any switching of polarization. This indicates that the domain walls are completely pinned
by the $(Fe'_{Ti,Zr} - V_O^{\bullet\bullet})^\bullet$ defect dipoles. In a word, all the factors, which influence the domain
wall motion at weak field, would influence logarithmic dispersion (creep).

It is known that the hard PZT exhibits aging effect, which originates from the redistribu-
tion of the $(Fe'_{Ti,Zr} - V_O^{\bullet\bullet})^\bullet$ defect dipoles. Those defect dipoles form with time an ordered
distribution aligning with polarization and immobilize the domain wall motion. Above the $T_C$,
ferroelectric PZT belongs to the cubic phase without any polarization, and the defect dipoles
should distribute randomly. PZT(58/42)Fe1.0 was annealed at 570 °C (150 °C above the $T_C$)
for 1 hour and then quenched in the silicon oil at room temperature. After those treatments, it
is believed that the defect dipoles at frozen at disordered high-temperature state and distributed
randomly. The random distribution is kept at room temperature due to the quenching. Since
the low frequency dielectric characterization (10 mHz to 1 kHz) requires much time (>3 hours),
the aging would take place during measurements. We measured the dielectric response of the
sample in the frequency range from 1 kHz to 1 MHz. Fig. 6.10 shows comparison of $\varepsilon'$ of
PZT(58/42)Fe1.0 between aged and quenched states. By quenching, the $\varepsilon'$ at all frequencies is
increased. The $\alpha$ is also increased from 3.6 to 13.6. As shown in the Fig. 6.10 inset, the pinched
loop almost disappears after quenching. All those characteristics suggest that the pinning ef-
fect by the ordered defect dipoles is reduced, and the domain wall mobility is increased, when
sample is thermally disordered. Disorder in quenched hard materials is lower than in soft mate-
rials, which can be seen by comparing with Fig. 6.3. Through experiments shown in Fig. 6.10,
we show that the ordered distribution of defect dipoles could be decreased by quenching and
domain wall mobility could be increased by decoupling between the defect dipoles and domain

**Figure 6.10:** The $\varepsilon'$ of PZT(58/42)Fe1.0 in aged and quenched states at room temperature. The data and the logarithmic fitting of the aged state are reproduced from Fig. 6.3(a). For the quenching state the logarithmic fitting is conducted in the frequency range from 1 kHz to 1 MHz. The $\alpha$ and $R$ are 13.6 and 0.99, respectively. Inset shows the hysteresis loops of PZT(58/42)Fe1.0 in aging and quenching states at room temperature.

walls.

## 6.4   Summary

- In soft PZT with rhombohedral symmetry the $\varepsilon'$ decreases linearly with the logarithm of the frequency of ac electric field in the range from 10 mHz to several hundred MHz. Soft PZT with tetragonal symmetry shows a similar logarithmic dispersion with a weaker frequency-dependence. In hard group, the logarithmic dispersion of $\varepsilon'$ is observed in rhombohedral phase, while tetragonal phase exhibits a nearly constant permittivity in this frequency range.

- The rapid increase of the $\varepsilon'$ and $\varepsilon''$ and their deviations from the logarithmic dispersion and NCL respectively at low frequencies is mainly due to the conductivity by the oxygen vacancy in hard group and electrons in soft group (4). Frequency dependence of piezoelectric constant $d_{33}$ of all studied PZT samples from 10 mHz to 100 Hz shows a similar logarithmic dispersion. This supports that the ferroelastic domain wall motion contributes to the dielectric and piezoelectric properties through the same logarithmic law.

- For all the samples, a nearly constant loss (NCL) behavior of $\varepsilon''$ accompanies the logarithmic dispersion in the same frequency range. This logarithmic dispersion is ascribed to creep of the domain wall. By combining dielectric and piezoelectric measurements we show that the

strong low frequency dispersion in hard ceramics is more likely related to charge hopping rather than motion of non-180° domain walls. Furthermore, it should be noted that piezo-electric nonlinearity with respect to driving field as described by the Rayleigh law (204) also corresponds to motion of domain walls in a random potential. It is thus likely that logarithmic frequency dependence observed in soft PZT materials and accompanied by Rayleigh -type field nonlinearity (228) corresponds to creep.

- We demonstrate that such a logarithmic dispersion is expected in classic ferroelectric soft PZT ceramics with disordered dipolar defects. In soft or hard PZT, the frequency dependence of the logarithmic dispersion is stronger in rhombohedral phase than in tetragonal phase. In the hard PZT, strong frequency dependence of the logarithmic dispersion is also observed by disturbing the ordered state of defects dipoles through quenching.

# Chapter 7

# Conclusions and perspectives
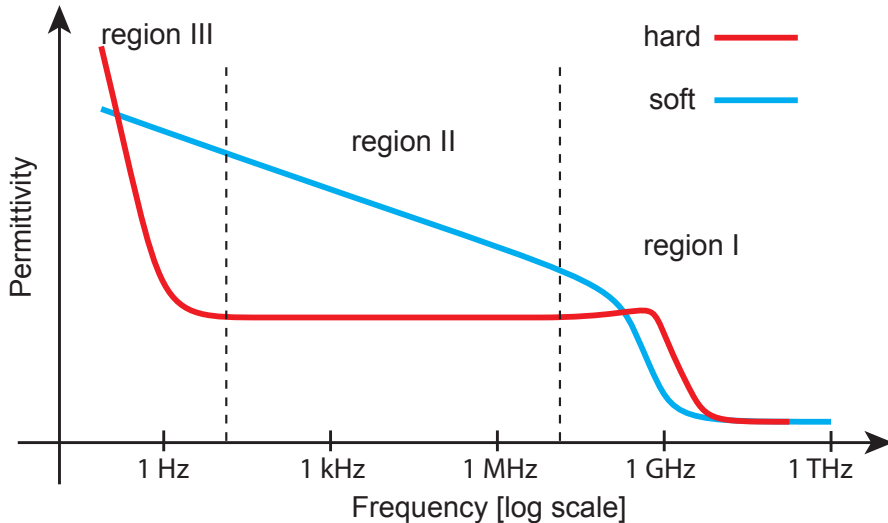
The present works attempts to contribute to the understanding of the hardening and softening mechanisms in PZT ferroelectric ceramics by focusing on their dielectric response which is investigated over a broad frequency range. The dielectric spectroscopy study is complemented by investigation of the domain structure using transmission and scanning electron microscopy.

In the following, the main achievements of this thesis are summarized starting with the general qualitative description of the broadband dielectric response of hard and soft PZTs. Related domain structures and their relations with the grain size are then presented. Finally the questions posed at the beginning of this work and unveiled answers are presented along with suggestions for the further studies that may be conducted on the basis of results of this thesis.

## 7.1 General qualitative description of the broadband dielectric response of hard and soft PZT ceramics

By means of different dielectric measurement techniques, consecutive dielectric spectra are measured to reveal the dielectric response of hard and soft PZT ferroelectric ceramics from 10 mHz to 20 GHz. A general description of the frequency dependence of dielectric properties of hard and soft PZTs was established based on these dielectric characterizations. As shown schematically in Fig.1, the dielectric response is divided into three regions, which correspond to the different mechanisms that govern the dielectric response of the hard and soft PZTs. Based on this general figure, we will summarize the main difference of the dielectric response of the hard and soft PZTs in these three regions.

- **Region I**: The frequency range of region I is located from several hundred MHz to tens of GHz. The dielectric responses of hard and soft PZTs discussed in region I are referred to as "microwave dielectric properties". In this region, both hard and soft PZTs undergo a dielectric dispersion, which manifest itself as large decrease of the permittivity on increasing frequency followed by a loss peak. There are two mechanisms governing simultaneously the dielectric dispersion. The main part of this dispersion originates from domain wall relaxation, while piezoelectric grain resonances (as shown as a hump in Fig 7.1) also contribute

**Figure 7.1:** A general description of the broadband dielectric response of hard and soft PZTs. The dielectric response is divided into three regions according to the characteristic responses in hard and soft PZTs.

to the dispersion at somewhat lower frequencies. By means of gradual poling, the piezo-electric grain resonance is revealed, since the domain wall density is decreased by external electric field (Chapter 4). The dispersion frequency of the piezoelectric grain resonance is in reverse proportion to the mean grain size of samples; this holds for grain size in the range between 1 and 10 µm. Because the doping mainly results in changes in domain structures and mobility (extrinsic contribution) rather than of the crystalline lattice (intrinsic contribu-tion), similar dielectric responses of hard and soft PZTs are observed above about 10 GHz, where the intrinsic dielectric response is approached. In order to simplify the description, in Fig 7.1 the permittivity of hard and soft PZTs converge to the same value at high frequencies, which may not be the case for samples with different Zr/Ti ratio. In addition, the dispersion frequency may be different for hard and soft samples with the same Zr/Ti ratio due to the different mean domain size (domain width).

- **Region II**: The frequency range of the region II shown in Fig 7.1 spreads over at least 8 decades of frequency. The lower limit frequency of this range is less than 1 Hz, while the upper limit frequency could reach several hundred MHz. In such a region, the dielectric response of soft PZT shows a logarithmic dispersion, which could be described a logarithmic function on log-linear scale. On the contrary, the dielectric response of hard PZT is almost independent of frequency if the domain walls are completely pinned by defect dipoles. In this case, domain walls move but not jump. Rather they vibrate about the pinning centers. Without the interferences from other dispersion mechanisms, the losses of both hard and soft PZTs are independent of frequency in this region. By controlling the doping kind and crystalline symmetry, the slope of the logarithmic dispersion could be adjusted. A large slope is observed in PZT compositions with a large disorder. The origin of the logarithmic dispersion comes from the creep-like domain wall motion, i.e., a motion of domain walls in

a random potential. In hard materials the domain walls vibrate around pinning centers and are confined in at bottom of deep potential wells.

- **Region III**: The upper limit frequency of this region is determined by the frequency, below which the permittivity of hard PZT increases sharply. In hard PZT, oxygen vacancies are induced by acceptor doping to compensate acceptor charge. These defect vacancies contribute (in fact, dominate) conductivity by the hopping mechanism and at the same time contribute to increase of the apparent permittivity at low enough frequencies. In the same region, the response of soft PZT still follows the logarithmic behavior observed in region II. Under an external electric field, both the conductive hopping charges and domain walls may contribute to the dielectric properties. However, only non-180° ferroelastic domain walls respond to the external mechanical driving field. Thus, by comparing the piezoelectric and dielectric responses, it may be possible to separate contributions from the displacement of ferroelastic domain walls (observed in piezoelectric effect and permittivity) from conductivity (affects only permittivity). The frequency-dependent piezoelectric constants of both soft and hard PZTs are described by a logarithmic function in the frequency range from 10 mHz to 100 Hz. Strong dispersion in the permittivity characteristic for hard ceramics at low frequencies has not been observed in the piezoelectric response. Together, these data suggest that the low frequency dispersion in the permittivity of hard materials is dominated by contribution form hopping charges.

## 7.2 Domain configurations and relationship between the domain size and grain size

Compared with previous reports on undoped PZT ceramics, the investigation of domain structures presented in this thesis mainly focus on doped PZT ceramics with compositions in rhombohdral, tetragonal and MPB regions. Following conclusions are obtained:

- Nanodomains are observed in $Fe^{3+}$-doped hard PZT with composition at MPB, however, their presence does not correlate with high dielectric and piezoelectric properties, as might be expected from some theoretical models. Compared to domain size, domain wall mobility appears to have a stronger effect on properties.

- The domain size decreases when compositions approach the MPB region from both rhombohdral and tetragonal sides. Besides this composition effect, another effect which decreases domain size is observed in acceptor doped ceramics, in agremeent with previous reports in the literature. This effect is verified here for the PZT compositions in rhombohedral, tetragonal and MPB regions. The presence of the oxygen vacancies, which may break continuity of polarization, is most likely responsible for the decreasing domain size in acceptor doped samples.

- The parabolic relationship between domain size and grain size has been previously proposed theoretically and has been verified experimentally for undoped PZT compositions. Our data suggests that ultra small domain size observed in $Fe^{3+}$-doped PZTs deviates from this prediction. On the contrary, this law is applicable to the $Nb^{5+}$-doped soft PZTs.

## 7.3   Perspectives and suggestions for future work

As this study presents the first characterization of the broadband dielectric response of hard and soft PZT ferroelectric ceramics as a key to understand the hardening and softening mechanisms, numerous issues remain open. Several interesting avenues of investigation can be suggested according to those open questions.

- The origin of the microwave dielectric dispersion is ascribed to the domain wall relaxation and piezoelectric grain resonance, which are separated by means of gradual poling. Above $T_C$, both the domain structure and piezoelectricity will disappear. Thus, the absence of the microwave dielectric dispersion is expected above $T_C$, Interestingly, some authors [148] still report on strong microwave dispersion above $T_C$ in $BaTiO_3$ ceramics. The high $T_C$ of the PZT system results in difficulties in dielectric characterization in the paraelectric region. The general description presented here should be repeated on a material with a low $T_C$ to verify the absence of the dispersion in microwave region. One candidate material is $(Ba,Sr)TiO_3$, where $T_C$ can be adjusted by the Ba/Sr ratio.

- Due to the coupling effect between the grains and domains vibrations in polycrystalline PZT ceramics, similar dielectric characterization in the microwave frequency range in polydomain and monodomain single crystals is important to confirm and clarify the origin of the microwave dielectric dispersion proposed here.

- For the microwave dielectric dispersion, the dispersion frequency corresponding to the piezoelectric grain resonance has been correlated to the mean grain size. There is no satisfactory model which could predict the dispersion frequency as related to the domain wall relaxation.

- The parabolic relationship between the domain size and grain size is obtained by thermodynamic calculations, and has been verified in undoped and soft PZT ceramics. Obvious deviations from this law are observed in hard PZT ceramics. A modification of this relationship for hard PZT ceramics should take into account the domain wall energy related to the doping effect.

- In hard PZT, oxygen vacancies could possibly be located preferentially at domain walls, imprinting a nanodomain structure. It is of great interest to establish the exact location of oxygen vacancy (within a domain or at a domain wall).

- Substituting $Nb^{5+}$ at the B-site in PZT clearly results in donor doping, however, the details of the compensation mechanisms can vary, depending on by processing conditions and dopant concentration, and have not been firmly established. Positron annihilation lifetime spectroscopy (PALS) would be suitable to study the variation in vacancy defect content in $Nb^{5+}$-doped PZT ceramics, because of its particular sensitivity to cation vacancy defects in perovskite oxide materials.

- Identification the new phase transition due to the tilting of oxygen octahedron in PZT with high Ti concentration.

# Appendix A

# Technical details

## A.1  THz frequency range characterizations

All experiments were performed at Institute of Physics, Academy of Sciences of the Czech Republic.

### A.1.1  Raman spectra

Raman spectra were excited with the 514.5 nm line of an Ar laser at a power of about 30 mW (∼5 mW on the sample) and recorded in back-scattering geometry using a RM-1000 RENISHAW Raman microscope, equipped with a grating filter enabling good stray light rejection, in the $20 - 850 \, \text{cm}^{-1}$ range. The diameter of the laser spot on the sample surface was $2 - 3 \, \mu\text{m}$. A THMS-600 cell (LINKAM) was used for temperature control of the samples from 300 to 800 K. For low-temperature spectra (between 300 and 10 K), samples were loaded into a continuous-flow He cryostat (Oxford Instruments) and the microscope was equipped with a special angled arm carrying a x20 ULWD objective for efficient optical coupling. The spectral resolution was below $2 \, \text{cm}^{-1}$.

### A.1.2  THz spectra

Time-domain THz (TDTHz) transmission measurements were carried out on thin polished plane-parallel samples (thickness 70 μm) in the temperature range $20 - 900$ K. A custom-made TDTHz transmission spectrometer was used to obtain the complex dielectric response from 5 to $30 \, \text{cm}^{-1}$ with a resolution of $0.5 \, \text{cm}^{-1}$. At higher frequencies the samples were opaque. An Optistat CF cryostat with Mylar windows (thickness of 25 and 50 μm for the inner and outside windows, respectively) was used for measurements down to 20 K. Adapted commercial high-temperature cell SPECAC P/N 5850 was used to heat the samples up to 900 K.

## A.2   Fitting of the THz complex dielectric spectra

The measured IR reflectivity spectra were fitted together with the THz complex dielectric spectra, using the factorized multi-oscillator model of the dielectric function (232):

$$\varepsilon^*(\omega) = \varepsilon'(\omega) - \varepsilon''(\omega) = \varepsilon_\infty \prod_{j=1}^{n} \frac{\omega_{\mathrm{LO}j}^2 - \omega^2 + \mathrm{i}\omega\gamma_{\mathrm{LO}j}}{\omega_{\mathrm{TO}j}^2 - \omega^2 + \mathrm{i}\omega\gamma_{\mathrm{TO}j}}, \tag{A.1}$$

$$\Delta\varepsilon_j = \frac{\varepsilon_\infty}{\omega_{\mathrm{TO}j}^2} \cdot \frac{\prod_k \left( \omega_{\mathrm{LO}k}^2 - \omega_{\mathrm{LO}j}^2 \right)}{\prod_{k\neq j} \left( \omega_{\mathrm{TO}k}^2 - \omega_{\mathrm{TO}j}^2 \right)}, \tag{A.2}$$

where $\varepsilon_\infty$ is the permittivity at frequencies much higher than all polar phonon frequencies; $\omega_{\mathrm{TO}j}$ and $\omega_{\mathrm{TO}j}$ the transverse and longitudinal frequencies of the $j$-th phonon mode, $\gamma_{\mathrm{TO}j}$ and $\gamma_{\mathrm{LO}j}$, the respective damping constants; and $\Delta\varepsilon_j$ refers to its dielectric contribution. The complex dielectric permittivity $\varepsilon^*(\omega)$ is related to the reflectivity spectrum $R(v)$ by

$$R(v) = \left| \frac{\sqrt{\varepsilon^*(v)} - 1}{\sqrt{\varepsilon^*(v)} + 1} \right|^2. \tag{A.3}$$

# Bibliography

[1] G. H. Haertling, "Ferroelectric ceramics: History and technology," *Journal of the American Ceramic Society*, vol. 82, no. 4, pp. 797–818, 1999.

[2] B. Jaffe, W. R. Cook, and H. Jaffe, *Piezoelectric ceramics*. New York: Academic Press, 1971.

[3] M. I. Morozov and D. Damjanovic, "Hardening-softening transition in Fe-doped Pb(Zr,Ti)O$_3$ ceramics and evolution of the third harmonic of the polarization response," *Journal of Applied Physics*, vol. 104, no. 3, p. 034107, 2008.

[4] M. I. Morozov and D. Damjanovic, "Charge migration in Pb(Zr,Ti)O$_3$ ceramics and its relation to ageing, hardening, and softening," *Journal of Applied Physics*, vol. 107, no. 3, p. 034106, 2010.

[5] S. J. Zhang, J. B. Lim, H. J. Lee, and T. R. Shrout, "Characterization of hard piezoelectric lead-free ceramics," *IEEE Transactions on Ultrasonics, Ferroelectrics, and Frequency Control*, vol. 56, no. 8, pp. 1523–1527, 2009.

[6] J. B. Lim, S. J. Zhang, J. H. Jeon, and T. Shrout, "(K,Na)NbO$_3$-based ceramics for piezoelectric "hard" lead-free materials," *Journal of the American Ceramic Society*, vol. 93, no. 5, pp. 1218–1220, 2010.

[7] W. Jo, E. Erdem, R. A. Eichel, J. Glaum, T. Granzow, D. Damjanovic, and J. Rödel, "Effect of Nb-donor and Fe-acceptor dopants in (Bi$_{1/2}$Na$_{1/2}$)TiO$_{0.5}$-BaTiO$_3$-(K$_{0.5}$Na$_{0.5}$)NbO$_3$ lead-free piezoceramics," *Journal of Applied Physics*, vol. 108, no. 1, p. 014110, 2010.

[8] M. E. Lines and A. M. Glass, *Principles and applications of ferroelectrics and related materials*. Oxford: Clarendon Press, 1977.

[9] A. K. Taganstev, J. Fousek, and L. E. Cross, *Domains in ferroic crystals and thin films*. New York: Springer, 2010.

[10] J. F. Nye, *Physical properties of crystals*. Oxford: Clarendon, 2nd ed., 1985.

[11] G. Shirane, F. Jona, and R. Pepinsky, "Some aspects of ferroelectricity," *Proceedings of the Institute of Radio Engineers*, vol. 43, no. 12, pp. 1738–1793, 1955.

[12] G. Arlt, "Twinning in ferroelectric and ferroelastic ceramics. Stress relief," *Journal of Materials Science*, vol. 25, no. 6, pp. 2655–2666, 1990.

[13] J. Valasek, "Piezo-electric and allied phenomena in Rochelle salt," *Physical Review*, vol. 17, no. 4, pp. 475–481, 1921.

[14] L. G. Tejuca and J. L. G. Fierro, *Properties and applications of perovskite-type oxides*. New York: Dekker, 1993.

[15] A. Bhalla, R. Guo, and R. Roy, "The perovskite structure-A review of its role in ceramic science and technology," *Materials Research Innovations*, vol. 4, no. 1, pp. 3–26, 2000.

[16] Y. H. Xu, *Ferroelectric materials and their applications*. New York: Elsevier Science Press, 1991.

[17] J. Hlinka, M. Kempa, J. Kulda, P. Bourges, A. Kania, and J. Petzelt, "Lattice dynamics of ferroelectric $PbTiO_3$ by inelastic neutron scattering," *Physical Review B*, vol. 73, no. 14, p. 140101(R), 2006.

[18] G. Shirane and D. A. Takeda, "Phase transitions in solid solutions of $PbZrO_3$ and $PbTiO_3$. I. Small concentrations of $PbTiO_3$," *Journal of the Physical Society of Japan*, vol. 7, no. 1, pp. 5–11, 1952.

[19] G. Shirane, K. Suzuki, and A. Takeda, "Phase transitions in solid solutions of $PbZrO_3$ and $PbTiO_3$. II. X-ray study," *Journal of the Physical Society of Japan*, vol. 7, no. 1, pp. 12–18, 1952.

[20] G. Shirane and K. Suzuki, "Crystal structure of $Pb(Zr-Ti)O_3$," *Journal of the Physical Society of Japan*, vol. 7, no. 3, p. 333, 1952.

[21] B. Jaffe, R. S. Roth, and S. Marzullo, "Properties of piezoelectric ceramics in the solid-solution series lead titanate-lead zirconate-lead oxide: tin oxide and lead titanate-lead hafnate," *Journal of Research of the National Bureau of Standards*, vol. 55, no. 5, pp. 239–254, 1955.

[22] H. M. Barnett, "Evidence for a new phase boundary in the ferroelectric lead zirconate-lead titanate system," *Journal of Applied Physics*, vol. 33, no. 4, p. 1606, 1962.

[23] D. Berlincourt, H. H. A. Krueger, and B. Jaffe, "Stability of phases in modified lead zirconate with variation in pressure, electric field, temperature and composition," *Journal of Physics and Chemistry of Solids*, vol. 25, no. 7, pp. 659–674, 1964.

[24] M. J. Haun, E. Furman, T. R. Halemane, and L. E. Cross, "Thermodynamic theory of the lead zirconate-titanate solid solution system, Part IV: Tilting of the oxygen octahedra," *Ferroelectrics*, vol. 99, no. 1, pp. 55–62, 1989.

[25] B. Noheda, "Structure and high-piezoelectricity in lead oxide solid solutions," *Current Opinion in Solid State and Materials Science*, vol. 6, no. 1, pp. 27–34, 2002.

[26] B. Noheda and D. E. Cox, "Bridging phases at the morphotropic boundaries of lead oxide solid solutions," *Phase Transitions*, vol. 79, no. 1-2, pp. 5–20, 2006.

[27] V. Isupov, "Comments on the paper 'X-ray study of the PZT solid solutions near the morphotropic phase transition'," *Solid State Communications*, vol. 17, no. 11, pp. 1331–1333, 1975.

[28] K. Kakegawa, J. Mohri, T. Takahashi, H. Yamamura, and S. Shirasaki, "A compositional fluctu-ation and properties of Pb(Zr,Ti)O$_3$," *Solid State Communications*, vol. 24, no. 11, pp. 769–772, 1977.

[29] S. K. Mishra, D. Pandey, and A. P. Singh, "Effect of phase coexistence at morphotropic phase boundary on the properties of Pb(Zr$_x$Ti$_{1-x}$)O$_3$ ceramics," *Applied Physics Letters*, vol. 69, no. 12, pp. 1707–1709, 1996.

[30] W. Cao and L. E. Cross, "Theoretical model for the morphotropic phase boundary in lead zirconate–lead titanate solid solution," *Physical Review B*, vol. 47, no. 9, pp. 4825–4830, 1993.

[31] A. M. Glazer, P. A. Thomas, K. Z. Baba-Kishi, G. K. H. Pang, and C. W. Tai, "Influence of short-range and long-range order on the evolution of the morphotropic phase boundary in Pb(Zr$_{1-x}$Ti$_x$)O$_3$," *Physical Review B*, vol. 70, no. 18, p. 184123, 2004.

[32] B. Noheda, D. E. Cox, G. Shirane, R. Guo, B. Jones, and L. E. Cross, "Stability of the mono-clinic phase in the ferroelectric perovskite Pb(Zr$_{1-x}$Ti$_x$)O$_3$," *Physical Review B*, vol. 63, no. 1, p. 014103, 2001.

[33] B. Noheda, D. E. Cox, G. Shirane, J. A. Gonzalo, L. E. Cross, and S. E. Park, "A monoclinic ferroelectric phase in the Pb(Zr$_{1-x}$Ti$_x$)O$_3$ solid solution," *Applied Physics Letters*, vol. 74, no. 14, pp. 2059–2061, 1999.

[34] B. Noheda, J. A. Gonzalo, L. E. Cross, R. Guo, S. E. Park, D. E. Cox, and G. Shirane, "Tetragonal-to-monoclinic phase transition in a ferroelectric perovskite: The structure of PbZr$_{0.52}$Ti$_{0.48}$O$_3$," *Physical Review B*, vol. 61, no. 13, pp. 8687–8695, 2000.

[35] L. Bellaiche, A. Garcia, and D. Vanderbilt, "Finite-temperature properties of Pb(Zr$_{1-x}$Ti$_x$)O$_3$ alloys from first principles," *Physical Review Letters*, vol. 84, no. 23, pp. 5427–5430, 2000.

[36] D. Vanderbilt and M. H. Cohen, "Monoclinic and triclinic phases in higher-order Devonshire theory," *Physical Review B*, vol. 63, no. 9, p. 094108, 2001.

[37] D. Viehland, "Symmetry-adaptive ferroelectric mesostates in oriented Pb(BI$_{1/3}$BII$_{2/3}$)O$_3$-PbTiO$_3$ crystals," *Journal of Applied Physics*, vol. 88, no. 8, pp. 4794–4806, 2000.

[38] Y. M. Jin, Y. U. Wang, A. G. Khachaturyan, J. F. Li, and D. Viehland, "Adaptive ferroelectric states in systems with low domain wall energy: Tetragonal microdomains," *Journal of Applied Physics*, vol. 94, no. 5, pp. 3629–3640, 2003.

[39] Y. M. Jin, Y. U. Wang, A. G. Khachaturyan, J. F. Li, and D. Viehland, "Conformal miniaturization of domains with low domain-wall energy: Monoclinic ferroelectric States near the morphotropic phase boundaries," *Physical Review Letters*, vol. 91, no. 19, p. 197601, 2003.

[40] K. A. Schönau, L. A. Schmitt, M. Knapp, H. Fuess, R. A. Eichel, H. Kungl, and M. J. Hoffmann, "Nanodomain structure of Pb[Zr$_{1-x}$Ti$_x$]O$_3$ at its morphotropic phase boundary: Investigations from local to average structure," *Physical Review B*, vol. 75, no. 18, p. 184117, 2007.

[41] L. A. Schmitt, K. A. Schönau, R. Theissmann, H. Fuess, H. Kungl, and M. J. Hoffmann, "Composition dependence of the domain configuration and size in Pb(Zr$_{1-x}$Ti$_x$)O$_3$ ceramics," *Journal of Applied Physics*, vol. 101, no. 7, p. 074107, 2007.

[42] R. Theissmann, L. A. Schmitt, J. Kling, R. Schierholz, K. A. Schonau, H. Fuess, M. Knapp, H. Kungl, and M. J. Hoffmann, "Nanodomains in morphotropic lead zirconate titanate ceramics: On the origin of the strong piezoelectric effect," *Journal of Applied Physics*, vol. 102, no. 2, p. 024111, 2007.

[43] R. Schierholz, H. Fuess, K. Tsuda, Y. Ogata, M. Terauchi, and R. Theissmann, "Crystal symmetry in single domains of PbZr$_{0.54}$Ti$_{0.46}$O$_3$," *Physical Review B*, vol. 78, no. 2, p. 024118, 2008.

[44] B. Jaffe, R. S. Roth, and S. Marzullo, "Piezoelectric properties of lead zirconate-lead titanate solid-solution ceramics," *Journal of Applied Physics*, vol. 25, no. 6, pp. 809–810, 1954.

[45] D. Berlincourt, C. Cmolik, and H. Jaffe, "Piezoelectric properties of polycrystalline lead titanate zirconate compositions," *Proceedings of the Institute of Radio Engineers*, vol. 48, no. 2, pp. 220–229, 1960.

[46] D. Berlincourt, "Variation of electroelastic constants of polycrystalline lead titanate zirconate with thoroughness of poling," *Journal of the Acoustical Society of America*, vol. 36, no. 3, pp. 515–520, 1964.

[47] M. J. Haun, E. Furman, S. J. Jang, and L. E. Cross, "Thermodynamic theory of the lead zirconate-titanate solid solution system, Part V: Theoretical calculations," *Ferroelectrics*, vol. 99, no. 1, pp. 63–86, 1989.

[48] Q. M. Zhang, W. Y. Pan, S. J. Jang, and L. E. Cross, "Domain wall excitations and their contributions to the weak-signal response of doped lead zirconate titanate ceramics," *Journal of Applied Physics*, vol. 64, no. 11, pp. 6445–6451, 1988.

[49] Q. M. Zhang, H. Wang, N. Kim, and L. E. Cross, "Direct evaluation of domain-wall and intrinsic contributions to the dielectric and piezoelectric response and their temperature dependence on lead zirconate-titanate ceramics," *Journal of Applied Physics*, vol. 75, no. 1, pp. 454–459, 1994.

[50] C. A. Randall, N. Kim, J. P. Kucera, W. W. Cao, and T. R. Shrout, "Intrinsic and extrinsic size effects in fine-grained morphotropic-phase-boundary lead zirconate titanate ceramics," *Journal of the American Ceramic Society*, vol. 81, no. 3, pp. 677–688, 1998.

[51] D. Damjanovic, "Contributions to the piezoelectric effect in ferroelectric single crystals and ceramics," *Journal of the American Ceramic Society*, vol. 88, no. 10, pp. 2663–2676, 2005.

[52] A. F. Devonshire, "Theory of barium titanate," *Philosophical Magazine*, vol. 40, no. 309, pp. 1040–1063, 1949.

[53] A. F. Devonshire, "Theory of barium titanate. –Part II," *Philosophical Magazine*, vol. 42, no. 333, pp. 1065–1079, 1951.

[54] A. F. Devonshire, "Theory of ferroelectrics," *Advances in Physics*, vol. 3, no. 10, pp. 85–130, 1954.

[55] A. Amin, M. J. Haun, B. Badger, H. McKinstry, and L. E. Cross, "A phenomenological Gibbs function for the single cell region of the PbZrO$_3$:PbTiO$_3$ solid solution system," *Ferroelectrics*, vol. 65, no. 1-2, pp. 107–130, 1985.

[56] M. J. Haun, E. Furman, S. J. Jang, H. A. McKinstry, and L. E. Cross, "Thermodynamic theory of PbTiO$_3$," *Journal of Applied Physics*, vol. 62, no. 8, pp. 3331–3338, 1987.

[57] M. J. Haun, E. Furman, S. J. Jang, and L. E. Cross, "Thermodynamic theory of the lead zirconate-titanate solid solution system, Part I: Phenomenology," *Ferroelectrics*, vol. 99, no. 1, pp. 13–25, 1989.

[58] M. J. Haun, E. Furman, H. A. McKinstry, and L. E. Cross, "Thermodynamic theory of the lead zirconate-titanate solid solution system, Part II: Tricritical hehavior," *Ferroelectrics*, vol. 99, no. 1, pp. 27–44, 1989.

[59] M. J. Haun, Z. Q. Zhuang, E. Furman, S. J. Jang, and L. E. Cross, "Thermodynamic theory of the lead zirconate-titanate solid solution system, Part III: Curie constant and sixth-order polarization interaction dielectric stiffness coefficients," *Ferroelectrics*, vol. 99, no. 1, pp. 45–54, 1989.

[60] M. J. Haun, T. J. Harvin, M. T. Lanagan, Z. Q. Zhuang, S. J. Jang, and L. E. Cross, "Thermodynamic theory of PbZrO$_3$," *Journal of Applied Physics*, vol. 65, no. 8, pp. 3173–3180, 1989.

[61] L. E. Cross, "Ferroelectrics ceramics: Tailoring properties for specific applications," in *Ferroelectric ceramics: Tutorial reviews, theory, processing, and applications*, Edited by N. Setter and E. L. Colle. Birkhäuser Verlag, Basel, 1993, pp. 1-85.

[62] G. Arlt, "The role of domain walls on the dielectric, elastic and piezoelectric properties of ferroelectric ceramics," *Ferroelectrics*, vol. 76, no. 3-4, pp. 451–458, 1987.

[63] R. Herbiet, U. Robels, H. Dederichs, and G. Arlt, "Domain wall and volume contributions to material properties of PZT ceramics," *Ferroelectrics*, vol. 98, no. 1, pp. 107–21, 1989.

[64] G. Arlt, "Microstructure and domain effects in ferroelectric ceramics," *Ferroelectrics*, vol. 91, no. 1, pp. 3–7, 1989.

[65] G. Arlt, "The influence of microstructure on the properties of ferroelectric ceramics," *Ferroelectrics*, vol. 104, no. 1, pp. 217–227, 1990.

[66] F. Kulcsar, "Electromechanical properties of lead titanate zirconate ceramics modifed with certain three- or five-valent additions," *Journal of the American Ceramic Society*, vol. 42, no. 7, pp. 343–349, 1959.

[67] F. Kulcsar, "Electromechanical properties of lead titanate zirconate ceramics modified with tungsten and thorium," *Journal of the American Ceramic Society*, vol. 48, no. 1, p. 54, 1965.

[68] R. Gerson, "Variation in ferroelectric characteristics of lead zirconate titanate ceramics due to minor chemical modifications," *Journal of Applied Physics*, vol. 31, no. 1, pp. 188–194, 1960.

[69] R. Gerson and H. Jaffe, "Electrical conductivity in lead titanate zirconate ceramics," *Journal of Physics and Chemistry of Solids*, vol. 24, no. 8, pp. 979–984, 1963.

[70] X. L. Zhang, Z. X. Chen, L. E. Cross, and W. A. Schulze, "Dielectric and piezoelectric properties of modified lead titanate zirconate ceramics from 4.2 to 300K," *Journal of Materials Science*, vol. 18, no. 4, pp. 968–972, 1983.

[71] G. H. Jonker, "Nature of aging in ferroelectric ceramics," *Journal of the American Ceramic Society*, vol. 55, no. 1, pp. 57–58, 1972.

[72] K. Carl and K. H. Härdtl, "Electrical after-effects in Pb(Ti,Zr)O$_3$ ceramics," *Ferroelectrics*, vol. 17, no. 3-4, pp. 473–486, 1978.

[73] P. V. Lambeck and G. H. Jonker, "The nature of domain stabilization in ferroelectric perovskites," *Journal of the Physics and Chemistry of Solids*, vol. 47, no. 5, pp. 453–461, 1986.

[74] U. Robels and G. Arlt, "Domain wall clamping in ferroelectrics by orientation of defects," *Journal of Applied Physics*, vol. 73, no. 7, pp. 3454–3460, 1993.

[75] Q. Tan, J. F. Li, and D. Viehland, "Ferroelectric behaviours dominated by mobile and randomly quenched impurities in modified lead zirconate titanate ceramics," *Philosophical Magazine B*, vol. 76, no. 1, pp. 59–74, 1997.

[76] X. B. Ren, "Large electric-field-induced strain in ferroelectric crystals by point-defect-mediated reversible domain switching," *Nature Materials*, vol. 3, no. 2, pp. 91–94, 2004.

[77] L. X. Zhang and X. B. Ren, "In situ observation of reversible domain switching in aged Mn-doped BaTiO$_3$ single crystals," *Physical Review B*, vol. 71, no. 17, p. 174108, 2005.

[78] D. C. Lupascu, Y. A. Genenko, and N. Balke, "Aging in ferroelectrics," *Journal of the American Ceramic Society*, vol. 89, no. 1, pp. 224–229, 2006.

[79] V. S. Postnikov, V. S. Pavlov, and S. K. Turkov, "Internal friction in ferroelectrics due to interaction of domain boundaries and point defects," *Journal of Physics and Chemistry of Solids*, vol. 31, no. 8, pp. 1785–1791, 1970.

[80] W. L. Warren, D. Dimos, B. A. Tuttle, R. D. Nasby, and G. E. Pike, "Electronic domain pinning in Pb(Zr,Ti)O$_3$ thin films and its role in fatigue," *Applied Physics Letters*, vol. 65, no. 8, pp. 1018–1020, 1994.

[81] W. L. Warren, D. Dimos, B. A. Tuttle, and D. M. Smyth, "Electronic and ionic trapping at domain walls in BaTiO$_3$," *Journal of the American Ceramic Society*, vol. 77, no. 10, pp. 2753–2757, 1994.

[82] W. L. Warren, D. Dimos, G. E. Pike, K. Vanheusden, and R. Ramesh, "Alignment of defect dipoles in polycrystalline ferroelectrics," *Applied Physics Letters*, vol. 67, no. 12, pp. 1689–1691, 1995.

[83] W. L. Warren, K. Vanheusden, D. Dimos, G. E. Pike, and B. A. Tuttle, "Oxygen vacancy motion in perovskite oxides," *Journal of the American Ceramic Society*, vol. 79, no. 2, pp. 536–538, 1996.

[84] W. L. Warren, G. E. Pike, K. Vanheusden, D. Dimos, B. A. Tuttle, and J. Robertson, "Defect-dipole alignment and tetragonal strain in ferroelectrics," *Journal of Applied Physics*, vol. 79, no. 12, pp. 9250–9257, 1996.

[85] Y. A. Genenko and D. C. Lupascu, "Drift of charged defects in local fields as aging mechanism in ferroelectrics," *Physical Review B*, vol. 75, no. 18, p. 184107, 2007.

[86] E. Sawaguchi, "Ferroelectricity versus antiferroelectricity in the solid solutions of $PbZrO_3$ and $PbTiO_3$," *Journal of the Physical Society of Japan*, vol. 8, no. 5, pp. 615–629, 1953.

[87] M. Morozov, *Softening and hardening transitions in ferroelectric Pb(Zr,Ti)O₃ ceramics*. PhD thesis, Swiss Federal Institute of Technology, Lausanne, 2005.

[88] M. I. Mendelson, "Average grain size in polycrystalline ceramics," *Journal of the American Ceramic Society*, vol. 52, no. 8, pp. 443–446, 1969.

[89] Y. M. Chiang, D. P. Birnie III, and W. D. Kingery, *Physical ceramics: Principles for ceramic science and engineering*. New York: Wiley, 1997.

[90] P. V. Lambeck and G. H. Jonker, "Ferroelectric domain stabilization in $BaTiO_3$ by bulk ordering of defects," *Ferroelectrics*, vol. 22, no. 1-2, pp. 729–731, 1978.

[91] H. Mestric, R. A. Eichel, T. Kloss, K. P. Dinse, S. Laubach, P. C. Schmidt, K. A. Schonau, M. Knapp, and H. Ehrenberg, "Iron-oxygen vacancy defect centers in PbTiO: Newman superposition model analysis and density functional calculations," *Physical Review B*, vol. 71, no. 18, p. 134109, 2005.

[92] L. X. Zhang, E. Erdem, X. B. Ren, and R. A. Eichel, "Reorientation of $(Mn''_{Ti}$-$V^{\bullet\bullet}_O)^\times$ defect dipoles in acceptor-modified $BaTiO_3$ single crystals: An electron paramagnetic resonance study," *Applied Physics Letters*, vol. 93, no. 20, p. 202901, 2008.

[93] C. H. Park and D. J. Chadi, "Microscopic study of oxygen-vacancy defects in ferroelectric perovskites," *Physical Review B*, vol. 57, no. 22, pp. R13961–R13964, 1998.

[94] S. Pöykkö and D. J. Chadi, "Dipolar defect model for fatigue in ferroelectric perovskites," *Physical Review Letters*, vol. 83, no. 6, pp. 1231–1234, 1999.

[95] H. J. Kleebe, S. Lauterbach, L. Silvestroni, H. Kungl, M. J. Hoffmann, E. Erdem, and R. A. Eichel, "Formation of magnetic grains in ferroelectric $Pb[Zr_{0.6}Ti_{0.4}]O_3$ ceramics doped with $Fe^{3+}$ above the solubility limit," *Applied Physics Letters*, vol. 94, no. 14, p. 142901, 2009.

[96] H. J. Hagemann, "Loss mechanisms and domain stabilisation in doped $BaTiO_3$," *Journal of Physics C: Solid State Physics*, vol. 11, no. 15, pp. 3333–3344, 1978.

[97] J. O. Gentner, P. Gerthsen, N. A. Schmidt, and R. E. Send, "Dielectric losses in ferroelectric ceramics produced by domain-wall motion," *Journal of Applied Physics*, vol. 49, no. 8, pp. 4485–4489, 1978.

[98] R. A. Eichel, "Defect structure of oxide ferroelectrics−valence state, site of incorporation, mechanisms of charge compensation and internal bias fields," *Journal of Electroceramics*, vol. 19, no. 1, pp. 9–21, 2007.

[99] E. Erdem, R. A. Eichel, H. Kungl, M. J. Hoffmann, A. Ozarowski, J. van Tol, and L. C. Brunel, "Local symmetry-reduction in tetragonal (La,Fe)-codoped $Pb[Zr_{0.4}Ti_{0.6}]O_3$ piezoelectric ceramics," *Physica Scripta*, vol. T129, pp. 12–16, 2007.

[100] W. L. Warren, B. A. Tuttle, B. N. Sun, Y. Huang, and D. A. Payne, "Paramagnetic resonance of platinum ions in $PbTiO_3$ single crystals," *Applied Physics Letters*, vol. 62, no. 2, pp. 146–148, 1993.

[101] V. V. Laguta, T. V. Antimirova, M. D. Glinchuk, I. P. Bykov, J. Rosa, M. Zaritskii, and L. Jastrabik, "Local configurational instability of $Cr^{3+}$ in $PbTiO_3$," *Journal of Physics: Condensed Matter*, vol. 9, no. 45, pp. 10041–10049, 1997.

[102] E. Erdem, R. A. Eichel, H. Kungl, M. J. Hoffmann, A. Ozarowski, J. van Tol, and L. C. Brunel, "Characterization of $(Fe'_{Zr,Ti}-V_O^{\bullet\bullet})^{\bullet}$ defect dipoles in (La,Fe)-codoped PZT 52.5/47.5 piezoelectric ceramics by multifrequency electron paramagnetic resonance spectroscopy," *IEEE Transactions on Ultrasonics, Ferroelectrics, and Frequency Control*, vol. 55, no. 5, pp. 1061–1068, 2008.

[103] Y. A. Genenko, "Space-charge mechanism of aging in ferroelectrics: An analytically solvable two-dimensional model," *Physical Review B*, vol. 78, no. 21, p. 214103, 2008.

[104] L. Eyraud, B. Guiffard, L. Lebrun, and D. Guyomar, "Interpretation of the softening effect in PZT ceramics near the morphotropic phase boundary," *Ferroelectrics*, vol. 330, no. 1, pp. 51–60, 2006.

[105] D. M. Smyth, *The defect chemistry of metal oxides*. New York: Oxford University, 2000.

[106] S. Aggarwal and R. Ramesh, "Point defect chemistry of metal oxide heterostructures," *Annual Review of Materials Science*, vol. 28, pp. 463–499, 1998.

[107] Z. Zhang, L. Lu, C. Shu, and P. Wu, "Computational investigation of B-site donor doping effect on fatigue behavior of lead zirconate titanate," *Applied Physics Letters*, vol. 89, no. 15, p. 152909, 2006.

[108] L. Eyraud, P. Eyraud, P. Gonnard, and M. Troccaz, "Influence of the initial lead content on the properties of doped PZT ceramics prepared by wet or dry methods," *Ferroelectrics*, vol. 34, no. 3, pp. 133–138, 1981.

[109] R. J. Nelmes and W. F. Kuhs, "The crystal structure of tetragonal $PbTiO_3$ at room temperature and at 700K," *Solid State Communications*, vol. 54, no. 8, pp. 721–723, 1985.

[110] J. Joseph, T. M. Vimala, V. Sivasubramanian, and V. R. K. Murthy, "Structural investigations on Pb(Zr$_x$Ti$_{1-x}$)O$_3$ solid solutions using the X-ray Rietveld method," *Journal of Materials Science*, vol. 35, no. 6, pp. 1571–1575, 2000.

[111] S. Teslic and T. Egami, "Atomic Structure of PbZrO$_3$ Determined by Pulsed Neutron Diffraction," *Acta Crystallographica*, vol. B54, no. 6, pp. 750–765, 1998.

[112] Mackie, R. A. and Singh, S. and Laverock, J. and Dugdale, S. B. and Keeble, D. J., "Vacancy defect positron lifetimes in strontium titanate," *Physical Review B*, vol. 79, no. 1, p. 014102, 2009.

[113] D. L. Corker, A. M. Glazer, R. W. Whatmore, A. Stallard, and F. Fauth, "A neutron diffraction investigation into the rhombohedral phases of the perovskite series PbZr$_{1-x}$Ti$_x$O$_3$," *Journal of Physics: Condensed Matter*, vol. 10, no. 28, pp. 6251–6269, 1998.

[114] F. F. Ge, W. D. Wu, X. M. Wang, H. P. Wang, Y. Dai, H. B. Wang, and J. Shen, "The first-principle calculation of structures and defect energies in tetragonal PbTiO$_3$," *Physica B*, vol. 404, no. 20, pp. 3814–3818, 2009.

[115] Mackie, R. A. and Pelaiz-Barranco, A. and Keeble, D. J., "Vacancy defects in PbTiO$_3$ and lanthanide-ion-doped PbTiO$_3$: A study of positron lifetimes," *Physical Review B*, vol. 82, no. 2, p. 024113, 2010.

[116] S. Gottschalk, H. Hahn, A. G. Balogh, W. Puff, H. Kungl, and M. J. Hoffmann, "A positron lifetime study of lanthanum and niobium doped Pb(Zr$_{0.6}$Ti$_{0.4}$)O$_3$," *Journal of Applied Physics*, vol. 96, no. 12, pp. 7464–7470, 2004.

[117] E. Goo, R. Mishra, and G. Thomas, "Electron microscopy study of the ferroelectric domains and domain wall structure in PbZr$_{0.52}$Ti$_{0.48}$O$_3$," *Journal of Applied Physics*, vol. 52, no. 4, pp. 2940–2943, 1981.

[118] C. A. Randall, D. J. Barber, and R. W. Whatmore, "Ferroelectric domain configurations in a modified-PZT ceramic," *Journal of Materials Science*, vol. 22, no. 3, pp. 925–931, 1987.

[119] W. Cao and C. A. Randall, "Grain size and domain size relations in bulk ceramic ferroelectric materials," *Journal of Physics and Chemistry of Solids*, vol. 57, no. 10, pp. 1499–1505, 1996.

[120] J. Ricote, D. L. Corker, R. W. Whatmore, S. A. Impey, A. M. Glazer, J. Dec, and K. Roleder, "TEM and neutron diffraction study of the local structure in the rhombohedral phase of lead zirconate titanate," *Journal of Physics: Condensed Matter*, vol. 10, no. 8, pp. 1767–1786, 1998.

[121] J. Ricote, R. W. Whatmore, and D. J. Barber, "Studies of the ferroelectric domain configuration and polarization of rhombohedral PZT ceramics," *Journal of Physics: Condensed Matter*, vol. 12, no. 3, pp. 323–337, 2000.

[122] Q. Tan, Z. Xu, J. F. Li, and D. Viehland, "Role of defect distributions and mobility on ferroelectric phase transformations in lead zirconate titanate," *Applied Physics Letters*, vol. 71, no. 8, pp. 1062–1064, 1997.

[123] S. Wada, K. Yako, H. Kakemoto, T. Tsurumi, and T. Kiguchi, "Enhanced piezoelectric properties of barium titanate single crystals with different engineered-domain sizes," *Journal of Applied Physics*, vol. 98, no. 1, p. 014109, 2005.

[124] J. Hlinka, P. Ondrejkovic, and P. Marton, "The piezoelectric response of nanotwinned $BaTiO_3$," *Nanotechnology*, vol. 20, no. 10, p. 105709, 2009.

[125] R. Ahluwalia, T. Lookman, A. Saxena, and W. Cao, "Domain-size dependence of piezoelectric properties of ferroelectrics," *Physical Review B*, vol. 72, no. 1, p. 014112, 2005.

[126] D. I. Woodward, J. Knudsen, and I. M. Reaney, "Review of crystal and domain structures in the $PbZr_xTi_{1-x}O_3$ solid solution," *Physical Review B*, vol. 72, no. 10, p. 104110, 2005.

[127] H. Zheng, I. M. Reaney, W. E. Lee, N. Jones, and H. Thomas, "Effects of octahedral tilting on the piezoelectric properties of strontium/barium/niobium-doped soft lead zirconate titanate ceramics," *Journal of the American Ceramic Society*, vol. 85, no. 9, pp. 2337–2344, 2002.

[128] C. Kittel, "Theory of structure of ferromagnetic domains in films and small particles," *Physical Review*, vol. 70, no. 11/12, pp. 965–971, 1946.

[129] T. Mitsui and J. Furuichi, "Domain structure of Rochelle salt and $KH_2PO_4$," *Physical Review*, vol. 90, no. 2, pp. 193–202, 1953.

[130] M. J. Hoffmann, M. Hammer, A. Endriss, and D. C. Lupascu, "Correlation between microstructure, strain behavior, and acoustic emission of soft PZT ceramics," *Acta Materialia*, vol. 49, no. 7, pp. 1301–1310, 2001.

[131] M. J. Hoffmann, H. Kungl, R. Theissmann, and S. Wagner, "Microstructural analysis based on microscopy and x-ray diffraction," in *Piezoelectricity: Evolution and Future of a Technology*, Edited by W. Heywang, K. Lubitz, and W. Wersing, 2008, pp. 403-421.

[132] D. Damjanovic and M. Demartin, "Contribution of the irreversible displacement of domain walls to the piezoelectric effect in barium titanate and lead zirconate titanate ceramics," *Journal of Physics: Condensed Matter*, vol. 9, no. 23, pp. 4943–4953, 1997.

[133] K. A. Schönau, M. Knapp, M. Maglione, and H. Fuess, "In situ investigation of the stability field and relaxation behavior of nanodomain structures in morphotropic $Pb[Zr_{1-x}Ti_x]O_3$ under variations in electric field and temperature," *Applied Physics Letters*, vol. 94, no. 12, p. 122902, 2009.

[134] L. E. Cross, "Relaxor ferroelectrics," *Ferroelectrics*, vol. 76, no. 3-4, pp. 241–267, 1987.

[135] L. X. Zhang and X. B. Ren, "Aging behavior in single-domain Mn-doped $BaTiO_3$ crystals: Implication for a unified microscopic explanation of ferroelectric aging," *Physical Review B*, vol. 73, no. 9, p. 094121, 2006.

[136] I. M. Reaney, "Octahedral tilting, domain structure and piezoelectricity in perovskites and related ceramics," *Journal of Electroceramics*, vol. 19, no. 1, pp. 1–8, 2007.

[137] G. Arlt and N. Pertsev, "Force constant and effective mass of 90° domain walls in ferroelectric ceramics," *Journal of Applied Physics*, vol. 70, no. 4, pp. 2283–2289, 1991.

[138] G. Arlt, D. Hennings, and G. de With, "Dielectric properties of fine-grained barium titanate ceramics," *Journal of Applied Physics*, vol. 58, no. 4, pp. 1619–1625, 1985.

[139] Z. Y. Feng and X. B. Ren, "Striking similarity of ferroelectric aging effect in tetragonal, orthorhombic and rhombohedral crystal structures," *Physical Review B*, vol. 77, no. 13, p. 134115, 2008.

[140] J. G. Powles and W. Jackson, "The measurement of the dielectric properties of high-permittivity materials at centimetre wavelengths," *Proceedings of the Institution of Electrical Engineers*, vol. 96, no. 43, pp. 383–389, 1949.

[141] A. von Hippel, "Ferroelectricity, domain structure and phase transitions of barium titanate," *Reviews of Modern Physics*, vol. 22, no. 3, pp. 221–237, 1950.

[142] Y. M. Poplavko, V. G. Tsykalov, and V. I. Molchanov, "Microwave dielectric dispersion of the ferroelectric and paraelectric phases of barium titanate," *Soviet Physics – Solid State*, vol. 10, no. 11, pp. 2708–2710, 1969.

[143] S. Kazaoui, J. Ravez, C. Elissalde, and M. Maglione, "High frequency dielectric relaxation in $BaTiO_3$ derived materials," *Ferroelectrics*, vol. 135, no. 1-4, pp. 85–99, 1992.

[144] M. P. McNeal, S. J. Jang, and R. E. Newnham, "The effect of grain and particle size on the microwave properties of barium titanate ($BaTiO_3$)," *Journal of Applied Physics*, vol. 83, no. 6, pp. 3288–3297, 1998.

[145] R. Gerson, J. M. Peterson, and D. R. Rote, "Dielectric constant of lead titanate zirconate ceramics at high frequency," *Journal of Applied Physics*, vol. 34, no. 11, pp. 3242–3245, 1963.

[146] O. Kersten and G. Schmidt, "Dielectric dispersion in PZT ceramics," *Ferroelectrics*, vol. 67, no. 1, pp. 191–197, 1986.

[147] U. Böttger and G. Arlt, "Dielectric microwave dispersion in PZT ceramics," *Ferroelectrics*, vol. 127, no. 1-4, pp. 95–100, 1992.

[148] G. Arlt, U. Böttger, and S. Witte, "Dielectric dispersion of ferroelectric ceramics and single crystals at microwave frequencies," *Annalen der Physik*, vol. 3, no. 7-8, pp. 578–588, 1994.

[149] S. P. Li, J. Sheen, S. J. Jang, A. S. Bhalla, R. E. Newnham, and L. E. Cross, "Modified lumped parameter method for measurements of dielectric susceptibility in ferroelectrics," *Japanese Journal of Applied Physics, Part 1*, vol. 33, no. 6A, pp. 3617–3621, 1994.

[150] H. Hassan, M. Maglione, M. Fontana, and J. Handerek, "High-frequency dielectric relaxation related to the PE-FE transition in PZT ceramics with low Ti concentration," *Journal of Physics: Condensed Matter*, vol. 7, no. 45, pp. 8647–8654, 1995.

[151] A. V. Turik, K. R. Chernyshov, and V. D. Komarov, "Dielectric dispersion in ferroelectrics with perovskite structure over the meter-wave range," *Ferroelectrics*, vol. 6, no. 1, pp. 45–47, 1973.

[152] Y. Xi, H. McKinstry, and L. E. Cross, "The influence of piezoelectric grain resonance on the dielectric spectra of $LiNbO_3$ ceramics," *Journal of the American Ceramic Society*, vol. 66, no. 9, pp. 637–641, 1983.

[153] M. T. Lanagan, J. H. Kim, S. J. Jang, and R. E. Newnham, "Microwave dielectric properties of antiferroelectric lead zirconate," *Journal of the American Ceramic Society*, vol. 71, no. 4, pp. 311–16, 1988.

[154] J. W. Zhai, X. Yao, M. Z. Wu, and L. Y. Zhang, "Preparation and microwave characterization of $PbTiO_3$ ceramic and powder," *Journal of Physics D: Applied Physics*, vol. 34, no. 9, pp. 1413–1416, 2001.

[155] V. Porokhonskyy, S. Kamba, A. Pashkin, M. Savinov, J. Petzelt, R. E. Eitel, and C. A. Randall, "Broadband dielectric spectroscopy of $(1-x)BiScO_3-xPbTiO_3$ piezoelectrics," *Applied Physics Letters*, vol. 83, no. 8, pp. 1605–1607, 2003.

[156] V. Porokhonskyy, *Dielectric spectroscopy of some high-permittivity ceramics with structural disorder*. PhD thesis, Charles University, Prague, 2004.

[157] M. P. McNeal, *The effects of grain and particle size on the microwave dielectric properties of ferroelectric barium titanate*. PhD thesis, The Pennsylvania State University, Pennsylvania, 1997.

[158] S. Fushimi and T. Ikeda, "Single crystals of lead zirconate-titanate solid solutions," *Japanese Journal of Applied Physics, Part 1*, vol. 3, no. 3, pp. 171–172, 1964.

[159] K. Tsuzuki, K. Sakata, S. Hasegawa, and G. Ohara, "Growth of $Pb(Zr-Ti)O_3$ single crystal by flux method," *Japanese Journal of Applied Physics, Part 1*, vol. 7, no. 8, p. 953, 1968.

[160] K. Tsuzuki, K. Sakata, G. Ohara, and M. Wada, "The growth of ferroelectric $Pb(Zr_xTi_{1-x})O_3$ single crystals," *Japanese Journal of Applied Physics, Part 1*, vol. 12, no. 10, pp. 1500–1503, 1973.

[161] K. Yanagisawa and H. Kanai, "Crystal growth of lead zirconate titanate with additives under hydrothermal conditions," *Japanese Journal of Applied Physics, Part 1*, vol. 36, no. 9B, pp. 6031–6034, 1997.

[162] Z. G. Ye, "High-performance piezoelectric single crystals of complex perovskite solid solutions," *MRS Bulletin*, vol. 34, no. 4, pp. 277–283, 2009.

[163] J. Fousek, "The dielectric properties of single crystals of $BaTiO_3$ at a frequency of 1000 Mc/s," *Czechoslovak Journal of Physics*, vol. 8, no. 2, pp. 254–255, 1958.

[164] T. S. Benedict and J. L. Durand, "Dielectric properties of single domain crystals of $BaTiO_3$ at microwave frequencies," *Physical Review*, vol. 109, no. 4, pp. 1091–1093, 1958.

[165] A. Lurio and E. Stern, "Measurements of dielectric constant of BaTiO$_3$ single crystals in para-electric region at X band," *Journal of Applied Physics*, vol. 31, no. 10, pp. 1805–1809, 1960.

[166] E. Nakamura and J. Furuichi, "Measurement of microwave dielectric constants of ferroelectrics Part I. Dielectric constants of BaTiO$_3$ single crystal at 3.3 KMc/s," *Journal of the Physical Society of Japan*, vol. 15, no. 11, pp. 1955–1960, 1960.

[167] J. M. Ballantyne, "Frequency and temperature response of the polarization of barium titanate," *Physical Review*, vol. 136, no. 2A, pp. A429–A431, 1964.

[168] W. P. Mason and B. T. Matthias, "Theoretical model for explaining the ferroelectric effect in barium titanate," *Physical Review*, vol. 74, no. 11, pp. 1622–1639, 1948.

[169] A. von Hippel, "Piezoelectricity, ferroelectricity and crystal structure," *Zeitschrift für Physik*, vol. 133, no. 1-2, pp. 158–173, 1952.

[170] R. E. Newnham, *Properties of materials: Anisotropy, symmetry, structure*. New York: Oxford University, 2005.

[171] G. Arlt, U. Böttger, and S. Witte, "Emission of GHz shear waves by ferroelastic domain walls in ferroelectrics," *Applied Physics Letters*, vol. 63, no. 5, pp. 602–604, 1993.

[172] D. V. Taylor and D. Damjanovic, "Evidence of domain wall contribution to the dielectric permittivity in PZT thin films at sub-switching fields," *Journal of Applied Physics*, vol. 82, no. 4, pp. 1973–1975, 1997.

[173] F. Xu, S. Trolier-McKinstry, W. Ren, B. Xu, Z. L. Xie, and K. J. Hemker, "Domain wall motion and its contribution to the dielectric and piezoelectric properties of lead zirconate titanate films," *Journal of Applied Physics*, vol. 89, no. 2, pp. 1336–1348, 2001.

[174] J. L. Jones, M. Hoffman, J. E. Daniels, and A. J. Studer, "Direct measurement of the domain switching contribution to the dynamic piezoelectric response in ferroelectric ceramics," *Applied Physics Letters*, vol. 89, no. 9, p. 092901, 2006.

[175] S. J. Zhang, E. F. Alberta, R. E. Eitel, C. A. Randall, and T. R. Shrout, "Elastic, piezoelectric, and dielectric characterization of modified BiScO$_3$-PbTiO$_3$ ceramics," *IEEE Transactions on Ultrasonics, Ferroelectrics, and Frequency Control*, vol. 52, no. 11, pp. 2131–2139, 2005.

[176] R. G. Geyer, P. Kabos, and J. Baker-Jarvis, "Dielectric sleeve resonator techniques for microwave complex permittivity evaluation," *IEEE Transactions on Instrumentation and Measurement*, vol. 51, no. 2, pp. 383–392, 2002.

[177] *IEEE Standard on piezoelectricity*. ANSI/IEEE Std 176-1987 edition, 1987.

[178] E. Buixaderas, V. Bovtun, M. Kempa, M. Savinov, D. Nuzhnyy, F. Kadlec, P. Vanek, J. Petzelt, M. Eriksson, and Z. Shen, "Broadband dielectric response and grain-size effect in K$_{0.5}$Na$_{0.5}$NbO$_3$ ceramics," *Journal of Applied Physics*, vol. 107, no. 1, p. 014111, 2010.

[179] M. Adachi, Y. Akishige, T. Asahi, K. Deguchi, K. Gesi, K. Hasebe, T. Hikita, T. Ikeda, and Y. Iwata, *Ferroelectrics and related substances: Oxides Part 1: Perovskite-type oxides and $LiNbO_3$ family*, vol. III/36A1 of *Landolt-Börnstein, New Series*. Berlin: Springer-Verlag, 2001.

[180] S. J. Zhang, R. Xia, T. R. Shrout, G. Z. Zang, and J. F. Wang, "Characterization of lead free $(K_{0.5}Na_{0.5})NbO_3$-$LiSbO_3$ piezoceramic," *Solid State Communications*, vol. 141, no. 12, pp. 675 – 679, 2007.

[181] G. Arlt, U. Böttger, and S. Witte, "Dielectric dispersion of ferroelectric ceramics and single crystal by sound generation in piezoelectric domains," *Journal of the American Ceramic Society*, vol. 78, no. 4, pp. 1097–100, 1995.

[182] G. Arlt, "Strong ultrasonic microwaves in ferroelectric ceramics," *IEEE Transactions on Ultrasonics, Ferroelectrics, and Frequency Control*, vol. 45, no. 1, pp. 4–10, 1998.

[183] N. A. Pertsev and G. Arlt, "Forced translational vibrations of $90°$ domain walls and the dielectric dispersion in ferroelectric ceramics," *Journal of Applied Physics*, vol. 74, no. 6, pp. 4105–4112, 1993.

[184] Z. Q. Zhuang, M. J. Haun, S. J. Jang, and L. E. Cross, "Composition and temperature dependence of the dielectric, piezoelectric and elastic properties of pure PZT ceramics," *IEEE Transactions on Ultrasonics, Ferroelectrics, and Frequency Control*, vol. 36, no. 4, pp. 413–416, 1989.

[185] G. Arlt, H. Dederichs, and R. Herbiet, "$90°$-domain wall relaxation in tetragonally distorted ferroelectric ceramics," *Ferroelectrics*, vol. 74, no. 1-2, pp. 37–53, 1987.

[186] J. E. Garcia, V. Gomis, R. Perez, A. Albareda, and J. A. Eiras, "Unexpected dielectric response in lead zirconate titanate ceramics: The role of ferroelectric domain wall pinning effects," *Applied Physics Letters*, vol. 91, no. 4, p. 042902, 2007.

[187] D. A. Ochoa, J. E. Garcia, R. Perez, and A. Albareda, "Influence of extrinsic contribution on the macroscopic properties of hard and soft lead zirconate titanate ceramics," *IEEE Transactions on Ultrasonics, Ferroelectrics, and Frequency Control*, vol. 55, no. 12, pp. 2732–2736, 2008.

[188] H. Takahashi, Y. Numamoto, J. Tani, and S. Tsurekawa, "Domain properties of high-performance barium titanate ceramics," *Japanese Journal of Applied Physics, Part 1*, vol. 46, no. 10B, pp. 7044–7047, 2007.

[189] D. Damjanovic, "Hysteresis in piezoelectric and ferroelectric materials," in *The Science of Hysteresis*, Volume 3, Edited by I. Mayergoyz and G. Bertotti. Elsevier, Amsterdam, 2006, pp. 337-465.

[190] D. M. Pozar, *Microwave engineering*. Wiley, second edition ed., 1998.

[191] E. Buixaderas, D. Nuzhnyy, P. Vanek, I. Gregora, J. Petzelt, V. Porokhonskyy, L. Jin, and D. Damjanovic, "Lattice dynamics and dielectric response of undoped, soft and hard $pbzr_{0.42}ti_{0.58}o_3$," *Phase Transitions*, vol. 83, no. 10-11, pp. 917 – 930, 2010.

[192] I. Kornev, L. Bellaiche, P. E. Janolin, B. Dkhil, and E. Suard, "Phase diagram of Pb(Zr,Ti)O$_3$ solid solutions from first principles," *Physical Review Letters*, vol. 97, no. 15, p. 157601, 2006.

[193] D. M. Hatch, H. T. Stokes, R. Ranjan, S. K. Ragini, Mishra, D. Pandey, and B. J. Kennedy, "Antiferrodistortive phase transition in Pb(Ti$_{0.48}$Zr$_{0.52}$)O$_3$: Space group of the lowest temperature monoclinic phase," *Physical Review B*, vol. 65, no. 21, p. 212101, 2002.

[194] D. Pandey, A. K. Singh, and S. Baik, "Stability of ferroic phases in the highly piezoelectric Pb(Zr$_x$Ti$_{1-x}$)O$_3$ ceramics," *Acta Crystallographica*, vol. A64, no. 1, pp. 192–203, 2007.

[195] E. Buixaderas, M. Savinov, M. Kempa, S. Veljko, S. Kamba, J. Petzelt, R. Pankrath, and S. Kapphan, "Infrared and dielectric spectroscopy of the relaxor ferroelectric Sr$_{0.61}$Ba$_{0.39}$Nb$_2$O$_6$," *Journal of Physics: Condensed Matter*, vol. 17, no. 4, pp. 653–666, 2005.

[196] E. Buixaderas, D. Nuzhnyy, S. Veljko, M. Savinov, P. Vanek, S. Kamba, J. Petzelt, and M. Kosec, "Broad-band dielectric spectroscopy of tetragonal PLZT $x$/40/60," *Phase Transitions*, vol. 79, no. 6-7, pp. 415–426, 2006.

[197] W. Wersing, "Small signal resonance methods," in *Piezoelectricity: Evolution and Future of a Technology*, Edited by W. Heywang, K. Lubitz, and W. Wersing, 2008, pp. 423-444.

[198] E. Buixaderas, I. Gregora, S. Kamba, J. Petzelt, and M. Kosec, "Raman spectroscopy and effective dielectric function in PLZT $x$/40/60," *Journal of Physics: Condensed Matter*, vol. 20, no. 34, p. 345229, 2008.

[199] J. Hlinka, T. Ostapchuk, D. Noujni, S. Kamba, and J. Petzelt, "Anisotropic dielectric function in polar nanoregions of relaxor ferroelectrics," *Physical Review Letters*, vol. 96, no. 2, p. 027601, 2006.

[200] W. Pan, E. Furman, G. O. Dayton, and L. E. Cross, "Dielectric ageing effects in doped lead magnesium niobate: lead titanate relaxor ferroelectric ceramics," *Journal of Materials Science Letters*, vol. 5, no. 6, pp. 647–649, 1986.

[201] R. E. Eitel and C. A. Randall, "Octahedral tilt-suppression of ferroelectric domain wall dynamics and the associated piezoelectric activity in Pb(Zr,Ti)O$_3$," *Physical Review B*, vol. 75, no. 9, p. 094106, 2007.

[202] I. Rychetsky, S. Kamba, V. Porokhonskyy, A. Pashkin, M. Savinov, V. Bovtun, J. Petzelt, M. Kosec, and M. Dressel, "Frequency-independent dielectric losses ($1/f$ noise) in PLZT relaxors at low temperatures," *Journal of Physics: Condensed Matter*, vol. 15, no. 35, pp. 6017–6030, 2003.

[203] D. Damjanovic, "Lead-based piezoelectric materials," in *Piezoelectric and acoustic materials for transducer applications*, Edited by A. Safari and E. K. Akdogan. Springer, New York, 2008, pp. 59-79.

[204] D. Damjanovic, "Stress and frequency dependence of the direct piezoelectric effect in ferroelectric ceramics," *Journal of Applied Physics*, vol. 82, no. 4, pp. 1788–1797, 1997.

[205] T. Braun, W. Kleemann, J. Dec, and P. A. Thomas, "Creep and relaxation dynamics of domain walls in periodically poled KTiOPO$_4$," *Physical Review Letters*, vol. 94, no. 11, p. 117601, 2005.

[206] W. Kleemann, "Universal domain wall dynamics in disordered ferroic materials," *Annual Review of Materials Research*, vol. 37, pp. 415–448, 2007.

[207] W. Kleemann, J. Dec, S. Miga, T. Woike, and R. Pankrath, "Non-Debye domain-wall-induced dielectric response in Sr$_{0.61-x}$Ce$_x$Ba$_{0.39}$Nb$_2$O$_6$," *Physical Review B*, vol. 65, no. 22, p. 220101, 2002.

[208] J. Dec, W. Kleemann, and M. Itoh, "Quantum phase transition and dielectric domain wall response of SrTi$^{18}$O$_3$," *Ferroelectrics*, vol. 298, no. 1, pp. 163–169, 2004.

[209] Y. Park, "Low-frequency-dispersion of Pb(Fe$_{1/2}$Nb$_{1/2}$)O$_3$ single crystal in the region of its paraelectric ferroelectric phase transition," *Solid State Communications*, vol. 113, no. 7, pp. 379–383, 2000.

[210] V. Mueller, Y. Shchur, and H. Beige, "Logarithmic domain-wall dispersion," *Ferroelectrics*, vol. 269, no. 1, pp. 201–206, 2002.

[211] V. Mueller, Y. Shchur, and H. Beige, "Dielectric dispersion due to weak domain wall pinning in RbH$_2$PO$_4$," *Physical Review B*, vol. 65, no. 13, p. 134102, 2002.

[212] A. A. Fedorenko, V. Mueller, and S. Stepanow, "Dielectric response due to stochastic motion of pinned domain walls," *Physical Review B*, vol. 70, no. 22, p. 224104, 2004.

[213] J. C. Dyre, "The random free-energy barrier model for ac conduction in disordered solids," *Journal of Applied Physics*, vol. 64, no. 5, pp. 2456–2468, 1988.

[214] T. Nattermann, Y. Shapir, and I. Vilfan, "Interface pinning and dynamics in random systems," *Physical Review B*, vol. 42, no. 13, pp. 8577–8586, 1990.

[215] V. Mueller, Y. Shchur, H. Beige, A. Fuith, and S. Stepanow, "Non-Debye domain wall response in KH$_2$PO$_4$," *Europhysics Letters*, vol. 57, no. 1, pp. 107–112, 2002.

[216] K. Ngai, "Properties of the constant loss in ionically conducting glasses, melts, and crystals," *Journal of Chemical Physics*, vol. 110, no. 21, pp. 10576–10584, 1999.

[217] J. R. Macdonald, "Nearly constant loss or constant loss in ionically conducting glasses: A physically realizable approach," *Journal of Chemical Physics*, vol. 115, no. 13, pp. 6192–6199, 2001.

[218] C. Leon, A. Rivera, A. Varez, J. Sanz, J. Santamaria, and K. L. Ngai, "Origin of constant loss in ionic conductors," *Physical Review Letters*, vol. 86, no. 7, pp. 1279–1282, 2001.

[219] A. K. Jonscher, *Dielectric relaxation in solids*. London: Chelsae Dielectrics, 1983.

[220] A. K. Jonscher, *Universal relaxation law*. London: Chelsae Dielectrics, 1996.

[221] Z. Kutnjak, C. Filipic, A. Levstik, and R. Pirc, "Glassy dynamics of Rb$_{0.40}$(ND$_4$)$_{0.60}$D$_2$PO$_4$," *Physical Review Letters*, vol. 70, no. 25, pp. 4015–4018, 1993.

[222] S. Kamba, V. Bovtun, J. Petzelt, I. Rychetsky, R. Mizaras, A. Brilingas, J. Banys, J. Grigas, and M. Kosec, "Dielectric dispersion of the relaxor PLZT ceramics in the frequency range 20 Hz-100 THz," *Journal of Physics: Condensed Matter*, vol. 12, no. 4, pp. 497–519, 2000.

[223] J. C. Dyre, P. Maass, B. Roling, and D. L. Sidebottom, "Fundamental questions relating to ion conduction in disordered solids," *Reports on Progress in Physics*, vol. 72, no. 4, p. 046501, 2009.

[224] J. R. Macdonald, "Addendum to 'Fundamental questions relating to ion conduction in disordered solids'," *Journal of Applied Physics*, vol. 107, no. 10, p. 101101, 2010.

[225] R. Blinc, V. V. Laguta, B. Zalar, and J. Banys, "Polar nanoclusters in relaxors," *Journal of Materials Science*, vol. 41, no. 1, pp. 27–30, 2006.

[226] L. X. He and D. Vanderbilt, "First-principles study of oxygen-vacancy pinning of domain walls in $PbTiO_3$," *Physical Review B*, vol. 68, no. 13, p. 134103, 2003.

[227] D. Damjanovic and M. Demartin, "The rayleigh law in piezoelectric ceramics," *Journal of Physics D: Applied Physics*, vol. 29, no. 7, pp. 2057–2060, 1996.

[228] D. Damjanovic, "Logarithmic frequency dependence of the piezoelectric effect due to pinning of ferroelectric-ferroelastic domain walls," *Physical Review B*, vol. 55, no. 2, pp. R649–R652, 1997.

[229] A. S. Nowick and W. R. Heller, "Dielectric and anelastic relaxation of crystals containing point defects," *Advances in Physics*, vol. 14, no. 54, pp. 101–166, 1965.

[230] D. Damjanovic, M. Demartin, M. P. Duran, C. Voisard, and N. Setter, "Maxwell-Wagner piezoelectric relaxation in ferroelectric heterostructures," *Journal of Applied Physics*, vol. 90, no. 11, pp. 5708–5712, 2001.

[231] W. Kleemann, T. Braun, J. Dec, and O. Petracic, "Dynamic phase transitions in ferroic systems with pinned domain walls," *Phase Transitions*, vol. 78, no. 9-11, pp. 811–816, 2005.

[232] K. J. Button, ed., *Electromagnetic waves in matter, Part I*, vol. 8 of *Infrared and millimater waves*. New York: Academic Press, 1983.

# List of Figures

# List of Tables

# Publications and conference presentations

## Peer review articles

($\star$: Articles from 1 to 10 are related to this thesis.)

1. <u>L. Jin</u>, V. Porokhonskyy, and D. Damjanovic, "Broad logarithmic dielectric dispersion in Pb(Zr,Ti)$O_3$ ceramics: The influence of the crystalline symmetry and doping on the disorder," *to be submitted*.

2. <u>L. Jin</u>, Z. B. He, and D. Damjanovic, "Domain configurations and parabolic relationship between the domain size and grain size in B-site $Fe^{3+}$-doped Pb(Zr,Ti)$O_3$ ceramics," *to be submitted*.

3. R. A. Mackie, <u>L. Jin</u>, D. Damjanovic, and D. J. Keeble, "Vacancy defects in Nb doped Pb(Zr$_x$Ti$_{1-x}$)$O_3$ ceramics," *to be submitted*.

4. V. Porokhonskyy, <u>L. Jin</u>, and D. Damjanovic, "Common features in the microwave response of perovskite ferroelectric ceramics," *to be submitted*.

5. P. Jakes, E. Erdem, R.-A. Eichel, <u>L. Jin</u>, and D. Damjanovic, "Position of defects with respect to domain walls in $Fe^{3+}$-doped Pb[Zr$_{0.52}$Ti$_{0.48}$]$O_3$ piezoelectric ceramics," *Applied Physics Letters*, vol. 98, art. no. 072907, 2011.

6. E. Buixaderas, D. Nuzhnyy, P. Vanek, I. Gregora, J. Petzelt, V. Porokhonskyy, <u>L. Jin</u>, and D. Damjanovic "Lattice dynamics and dielectric response of soft and hard PbZr$_{0.42}$Ti$_{0.58}$$O_3$," *Phase Transitions*, vol. 83, pp. 917-930 , 2010.

7. <u>L. Jin</u>, V. Porokhonskyy, and D. Damjanovic, "Domain wall contributions in Pb(Zr,Ti)$O_3$ ceramics at morphotropic phase boundary: A study of dielectric dispersion," *Applied Physics Letters*, vol. 96, art. no. 242902, 2010.

8. D. Damjanovic, N. Klein, <u>L. Jin</u>, and V. Porokhonskyy. "What can be expected from lead-free piezoelectric materials?" *Functional Materials Letters*, vol. 3, pp. 5-13, 2010.

9. <u>L. Jin</u>, Z. B. He, and D. Damjanovic, "Nanodomains in $Fe^{+3}$-doped lead zirconate titanate ceramics at the morphotropic phase boundary do not correlate with high properties," *Applied Physics Letters*, vol. 95, art. no. 012905, 2009.

10. V. Porokhonskyy, <u>L. Jin</u>, and D. Damjanovic, "Separation of piezoelectric grain resonance and domain wall dispersion in Pb(Zr,Ti)$O_3$ ceramics," *Applied Physics Letters*, vol. 94, art. no. 212906, 2009.

11. F. Li, <u>L. Jin</u>, Z. Xu, and Z. Q. Guo, "Determination of three-dimensional orientations of ferroelectric single crystals by an improved rotating orientation x-ray diffraction method," *Review of Scientific Instruments*, vol. 80, art. no. 085106, 2009.

12. F. Li, Z. Xu, X. Y. Wei, <u>L. Jin</u>, J. J. Gao, C. H. Zhang, and X. Yao, "Evolution of transverse piezoelectric response of lead zirconate titanate ceramics under hydrostatic pressure," *Journal of Physics D: Applied Physics*, vol. 42, art. no. 072001, 2009.

13. Z. Q. Guo, <u>L. Jin</u>, F. Li, and Y. Bai, "Applications of the rotating orientation XRD method to oriented materials," *Journal of Physics D: Applied Physics*, vol. 42, art. no. 012001, 2009.

14. <u>L. Jin</u>, X. Yao, and X. Y. Wei, "Study of abnormal transient current of PMN-32%PT ferroelectric single crystal in time domain and frequency domain," *Journal of Electroceramics*, vol. 21, pp. 601-604, 2008.

15. F. Li, Z. Xu, X. Y. Wei, X. Yao and <u>L. Jin</u>, Domain switching contribution to piezoelectric response in BaTiO$_3$ single crystals," *Applied Physics Letters*, vol. 93, art. no. 092904 (2008).

16. <u>L. Jin</u>, X. Yao, and X. Y. Wei, "Evolution of piezoelectric resonance in switching current of 0.68Pb(Mg$_{1/3}$Nb$_{2/3}$)O$_3$-0.32PbTiO$_3$ ferroelectric single crystal excited by a stepwise electric field," *Journal of Physics D: Applied Physics*, vol. 41, art. no. 202005, 2008.

17. Y. Bai and <u>L. Jin</u>, "Characterization of frequency-dependent glass transition temperature by Vogel-Fulcher relationship," *Journal of Physics D: Applied Physics*, vol. 41, art. no. 152008, 2008.

18. <u>L. Jin</u>, X. Yao, and X. Y. Wei, "Piezoelectric resonance of lead zirconate titanate ceramics excited by a stepwise electric field," *Journal of Applied Physics*, vol. 99, art. no. 014105, 2006.

19. X. Y. Wei, <u>L. Jin</u>, and X. Yao, "Isothermal relaxation of field-biased barium stannate titanate," *Applied Physics Letters*, vol. 87, art. no. 082905, 2005.

20. <u>L. Jin</u>, X. Yao, X. Y. Wei, and Z. Z. Xi, "Observation of piezoelectric resonance in time domain transient current of ferroelectric ceramics and crystals," *Applied Physics Letters*, vol. 87, art. no. 072910, 2005.

21. X. Y. Wei, Y. J. Feng, L. M. Hang, S. Xia, <u>L. Jin</u>, and X. Yao, "Abnormal C-V curve and clockwise hysteresis loop in ferroelectric barium stannate titanate ceramics," *Materials Science and Engineering B*, vol. 120, pp. 64-67, 2005.

22. <u>L. Jin</u>, Z. Z. Xi, Z. Xu, and X. Yao, "Study of ferroelectric domain morphology in PMN-32%PT single crystals," *Ceramics International*, vol. 30, pp. 1695-1698, 2004.

# Conference Presentations

($\star$: the presenter)

1. <u>Li Jin</u>$^\star$, Viktor Porokhonskyy, and Dragan Damjanovic, Domain wall contributions in Pb(Zr,Ti)O$_3$ ceramics at morphotropic phase boundary: a study of dielectric dispersion, Joint meeting of the 19$^{th}$ International Symposium on the Applications of Ferroelectrics and the 10$^{th}$ European Conference on the Applications of Polar Dielectrics, Edinburgh, Scotland, August 9-12, 2010. (contributed, Poster)

2. Viktor Porokhonskyy$^\star$, <u>Li Jin</u>, and Dragan Damjanovic, Common features in the microwave response of ferroelectric ceramics, Joint meeting of the 19$^{th}$ International Symposium on the Applications of Ferroelectrics and the 10$^{th}$ European Conference on the Applications of Polar Dielectrics, Edinburgh, Scotland, August 9-12, 2010. (contributed, Poster)

3. <u>Li Jin</u>, Viktor Porokhonskyy, and Dragan Damjanovic$^\star$, Broad band dielectric response and meachanisms of softening and harding in Pb(Zr,Ti)O$_3$, Joint meeting of the 12$^{th}$ International Meeting on Ferroelectricity and 18$^{th}$ IEEE International Symposium on Applications of Ferroelectrics, Xi'an, China, August 23-27, 2009. (contributed, Invited Oral talk)

4. Viktor Porokhonskyy$^\star$, <u>Li Jin</u>, and Dragan Damjanovic, On the contribution of piezoelectric resonance of grains to dielectric permittivity of ferroelectrics, Joint meeting of the 12$^{th}$ International Meeting on Ferroelectricity and 18$^{th}$ IEEE International Symposium on Applications of Ferroelectrics, Xi'an, China, August 23-27, 2009. (contributed, Oral talk)

5. Dragan Damjanovic$^\star$, Viktor Porokhonskyy, and <u>Li Jin</u>, Broadband dielectric response and mechanisms of hardening and softening in lead zirconate titanate, 33$^{rd}$ International Conference on Advanced Ceramcs and Composites, Daytona Beach, Florida, USA, January 18-23, 2009. (contributed, Invited Oral talk)

6. <u>Li Jin</u>$^\star$, Viktor Porokhonskyy, and Dragan Damjanovic, Broadband ($10^{-2}$-$10^{10}$ Hz) dielectric response in hard and soft PZT ceramics, 2008 IEEE International Ultrasonics Symposium, Beijing, China, November 2-5, 2008. (contributed, Oral talk)

7. <u>Li Jin</u>$^\star$, X. Yao, and X. Y. Wei, Study of abnormal transient current of PMN-32%PT ferroelectric single crystal in time domain and frequency domain, 4$^{th}$ Asian Meeting on Electroceramics, Hangzhou, China, June 27-30, 2005. (contributed, Poster)

# Curriculum Vitae

## Li Jin (靳立)

*Laboratory of Ceramics, Swiss Federal Institute of Technology–EPFL*
*CH-1015 Lausanne, Switzerland*

## Personal Information

Date of birth: 15th July 1981
Place of birth: Xi'an, People's Republic of China
Nationality: Chinese

## Education

2006.09~present      Ph.D candidate in *Materials Science and Engineering*
Thesis supervised by Prof. DRAGAN DAMJANOVIC
Institute of Materials, School of Engineering
Swiss Federal Institute of Technology, Lausanne, Switzerland

2003.09~2006.07      M. Eng., in *Microelectronics and Solid State Electronics*
Thesis supervised by Prof. XI YAO
School of Electronic and Information Engineering
Xi'an Jiaotong University, Xi'an, People's Republic of China

1999.09~2003.07      B. Eng., in *Electronics Science and Technology*
Thesis supervised by Prof. ZENGZHE XI
School of Electronic and Information Engineering
Xi'an Jiaotong University, Xi'an, People's Republic of China

## Academic Experience

2006.09~present      Research assistant at *Ceramics Laboratory*
Swiss Federal Institute of Technology, Lausanne, Switzerland

2003.09~2006.07      Research assistant at *Electronic Materials Research Laboratory*
Key Laboratory of the Ministry of Education
Xi'an Jiaotong University, Xi'an, People's Republic of China

## Award

- Chinese Government Award for Outstanding Students Abroad (2010)

- Outstanding Graduate in Shaanxi Province (2006)

- Outstanding Graduate in Xi'an Jiaotong University (2006)

- "Tang Wen Zhi" Outstanding President Scholarship (2005)

- "Pan Wen Yuan" Scholarship for Excellent Graduate Student (2005)

- "Chen Qi" Scholarship for Excellent Postgraduate Student (2004)

## Editing and reviewing

- Editor team member of the *Journal of Advanced Dielectrics* (since 2010)

- Review papers on a regular basis for:

    - *Journal of Advanced Dielectrics*
    - *Journal of Alloys and Compounds*
    - *Journal of Materials Research*
    - *Materials Chemistry and Physics*
    - *Materials Research Bulletin*
    - *Smart Materials and Structures*